LEV

AFAL-TR-78-33

MULTIFUNCTION INERTIAL REFERENCE ASSEMBLY TECHNOLOGY (MIRAT) SIMULATION DEVELOPMENT, CONFIGURATION EVALUATION, AND TEST PLAN DEVELOPMENT

The Charles Stark Draper Laboratory, Inc.
Cambridge, Massachusetts 02139

D

MARCH 1978

Final Report   February 1977 - December

AIR FORCE AVIONICS LABORATORY
AIR FORCE WRIGHT AERONAUTICAL LABORATORIES
AIR FORCE SYSTEMS COMMAND

Mr. Jack Bell, AFAL/RWA-2
Project Engineer

FOR THE COMMANDER:

Ronald L. Ringo
Chief, Reference System Branch
Reconnaissance & Weapon Delivery Division
Air Force Avionics Laboratory

SECURITY CLASSIFICATION OF THIS PAGE *(When Data Entered)*

REPORT DOCUMENTATION PAGE		READ INSTRUCTIONS BEFORE COMPLETING FORM
1. REPORT NUMBER AFAL-TR-78-33	2. GOVT ACCESSION NO.	3. RECIPIENT'S CATALOG NUMBER
4. TITLE *(and Subtitle)* MULTIFUNCTION INERTIAL REFERENCE ASSEMBLY TECHNOLOGY (MIRAT) SIMULATION DEVELOPMENT, CONFIGURATION EVALUATION, AND TEST PLAN DEVELOPMENT		5. TYPE OF REPORT & PERIOD COVERED Final Report 2/1/77 - 12/31/77
		6. PERFORMING ORG. REPORT NUMBER R-1135
7. AUTHOR(s) Paul Motyka, Roy Nurse, and Kevin Daly		8. CONTRACT OR GRANT NUMBER(s) F33615-77-C-1103
9. PERFORMING ORGANIZATION NAME AND ADDRESS The Charles Stark Draper Laboratory, Inc. Cambridge, Massachusetts 02139		10. PROGRAM ELEMENT, PROJECT, TASK AREA & WORK UNIT NUMBERS 6095-16-02
11. CONTROLLING OFFICE NAME AND ADDRESS Air Force Avionics Laboratory (RWA-2) Wright-Patterson Air Force Base Ohio 45433		12. REPORT DATE March 1978
		13. NUMBER OF PAGES 105
14. MONITORING AGENCY NAME & ADDRESS *(if different from Controlling Office)* 105 p.		15. SECURITY CLASS. *(of this report)* UNCLASSIFIED
		15a. DECLASSIFICATION/DOWNGRADING SCHEDULE

16. DISTRIBUTION STATEMENT *(of this Report)*

Approved for public release; distribution unlimited.

62204F

D D C
RECEIVED
AUG 11 1978
B

17. DISTRIBUTION STATEMENT *(of the abstract entered in Block 20, if different from Report)*

18. SUPPLEMENTARY NOTES

Final rept. 1 Feb-31 Dec 77,

19. KEY WORDS *(Continue on reverse side if necessary and identify by block number)*

MIRA
Simulation Development
Inertial Navigation Systems

Error-Navigation Algorithm

20. ABSTRACT *(Continue on reverse side if necessary and identify by block number)*

The significance of this research and development to the Air Force lies in the application of the developed simulation tools and techniques to the evaluation of potential Multifunction Inertial Reference Assembly (MIRA) sensor systems. These systems use a minimum number of inertial sensors to provide the inertial-reference information necessary to meet the aircraft requirements for weapon delivery, flight control, navigation, fire control, and flight safety. The simulation development was begun under a previous

DD FORM 1473 EDITION OF 1 NOV 65 IS OBSOLETE
1 JAN 73

next page

408 386

20. Abstract (Cont.)

Consider

contract. However, its capability was increased under this contract, with the development of real-time operation, and the addition of a navigation and attitude error-propagation algorithm. Other models added to the simulation are two-degree-of-freedom gyros, an air-data system, an autopilot, and a transport vehicle. Parametric studies and evaluations of potential MIRA configurations were conducted to support the definition of the long-term MIRA requirements, and to provide an independent evaluation of candidate configurations. The philosophy and details of a test and development plan, specifically geared to MIRA systems, are also discussed.

PREFACE

This report was prepared under Project 6095, covering the period 1 February through 31 December 1977, under Air Force Contract F33615-77-C-1103 by The Charles Stark Draper Laboratory, Inc., Cambridge, Massachusetts 02139.

The monitoring Air Force Project Engineer is Mr. Jack Bell, AFAL/RWA-2, Air Force Avionics Laboratory, Air Force Systems Command, Wright-Patterson Air Force Base, Ohio 45433. This report was submitted in January 1978.

The Draper Laboratory Program Technical Director is Dr. K. Daly; Dr. P. Motyka is the Program Project Engineer; and Mr. R. Nurse was responsible for the development of the sensor models and error navigation algorithm. Mssrs. D. Hauger and M. Santarelli were responsible for the programming of the simulation.

TABLE OF CONTENTS

LIST OF SYMBOLS

a_{g_x}, a_{g_y}, a_{g_z}	Specific forces along gyro x, y, z, axes (z is the spin axis)(ft/s^2 or g).
CC1, CC2	Constants of error-navigation vertical-damping system.
E	Unit delay operator.
$[e_1]$	Unit vector $[1\ 0\ 0]^T$.
$[e_2]$	Unit vector $[0\ 1\ 0]^T$.
$[e_3]$	Unit vector $[0\ 0\ 1]^T$.
g_0	Gravitational constant (32.1725 ft/s^2).
h	True altitude of vehicle above the surface of the earth (ft).
$\underline{h}_{iS}$	Instrument spin axes for i = 1,2,...
$\underline{h}_{ij}$	Instrument measurement axes for i = 1,2,... and j = 1,2,...
h_p	Sensed altitude (ft).
$[I_0]$	Identity matrix.
K_i	Autopilot error gain for i = δθ, ∫δθ, δγ, ∫δγ, δφ, ∫δφ, δψ, ∫δψ, δβ, ∫δβ, δV, ∫δV.
L	Square of the Schuler frequency at vehicle altitude (s^{-2}).

$n_{x_{BI}}$, $n_{y_{BI}}$, $n_{z_{BI}}$ Integrated accelerometer outputs in the body frame (ft/s).

p_A Atmospheric pressure (lb/ft^2).

p_{GB} Roll-rate signal including bending effects (deg/s).

p_{GIM} Integrated roll-rate-gyro signal including misalignment effects (rad).

p_{GI}, q_{GI}, r_{GI} Integrated roll, pitch, yaw rate signals (rad).

$[R]$ Matrix of vehicle position and velocity in inertial space.

R_E Distance of vehicle center of gravity from the center of the earth ($R_0 + h$) (ft).

R_0 Radius of spherical earth (2.0925×10^7 ft).

s Laplace transform variable, s^{-1}.

SF_{p_G} Roll-rate-gyro scale factor (pulse/rad).

t Time (seconds).

$T_{BC_{ij}}$ ij^{th} element of the matrix $[T_{BC}]$.

$[T_{BC}]$ Transformation from the body-axes frame to the computational frame in forward/right/down-axes system.

$[T_{BC}^*]$ Transformation from the body-axes frame to the computational frame in up/east/north-axes system.

$[T_{BI}]$ Transformation matrix from the vehicle-body frame to the inertial frame.

$[T_{CI}]$ Transformation from the computational frame to the inertial frame.

TDFi   Two-degree-of-freedom gyro-error coefficients for $i = 1,2,...,12$.

$[V_{CE}]$ Vector of earth relative velocities of the vehicle in the local-vertical/north frame (ft/s).

$[V_{CI}]$	Vector of the vehicle velocities with respect to the inertial reference frame in local-vertical/north coordinates (ft/s).
$[V_{EI}]$	Vector of the earth's velocity with respect to the inertial reference frame in the local-vertical/north frame (ft/s).
$[V_I]$	Vector of the vehicle velocity in the inertial reference frame (ft/s).
v_g, w_g	Body-axes gust velocities (ft/s).
X_I, Y_I, Z_I	Position along x, y, z axes of inertial earth-centered reference frame (ft).
α	Angle of attack (deg).
β	Sideslip angle (deg).
γ	Flight-path angle (deg).
δ_a	Combined spoiler and aileron deflection, positive trailing edge right surface down (rad or deg).
δ_e	Horizontal tail deflection, positive trailing edge down (deg).
δ_{e_c}	Horizontal tail actuator command signal (deg).
δ_{RP}	Rudder-pedal input (lb).
δ_T	Throttle input (deg).
δ_{δ_x}	Longitudinal center-stick input (lb).
δ_{δ_y}	Roll center-stick input (lb).
Δb_{P_G}	Roll-rate-gyro bias error (pulse/s).
Δh	Computed altitude error due to sensor errors (ft).
Δt	Vehicle computation time increment (seconds).
Δt_{LO}	Low-speed navigation-system computation increment (0.2 second).

$[\Delta V_I]$	Vector of the integrals of the specific forces in the inertial frame (ft/s).
ΔV_{X_A}	Integrated longitudinal accelerometer input to the strapdown local-vertical wander-azimuth navigation algorithm (ft/s).
ΔV_{X_I}, ΔV_{Y_I}, ΔV_{Z_I}	Integrals of the specific force along the x, y, z inertial axes from time t_{n-1} to t_n (ft/s).
$\Delta \theta_{P_G}$, $\Delta \theta_{q_G}$, $\Delta \theta_{r_G}$	Roll-, pitch-, yaw-rate incremental navigation gyro signals (rad).
ε	Perturbation or error of error-navigation-algorithm quantity (i.e., εX_I is the perturbation of X_I).
$[\varepsilon G]$	Vector of integrated rate-gyro errors (rad).
$[\varepsilon G\chi]$	Skew-symmetric form of $[\varepsilon G]$.
εh	Total altitude error; computed altitude less sensed altitude ($\varepsilon h = h + \Delta h - h_p$) (ft).
εp_G, εq_G, εr_G	Integrated rate-gyro errors; components of $[\varepsilon G]$ (rad).
εSF_{P_G}	Roll-rate-gyro scale-factor error.
η_i	Generalized bending-mode coefficient for i = 1,2,...6 (rad).
λ	Latitude (rad).
μ_1, μ_2	Coefficients of roll-rate-gyro misalignment errors.
σ	Longitude (rad).
σ_e^2	Variance of navigation-sensor errors.
τ	Time constant of first-order lag network (seconds).
ϕ, θ, ψ	Roll, pitch, yaw angles of body axes with respect to earth surface frame (rad or deg).

ω_E Angular rate of earth's rotation (7.292×10^{-5} rad/s).

$\omega_{g_x}, \omega_{g_y}, \omega_{g_z}$ Inertial angular rates of the body about gyro x, y, z axes (rad/s).

Subscripts

auto   Autopilot.

c   Command.

err   Error; particularly the difference between the navigation-system output and the vehicle output.

k k^{th} iteration of vehicle equations.

m m^{th} iteration of low-speed navigation system.

n n^{th} iteration of low-speed navigation system.

Superscripts

T   Transpose.

$(\hat{\ })$ Computed.

SECTION 1

INTRODUCTION

This Research and Development Technical Report covers work performed by The Charles Stark Draper Laboratory, Inc., (CSDL) for the U.S. Air Force Systems Command, Aeronautical Systems Division, Wright-Patterson Air Force Base under Contract F33615-77-R-1103 between 1 February and 31 December 1977.

The effort performed under this contract is a natural follow-on to a CSDL effort conducted during calendar year 1976. Reference 1 documents the work performed under this initial effort. Its objective was to develop the tools and techniques required to assess the technical feasibility of using a minimum number of inertial sensors to provide the inertial-reference information consistent with the weapon-delivery, flight-control, navigation, fire-control, and flight safety requirements of an aircraft. The term Multifunction Inertial Reference Assembly (MIRA) describes the generic class of systems designed to meet this objective.

The initial MIRA effort was primarily oriented toward developing and demonstrating simulation capabilities to evaluate MIRA-type systems in realistic environments, and toward considering the life-cycle-cost implications of the MIRA approach. The main goal was to develop a versatile evaluation capability that would have long-term utility in the MIRA effort.

The present CSDL effort documented in this report is denoted Multifunction Inertial Reference Assembly Technology (MIRAT) to differentiate it from the first effort. It has three main objectives. The first is a continuation of the simulation development begun under the first CSDL MIRA effort. Section 2 of this report documents the results. The tasks performed during this phase of the contract were the development of a real-time digital simulation with the same capabilities as the nonreal-time MIRA simulation developed by CSDL

under the first MIRA-related effort, and the addition of an air-data model and a transport-vehicle model into the simulation. Also incorporated was a navigation and attitude error-propagation scheme using incremental velocity- and angular-sensor errors as inputs together with flight-profile data. This algorithm makes it possible to isolate the effects of sensor errors on navigation performance. Two-degree-of-freedom-gyro models were also added to the MIRA simulation to complement the existing laser-gyro models.

The second major CSDL task performed under this contract was directed toward the utilization of the simulation tools in the overall MIRA test and evaluation program. Parametric simulation studies were performed to evaluate the effects of sensor location, sensor type, sensor errors, etc. upon the navigation and flight-control capability of the aircraft. In addition, further simulation studies were performed to evaluate specific MIRA configurations and provide an independent assessment of candidate configurations. The configurations to be evaluated were to be given to CSDL based upon the results of the McDonnell Douglas Aircraft Company MIRA effort. However, this information was not supplied to CSDL in time to be taken into consideration on the present program. Therefore, CSDL selected the configurations to be evaluated. Section 3 describes the simulation runs performed, and presents the results and conclusions obtained from them. The evaluation of the MIRA configurations selected by the McDonnell Douglas Aircraft Company will be completed under an extension to the present contract. The results of this evaluation will be published in an appendix to this report.

The last major task required for CSDL under this contract was the development of a test and evaluation plan for MIRA-type systems. CSDL's proposed plan is presented in Section 4.

Section 5 summarizes the total CSDL MIRA-related effort, and provides information on future MIRA use of the tools developed and results obtained.

2

SECTION 2

MIRA SIMULATION DEVELOPMENT

One of CSDL's major goals on the MIRA program was the development
of a simulation capability to evaluate the MIRA concept. It was de-
cided that the simulation should be completely digital. Furthermore,
both nonreal-time and real-time versions were developed. The nonreal-
time version, coded in FORTRAN, is simpler to implement and allows for
easier checkout, while the real-time version, coded in assembly language,
permits human and/or equipment interaction with the simulated system.
The initial CSDL MIRA effort concentrated on the development of the
nonreal-time simulation capability, while the development of a parallel
real-time capability was emphasized during this contractual effort.
Another primary feature of the MIRA simulation is flexibility. Provi-
sions have been included in the simulation to allow parameters, sensor
configurations, sensor locations, program subroutines, models, etc. to
be changed easily.

The basic computation unit was a Xerox Data Systems (XDS) 9300
general-purpose digital computer. In addition, two Honeywell 124-series
digital computers were interfaced with the XDS 9300 to operate as parallel
processors. This added computation capability is needed for real-time
operation of the MIRA simulation.

This section provides a brief introduction to the capabilities of
the MIRA simulation, and documents its status at the end of this work
effort. In addition, the capability and algorithms added to the simu-
lation during the present contractual effort are presented in detail.
Included under this topic are an error-navigation algorithm, which iso-
lates the effects of sensor errors on navigation performance, and auto-
pilot, altimeter, and two-degree-of-freedom-gyro models. A brief summary
is given of a transport-aircraft model that has been simulated in real
time to permit an investigation of the MIRA concept and MIRA configura-
tions with this type of vehicle. Last of all is a discussion of an
actuator model included in the longitudinal flight-control system.

3

2.1 MIRA Simulation Status

As mentioned previously, CSDL's initial effort on the MIRA project concentrated upon the development of a nonreal-time simulation capability to allow the evaluation of the MIRA concept and MIRA sensor configurations. A major goal of the present effort was the development of an identical capability in a real-time digital simulation. As a result, a real-time simulation is available with the following features:

(1) A tactical fighter aircraft model.

(2) Nonlinear six-degree-of-freedom equations of motion.

(3) A rotating spherical earth model.

(4) Nonlinear aerodynamics valid beyond the stall angle-of-attack.

(5) Three longitudinal- and three lateral-directional structural modes.

(6) A representative flight-control system to improve the flying qualities of the vehicle.

(7) Turbulence and winds.

(8) Flight-control and navigation-sensor models. (These sensors can be located anywhere on the vehicle. The available navigation-sensor models are laser gyros and quartz-flexure accelerometers, and can be used for flight-control purposes.)

(9) An error-navigation algorithm.

(10) An instrumented cockpit.

Most of the models included in the simulation are discussed in detail in the first-phase report.[1]*

2.2 Error-Navigation Algorithm

The nonreal-time version of the MIRA simulation contains a model of a strapdown local-vertical wander-azimuth (LVWA) navigation system obtained from the Standardized Software Development Program.[2] With this system, navigation performance is assessed by consideration of

---

* Superscript numerals refer to similarly numbered items in the List of References.

4

the navigation errors that are obtained by differencing the outputs of the navigation-system model and the corresponding true vehicle states. This scheme reflects the expected performance of an actual inertial-navigation system, since it includes the effects of computational errors in the overall navigation performance.

An alternate approach exists for evaluating the effects of the flight environment on inertial-sensor performance, which has been incorporated into both the real-time and nonreal-time versions of the MIRA simulation. It is a navigation- and attitude-error-propagation scheme using incremental velocity- and angular-sensor errors as inputs together with flight-profile data.[3] In the MIRA simulation, these input errors are obtained by differencing the output of the simulated inertial sensors and the "ideal" sensors, although inertial-sensor-error models could be used as well. The outputs of the error-propagation algorithm are the errors in:

(1) Position—latitude, longitude, altitude.

(2) Velocity—north, east, vertical.

(3) Attitude—roll, pitch, and heading.

The main advantage resulting from the error-propagation approach is the possibility of isolating the effects of the sensor errors on navigation performance. The computational errors inherent in the strapdown LVWA navigation-system algorithm are eliminated from consideration of the navigation perfromance when the error-navigation algorithm is employed. However, with both algorithms incorporated into the nonreal-time MIRA simulation, it is possible to assess the magnitude of this effect.

The following assumptions were made in the development of the navigation-error equations:

(1) The earth is spherical.

(2) The aircraft equations-of-motion model provides a nominal trajectory, consisting of the body-to-local-vertical transformation, the body specific forces, the body angular rates, the latitude, longitude, and altitude of the vehicle, and the local vertical with respect to earth velocities.

(3) The inertial-sensor models provide the errors in the angular rates and specific forces.

Each of these assumptions is consistent with those made in the development of the MIRA simulation.

5

2.2.1 Equation Development

Since the earth model used in both the equations of motion and the strapdown navigation model is spherical, a space-stabilized computational frame is employed for the navigation-error equations. This has the great advantage that the navigation equations, including vertical damping, are perfectly symmetrical with respect to each of the three axes of the position and velocity variables. Therefore, only one axis of the three need be considered in developing the error equations, and the results extended to the remaining two axes by symmetry. The result is that the state errors are arranged in a 2×3-matrix form rather than as a 6×1-column vector, and the state transition matrix becomes 2×2 instead of 6×6. Similarly, the attitude-error equations become a single-matrix vector equation.

The mathematical flow diagram for the x-axis of the space-stable navigation algorithm with vertical damping is shown in Figure 2-1. The corresponding diagram for the y-axis is obtained by replacing ΔV_{X_I}, X_I, and $\dot{X}_I$ by ΔV_{Y_I}, Y_I, and $\dot{Y}_I$, respectively, and similarly for the z-axis.
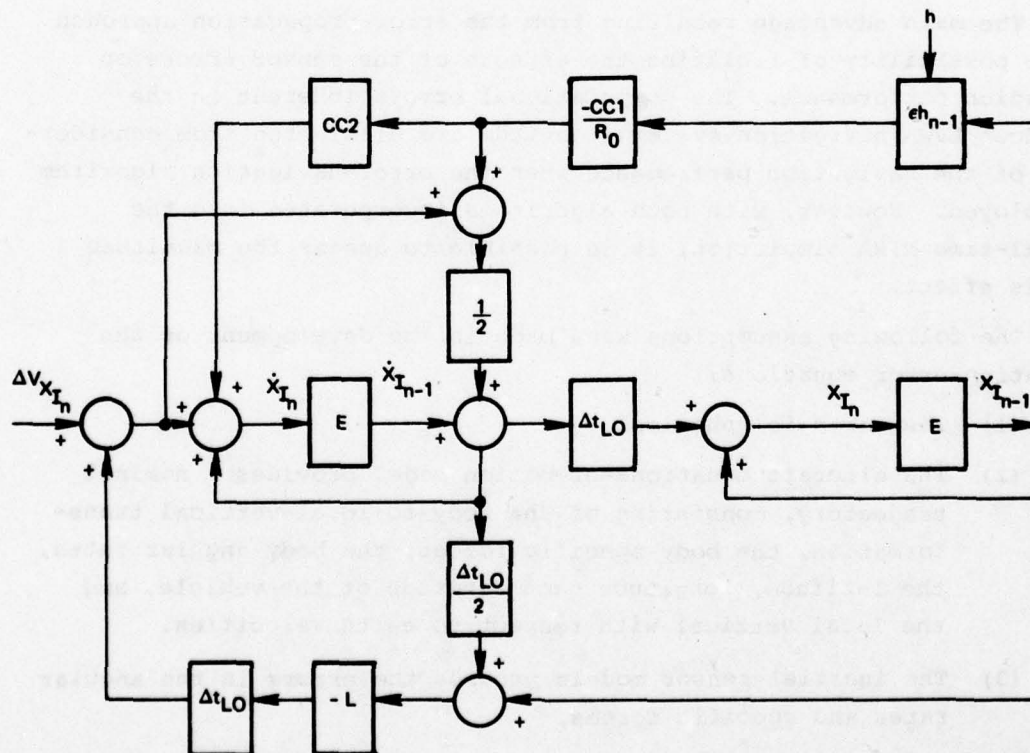

Figure 2-1. Flow diagram for x-axis of space-stable navigation algorithm with vertical damping.

The x-axis navigation algorithm may be written from Figure 2-1 as

$$[X_I]_n = \left\{ [A] + [C]\varepsilon h_{n-1} \right\} [X_I]_{n-1} + [b]\Delta V_{X_{I_n}} \qquad (2-1)$$

where

$$[X_I] = \begin{bmatrix} X_I \\ \dot{X}_I \end{bmatrix} \qquad\qquad [b] = \begin{bmatrix} \dfrac{\Delta t_{LO}}{2} \\ 1 \end{bmatrix} \qquad (2-2)$$

$$[A] = \begin{bmatrix} 1 - \dfrac{L\Delta t_{LO}^2}{2} & \Delta t_{LO}\left(1 - \dfrac{L\Delta t_{LO}^2}{4}\right) \\ -L\Delta t_{LO} & 1 - \dfrac{L\Delta t_{LO}^2}{2} \end{bmatrix} \qquad (2-3)$$

$$[C] = \begin{bmatrix} -\dfrac{CC1 \cdot \Delta t_{LO}}{2R_0} & 0 \\ -\dfrac{CC1 \cdot CC2}{R_0} & 0 \end{bmatrix} \qquad (2-4)$$

For all three axes, the algorithm is

$$[R]_n = \left\{ [A] + [C]\varepsilon h_{n-1} \right\} [R]_{n-1} + [b]\left[\Delta V_I\right]_n^T \qquad (2-5)$$

where

$$[R] = \begin{bmatrix} X_I & Y_I & Z_I \\ \dot{X}_I & \dot{Y}_I & \dot{Z}_I \end{bmatrix} \qquad (2-6)$$

$$[\Delta V_I] = \begin{bmatrix} \Delta V_{X_I} \\ \Delta V_{Y_I} \\ \Delta V_{Z_I} \end{bmatrix} \qquad (2-7)$$

7

Perturbing the elements of Eq. (2-1) (i.e., replacing X_{I_n} by $(X_{I_n} + \epsilon X_{I_n})$, etc.), expanding and retaining only the first-order terms results in

$$[\epsilon X_I]_n = [A][\epsilon X_I]_{n-1} + \{[\epsilon A] + [C]\epsilon h_{n-1}\}[X_I]_{n-1} + [b]\epsilon \Delta V_{X_{I_n}} \qquad (2-8)$$

This is the fundamental error equation for position and velocity.

Each term in Eq. (2-8) is now examined in detail. Consider first the matrix [A], which may be written as

$$[A] = \begin{bmatrix} 1 & \Delta t_{LO} \\ & \\ 0 & 1 \end{bmatrix} - L \begin{bmatrix} \dfrac{\Delta t_{LO}^2}{2} & \dfrac{\Delta t_{LO}^3}{4} \\ & \\ \Delta t_{LO} & \dfrac{\Delta t_{LO}^2}{2} \end{bmatrix} \qquad (2-9)$$

where

$$L = \frac{g_0}{R_0}\left[1 - \left(\frac{3}{R_0}\right)h + \left(\frac{6}{R_0^2}\right)h^2 - \left(\frac{10}{R_0^3}\right)h^3 + \ldots\right] \qquad (2-10)$$

When altitude is perturbed, L may be written as

$$L(h + \epsilon h) = L(h) + \epsilon L(h)$$

$$= L(h) + \frac{\partial L}{\partial h}\epsilon h \qquad (2-11)$$

and

$$\frac{\partial L}{\partial h} = \frac{g_0}{R_0}\left(-\frac{3}{R_0}\right)\left(1 - \frac{4h}{R_0} + \frac{10h^2}{R_0^2} - \ldots\right) \qquad (2-12)$$

The constant portion of the term $\partial L/\partial h$ multiplied by the altitude error is the altitude-divergence term inherent in any undamped three-axis pure inertial navigator. It is the prime reason vertical damping

8

is always incorporated. The net effect of altitude may be incorporated with ample accuracy by considering only this first term, since the rest of the terms in the series are negligible (e.g., 1 percent of the nominal value for altitudes between sea level and 50,000 feet). Therefore, [A] may be written as

$$[A(h + \varepsilon h)] = [A(h)] + [\varepsilon A(h)] \qquad (2\text{-}13)$$

where

$$[\varepsilon A(h)] = \frac{3g_0}{R_0^2} \varepsilon h \begin{bmatrix} \dfrac{\Delta t_{LO}^2}{2} & \dfrac{\Delta t_{LO}^3}{4} \\[3ex] \Delta t_{LO} & \dfrac{\Delta t_{LO}^2}{2} \end{bmatrix} \qquad (2\text{-}14)$$

Next, the term $\varepsilon \Delta V_{X_I}$ has to be expanded so it can be evaluated in terms of known quantities. It is obtained by perturbing the equation for ΔV_{X_I}. This latter quantity is, in turn, obtained by transforming the integrated outputs from the body frame to the inertial frame. In other words

$$[\Delta V_I] = [T_{BI}][\Delta V_A] \qquad (2\text{-}15)$$

and perturbing this equation leads to

$$[\varepsilon \Delta V_I] = [T_{BI}][\varepsilon \Delta V_A] + [\varepsilon T_{BI}][\Delta V_A] \qquad (2\text{-}16)$$

The elements of the vector $[\Delta V_A]$ are the incremental ideal vehicle-accelerometer signals, which are

$$[\Delta V_A] = \begin{bmatrix} -n_{z_{BI}} \\[1ex] n_{y_{BI}} \\[1ex] n_{x_{BI}} \end{bmatrix} \qquad (2\text{-}17)$$

The ordering and signs of the elements of $[\Delta V_A]$ are due to the difference in the orientation of the axes between the vehicle and the navigation

9

system. The vehicle-axes system has a north/east/down orientation, while the navigation-axis system has an up/east/north orientation.

The elements of the vector $[\varepsilon\Delta V_A]$ are the accelerometer-error signals. More specifically, they are the differences between the incremental outputs of the actual accelerometer models and the ideal accelerometer models. In particular

$$[\varepsilon\Delta V_A] = \begin{bmatrix} -\varepsilon n_z \\ \varepsilon n_y \\ \varepsilon n_x \end{bmatrix} \qquad (2\text{-}18)$$

where, for example

$$\varepsilon n_x = \Delta V_{x_A} - n_{x_{BI}}$$

The error in the transformation $[T_{BI}]$ of Eq. (2-16) may be expressed as

$$[\varepsilon T_{BI}] = [T_{BI}][\varepsilon G\chi] \qquad (2\text{-}19)$$

$[\varepsilon G\chi]$ is a skew-symmetric matrix corresponding to the vector of integrated rate errors, i.e.

$$[\varepsilon G] = \begin{bmatrix} -\varepsilon r_G \\ \varepsilon q_G \\ \varepsilon p_G \end{bmatrix} \qquad (2\text{-}20)$$

The elements of $[\varepsilon G]$ are obtained from the difference in the angular increments between the modeled gyros and the ideal gyros every cycle according to the formulae

$$\varepsilon p_{G_n} = \varepsilon p_{G_{n-1}} + (\Delta\theta p_{G_n} - p_{GI_n}) + (r_{GI_n} \cdot \varepsilon q_{G_{n-1}}) - (q_{GI_n} \cdot \varepsilon r_{G_{n-1}})$$

$$\varepsilon q_{G_n} = \varepsilon q_{G_{n-1}} + (\Delta\theta q_{G_n} - q_{GI_n}) - (r_{GI_n} \cdot \varepsilon p_{G_{n-1}}) + (p_{GI_n} \cdot \varepsilon r_{G_{n-1}})$$

$$\varepsilon r_{G_n} = \varepsilon r_{G_{n-1}} + (\Delta\theta r_{G_n} - r_{GI_n}) + (q_{GI_n} \cdot \varepsilon p_{G_{n-1}}) - (p_{GI_n} \cdot \varepsilon q_{G_{n-1}})$$

$$(2\text{-}21)$$

10

Once again, the differences in signs and subscripts are due to the different orientations of the vehicle- and navigation-axes system.

Equation (2-16) may now be rewritten as

$$[\varepsilon \Delta V_I] = [T_{BI}] \left\{ [\varepsilon \Delta V_A] + [\varepsilon G] \times [\Delta V_A] \right\} \qquad (2-22)$$

where $\times$ is the cross-product operation. Combining Eq. (2-22) and (2-8), and expanding to account for the three axes, results in the position- and velocity-vector-error equation

$$[\varepsilon R]_n = [A][\varepsilon R]_{n-1} + \left\{ [\varepsilon A] + [C] \varepsilon h_{n-1} \right\} [R]_{n-1}$$

$$+ [b] \left\{ [T_{CI}][T_{BC}] \left[[\varepsilon \Delta V_A] + [\varepsilon G] \times [\Delta V_A] \right] \right\}^T \qquad (2-23)$$

Use has been made of the equation

$$[T_{BI}] = [T_{CI}][T_{BC}] \qquad (2-24)$$

The major remaining step required for the mechanization of Eq. (2-23) is to define [R] and $[T_{BI}]$ in terms of quantities available from the vehicle model. In order to do this, the transformation from the local-vertical/north frame to the inertial frame is needed. This transformation is given by

$$[T_{CI}] = [T_\Lambda]^T [T_\lambda]$$

$$= \begin{bmatrix} \cos \Lambda & -\sin \Lambda & 0 \\ \sin \Lambda & \cos \Lambda & 0 \\ 0 & 0 & 1 \end{bmatrix} \begin{bmatrix} \cos \lambda & 0 & -\sin \lambda \\ 0 & 1 & 0 \\ \sin \lambda & 0 & \cos \lambda \end{bmatrix} \qquad (2-25)$$

Since

$$\Lambda = \omega_E t + \sigma$$

and λ and σ are available from the vehicle model, each element of this transformation is defined.

11

Position components in the inertial frame are obtained by transforming the radius vector from the earth center to the vehicle center of gravity (cg) through $[T_{CI}]$. That is

$$\begin{bmatrix} X_I \\ Y_I \\ Z_I \end{bmatrix} = [T_{CI}] \begin{bmatrix} R_0 + h \\ 0 \\ 0 \end{bmatrix} = \begin{bmatrix} (R_0 + h)\cos\lambda\cos\Lambda \\ (R_0 + h)\cos\lambda\cos\Lambda \\ (R_0 + h)\sin\lambda \end{bmatrix} \quad (2-26)$$

Note that the x,y,z-axes of the inertial frame are along the earth's polar axis, positive north, along the intersection of the initial meridian plane and the equatorial plane, positive out, and 90 degrees east in the equatorial plane, respectively. The corresponding axes of the local-vertical/north frame are up/east/north.

The velocity components of the vehicle in the inertial frame will now be determined. The earth-relative velocities of the vehicle in the local-vertical/north frame are available from the MIRA simulation and designated as $[V_{CE}]$. The velocity of the earth with respect to the inertial frame in the local-vertical/north frame is designated $[V_{EI}]$, where

$$[V_{EI}] = [0 \quad \omega_E(R_0 + h)\cos\lambda \quad 0]^T \quad (2-27)$$

The vehicle velocity relative to the inertial frame in local-vertical/north coordinates is

$$[V_{CI}] = [V_{CE}] + [V_{EI}] \quad (2-28)$$

Therefore, the vehicle velocity in the inertial frame $[V_I]$ is

$$[V_I] = [T_{CI}][V_{CI}] \quad (2-29)$$

The elements of the matrix [R] are now available from Eq. (2-26) and (2-29).

The next task is the generation of the body-to-inertial transformation, $[T_{BI}]$, required to rotate the increment-velocity-error vector into the inertial frame. $[T_{BI}]$ may be expressed as the product of two

12

rotations: from the body to the local-vertical/north frame, $[T^*_{BC}]$; and
from the local-vertical/north to the inertial frame, $[T_{CI}]$. That is

$$[T_{BI}] = [T_{CI}][T^*_{BC}] \qquad (2-30)$$

A modified version of $[T^*_{BC}]$ is available from the vehicle equations-
of-motion routine. The difference between what is available and what
is needed is due to the difference in the definition of the axes system
between the body frame and the navigation frame. The body frame is
defined in a forward/right/down sense, while the navigation frame is
defined in an up/east/north sense. Taking this difference in axes
systems definition into account, the elements of $[T^*_{BC}]$ are

$$[T^*_{BC}] = \begin{bmatrix} T_{BC_{33}} & -T_{BC_{32}} & -T_{BC_{31}} \\ -T_{BC_{23}} & T_{BC_{22}} & T_{BC_{21}} \\ -T_{BC_{13}} & T_{BC_{12}} & T_{BC_{11}} \end{bmatrix} \qquad (2-31)$$

2.2.2 Attitude Errors

Attitude errors arise from two different, but not independent,
sources. First, any errors in initial alignment or gyro-drift compensa-
tion will produce angular errors in the knowledge of the motion of the
body frame. This information is contained in $[\varepsilon G]$. Second, accelerom-
eter and gyro compensation errors, initial-alignment errors, and mechani-
zation errors integrate into latitude and longitude errors. These lati-
tude and longitude errors are angular errors in the knowledge of the
local-vertical/north frame, since the computed attitude matrix is a func-
tion of both where the computer "thinks" the body frame is, $[\varepsilon G]$, and
where it "thinks" the local-vertical/north frame is, $[\varepsilon \Lambda]$.

The attitude-error equation will now be derived. First, the posi-
tion errors must be interpreted as errors in the transformation from the
inertial frame to the computed local-vertical/north frame. The local-
vertical/north-to-inertial transformation was previously defined in
Eq. (2-25), and its transpose is given by

$$[T_{IC}] = [T_\lambda]^T [T_\Lambda] \qquad (2-32)$$

13

Assume errors in latitude and longitudes, $\varepsilon\lambda$ and $\varepsilon\sigma$, respectively. Also, assume no error in $\omega_E t$ so that $\varepsilon\sigma = \varepsilon\Lambda$. Then the computed transformation becomes $[T_{I\hat{C}}]$ where $\hat{C}$ is the computed local-vertical/north frame. $[T_{I\hat{C}}]$ is defined by

$$[T_{I\hat{C}}] = \left\{[I_0] + \varepsilon\lambda[\Delta T_\lambda(0)]^T\right\}[T_\lambda]^T$$

$$\cdot \left\{[I_0] + \varepsilon\sigma[\Delta T_\Lambda(0)]\right\}[T_\Lambda] \qquad (2\text{-}33)$$

$[\Delta T_\lambda(0)]^T$ is defined as

$$[\Delta T_\lambda(0)]^T = \lim_{\lambda \to 0} \frac{\partial[T_\lambda]}{\partial\lambda}$$

$$= \begin{bmatrix} 0 & 0 & 1 \\ 0 & 0 & 0 \\ -1 & 0 & 0 \end{bmatrix} \qquad (2\text{-}34)$$

and $[\Delta T_\Lambda(0)]$ is defined as

$$[\Delta T_\Lambda(0)] = \lim_{\sigma \to 0} \frac{\partial[T_\Lambda]}{\partial\sigma}$$

$$= \begin{bmatrix} 0 & 1 & 0 \\ -1 & 0 & 0 \\ 0 & 0 & 0 \end{bmatrix} \qquad (2\text{-}35)$$

Expanding Eq. (2-33), retaining only first-order terms, and noting that $[\Delta T_\lambda(0)]^T$ and $[T_\lambda]^T$, and $[\Delta T_\Lambda(0)]$ and $[T_\Lambda]$ commute results in

$$[T_{I\hat{C}}] = \left\{[I_0] + \varepsilon\lambda[\Delta T_\lambda(0)]^T + \varepsilon\sigma[T_\lambda]^T[\Delta T_\Lambda(0)][T_\lambda]\right\}[T_{IC}] \qquad (2\text{-}36)$$

Postmultiplying both sides of Eq. (2-36) by $[T_{CI}]$ and expanding leads to

$$[T_{C\hat{C}}] = [I_0] + \begin{bmatrix} 0 & \varepsilon\sigma\cos\lambda & \varepsilon\lambda \\ -\varepsilon\sigma\cos\lambda & 0 & \varepsilon\sigma\sin\lambda \\ -\varepsilon\lambda & -\varepsilon\sigma\sin\lambda & 0 \end{bmatrix} \qquad (2\text{-}37)$$

$$= [I_0] + [\pi\chi] \qquad (2\text{-}38)$$

14

The matrix $[\pi\chi]$ is the skew-symmetric form of the vector

$$[\pi] = [-\varepsilon\sigma \sin \lambda \quad \varepsilon\sigma \quad -\varepsilon\sigma \cos \lambda]^{T} \tag{2-39}$$

The total error in the computed attitude matrix $[T_{\hat{B}\hat{C}}]$ may now be determined. The matrix $[T_{\hat{B}\hat{C}}]$ is given by

$$[T_{\hat{B}\hat{C}}] = [T_{C\hat{C}}][T_{BC}][T_{\hat{B}B}] \tag{2-40}$$

$$= \left\{[I_0] + [\pi\chi]\right\}[T_{BC}]\left\{[I_0] + [\varepsilon G\chi]\right\} \tag{2-41}$$

or

$$[\varepsilon T_{BC}] = [T_{\hat{B}\hat{C}}] - [T_{BC}]$$

$$= [\pi\chi][T_{BC}] + [T_{BC}][\varepsilon G\chi] \tag{2-42}$$

Equation (2-42) is the matrix expression for the errors in the computed attitude matrix. Another expression for the same errors will be derived as a function of the attitude (Euler) angles, the two equated, and the attitude errors solved for.

The true attitude matrix or body-to-local-vertical/north transformation is given by

$$[T_{BC}] = [T_{\psi}][T_{\theta}]^{T}[T_{\phi}]^{T} \tag{2-43}$$

where

$$[T_{\psi}] = \begin{bmatrix} 1 & 0 & 0 \\ 0 & \cos \psi & \sin \psi \\ 0 & -\sin \psi & \cos \psi \end{bmatrix} \tag{2-44}$$

$$[T_{\theta}] = \begin{bmatrix} \cos \theta & 0 & -\sin \theta \\ 0 & 1 & 0 \\ \sin \theta & 0 & \cos \theta \end{bmatrix} \tag{2-45}$$

$$[T_{\phi}] = \begin{bmatrix} \cos \phi & \sin \phi & 0 \\ -\sin \phi & \cos \phi & 0 \\ 0 & 0 & 1 \end{bmatrix} \tag{2-46}$$

15

If all of the attitude angles are perturbed by small angles $\varepsilon\psi$, $\varepsilon\theta$, and $\varepsilon\phi$, the resultant will be the computed attitude matrix, $[T^{\wedge\wedge}_{BC}]$. This matrix is given by

$$[T^{\wedge\wedge}_{BC}] = [T_\psi]\left\{[I_0] + \varepsilon\psi[\Delta T_\psi(0)]\right\}[T_\theta]^T\left\{[I_0] + \varepsilon\theta[\Delta T_\theta(0)]^T\right\}$$

$$\cdot \, [T_\phi]^T\left\{[I_0] + \varepsilon\phi[\Delta T_\phi(0)]^T\right\} \tag{2-47}$$

$[\Delta T_\theta(0)]^T$ and $[\Delta T_\phi(0)]$ are given by Eq. (2-34) and (2-35), respectively, while

$$[\Delta T_\psi(0)] = \lim_{\psi\to 0} \frac{\partial [T_\psi]}{\partial \psi}$$

$$= \begin{bmatrix} 0 & 0 & 0 \\ 0 & 0 & 1 \\ 0 & -1 & 0 \end{bmatrix} \tag{2-48}$$

Expanding Eq. (2-47), retaining first-order terms, and manipulating leads to

$$[\varepsilon T_{BC}] = [T^{\wedge\wedge}_{BC}] - [T_{BC}]$$

$$= [T_{BC}]\left\{\varepsilon\phi[\Delta T_\phi(0)]^T + [T_\phi]\left\{\varepsilon\theta[\Delta T_\theta(0)]^T\right.\right.$$

$$\left.\left. + \varepsilon\psi[T_\theta][\Delta T_\psi(0)][T_\theta]^T\right\}[T_\phi]^T\right\} \tag{2-49}$$

Equating Eq. (2-42) and (2-49) gives the matrix form of the attitude-error equation

$$\varepsilon\phi[\Delta T_\phi(0)]^T + [T_\phi]\left\{\varepsilon\theta[\Delta T_\theta(0)]^T\right.$$

$$\left. + \varepsilon\psi[T_\theta][\Delta T_\psi(0)][T_\theta]^T\right\}[T_\phi]^T = [\varepsilon G\chi] + [T_{CB}][\pi\chi][T_{BC}]$$

$$\tag{2-50}$$

Equation (2-50) is equivalent to the vector equation

$$[\varepsilon G] + [T_{CB}][\pi] = \varepsilon\phi[e_3] + [T_\phi]\left\{\varepsilon\theta[e_2] - \varepsilon\psi[T_\theta][e_1]\right\} \tag{2-51}$$

16

The right side of Eq. (2-51) may be expanded so that

$$[\varepsilon G] + [T_{CB}][\pi] = \begin{bmatrix} -\cos\theta\cos\psi & \sin\phi & 0 \\ \cos\theta\sin\psi & \cos\phi & 0 \\ -\sin\theta & 0 & 1 \end{bmatrix} \begin{bmatrix} \varepsilon\psi \\ \varepsilon\theta \\ \varepsilon\phi \end{bmatrix} \qquad (2-52)$$

which can be solved for the three Euler-angle-error terms by inversion of the matrix. The result is

$$\begin{bmatrix} \varepsilon\psi \\ \varepsilon\theta \\ \varepsilon\phi \end{bmatrix} = \frac{1}{\cos\theta} \begin{bmatrix} -\cos\phi & \sin\phi & 0 \\ \sin\phi\cos\theta & \cos\phi\cos\theta & 0 \\ -\cos\phi\sin\theta & \sin\phi\sin\theta & -\cos\theta \end{bmatrix} \left\{ [\varepsilon G] + [T_{CB}][\pi] \right\}$$

$$(2-53)$$

2.2.3 Position Errors

Position errors in the local-vertical/north frame for output or attitude-error computation may be determined by perturbing the trigonometric functions of σ and λ, and substituting the inertial-position components into the trigonometric functions.

Latitude error is found from

$$\sin(\lambda + \varepsilon\lambda) = \sin\lambda + \varepsilon\lambda\cos\lambda \qquad (2-54)$$

Since

$$\sin\lambda = \frac{Z_I}{R_E} \qquad (2-55)$$

$$\cos\lambda = \frac{\sqrt{X_I^2 + Y_I^2}}{R_E} \qquad (2-56)$$

$$R_E = R_0 + h \qquad (2-57)$$

$$\Delta h = \varepsilon R_E \qquad (2-58)$$

17

then

$$\epsilon\lambda = \frac{\epsilon Z_I - \Delta h \sin \lambda}{R_E \cos \lambda} \qquad (2\text{-}59)$$

Similarly, the longitude error ($\epsilon\sigma = \epsilon\Lambda$) is found from

$$\sin (\Lambda + \epsilon\Lambda) = \sin \Lambda + \epsilon\Lambda \cos \Lambda \qquad (2\text{-}60)$$

Since

$$\sin \Lambda = \frac{Y_I}{\sqrt{X_I^2 + Y_I^2}} \qquad (2\text{-}61)$$

it follows that

$$\epsilon\sigma = \frac{\epsilon Y_I \cos \Lambda - \epsilon X_I \sin \Lambda}{R_E \cos \lambda} \qquad (2\text{-}62)$$

$$= \frac{X_I \epsilon Y_I - Y_I \epsilon X_I}{(R_E \cos \lambda)^2} \qquad (2\text{-}63)$$

The altitude error may be found from

$$\Delta h = \frac{X_I \epsilon X_I + Y_I \epsilon Y_I + Z_I \epsilon Z_I}{R_E} \qquad (2\text{-}64)$$

2.2.4 Ground-Velocity Errors

The errors in the local-vertical/north ground velocities are obtained from Eq. (2-27), (2-28), and (2-29). Solving for $[V_{CE}]$ results in

$$[V_{CE}] = [T_{IC}][V_I] - [V_{EI}] \qquad (2\text{-}65)$$

18

Perturbing the parameters of this equation and solving for the error in ground velocities leads to

$$[\varepsilon V_{CE}] = [T_{IC}][\varepsilon V_I] + [\varepsilon T_{IC}][V_I] - [\varepsilon V_{EI}] \qquad (2\text{-}66)$$

where $[T_{IC}]$ is obtained from Eq. (2-25); $[\varepsilon T_{IC}]$ is equal to $[\pi\chi][T_{IC}]$, obtained from Eq. (2-37); $[\varepsilon V_I]$ is obtained from Eq. (2-23); $[V_I]$ is obtained from Eq. (2-29); and

$$[\varepsilon V_{EI}] = [0 \quad -\varepsilon\lambda R_E \sin \lambda + \varepsilon h \cos \lambda \quad 0]^T \qquad (2\text{-}67)$$

2.2.5 Computational Frequencies

The equations that have been mechanized in the MIRA simulation are the inertial-state-error equation (2-23), the attitude-error equation (2-53), the position-error equations (2-59), (2-63), (2-64), and the ground-velocity-error equation (2-66). The fundamental computation frequency at which these equations are solved is 5 Hz. The only operations that must be performed at a higher frequency are those required to accumulate the total body misalignment and the incremental velocity errors in the inertial frame. This is the

$$[T_{BC}]\left\{[\varepsilon \Delta V_A] + [\varepsilon G] \times [\Delta V_A]\right\}$$

term of Eq. (2-23). These computations are performed at 50 Hz in the MIRA simulation. Ten samples of the outputs of this computation are summed and used in the other calculations of Eq. (2-23). In addition, the midcycle value of $[T_{CI}]$ is used in the solution of this equation to obtain a better estimate of its average value over a computational cycle.

2.3 Autopilot Algorithm

Previously, the only possible inputs to the MIRA simulation vehicle have been the pilot commands. Profile time histories of the desired signals are entered as a series of points in time along with the corresponding amplitudes of the input variable at the time points. The computer program linearly interpolates the amplitude of the input variable between the time points to achieve the desired profiles. With this capability, it is possible to approximate pilot inputs present in flight.

19

However, with this scheme it is difficult to have the vehicle fly a desired trajectory since it is not always possible to accurately determine the pilot commands that will generate the trajectory. To overcome this shortcoming in the MIRA simulation, an autopilot has been added to allow the vehicle to fly a desired trajectory. The autopilot generates the pilot commands that result in the vehicle following the flight-path, pitch-attitude-angle, roll-angle, heading, sideslip, or velocity commands entered into the simulation. The profile-generation scheme, mentioned in the previous paragraph, can be used to generate the desired trajectory commands. The pilot commands that cause the vehicle to fly the desired trajectory are generated based upon the error between the desired command signal and the actual signal. In order to null out any steady-state errors that may arise, the pilot command is also a function of the integral of the error between the desired and actual signal.

More specifically, the autopilot equations programmed into the MIRA simulation are

$$\delta_{s_{x \text{ auto}}} = K_{\delta\theta} \, \delta\theta + K_{\int\delta\theta} \int\delta\theta + K_{\delta\gamma} \, \delta\gamma + K_{\int\delta\gamma} \int\delta\gamma \qquad (2\text{-}68)$$

where

$$\delta\theta = \theta_c - \theta$$

$$\delta\gamma = \gamma_c - \gamma$$

$$\delta_{s_{y \text{ auto}}} = K_{\delta\phi} \, \delta\phi + K_{\int\delta\phi} \int\delta\phi \qquad (2\text{-}69)$$

where

$$\delta\phi = \phi_c - \phi$$

$$\delta_{RP \text{ auto}} = K_{\delta\psi} \, \delta\psi + K_{\int\delta\psi} \int\delta\psi + K_{\delta\beta} \, \delta\beta + K_{\int\delta\beta} \int\delta\beta \qquad (2\text{-}70)$$

where

$$\delta\psi = \psi_c - \psi$$

$$\delta\beta = \beta_c - \beta$$

20

$$\delta_{T \text{ auto}} = K_{\delta V} \, \delta V + K_{\int \delta V} \int \delta V \qquad (2\text{-}71)$$

where

$$\delta V = V_c - V_A$$

2.4 Altimeter Model

Both the navigation algorithm and error-navigation algorithm incorporated in the MIRA simulation require altitude as an input to provide damping of the vertical channel. It is possible to select one of three signals for this use. Figure 2-2 indicates the options. One option is true altitude, which assumes a perfect altimeter. The second option results in an altitude signal, which is generated by adding a bias to the true altitude and lagging the sum. The last option requires atmospheric pressure, which is generated in the MIRA simulation by
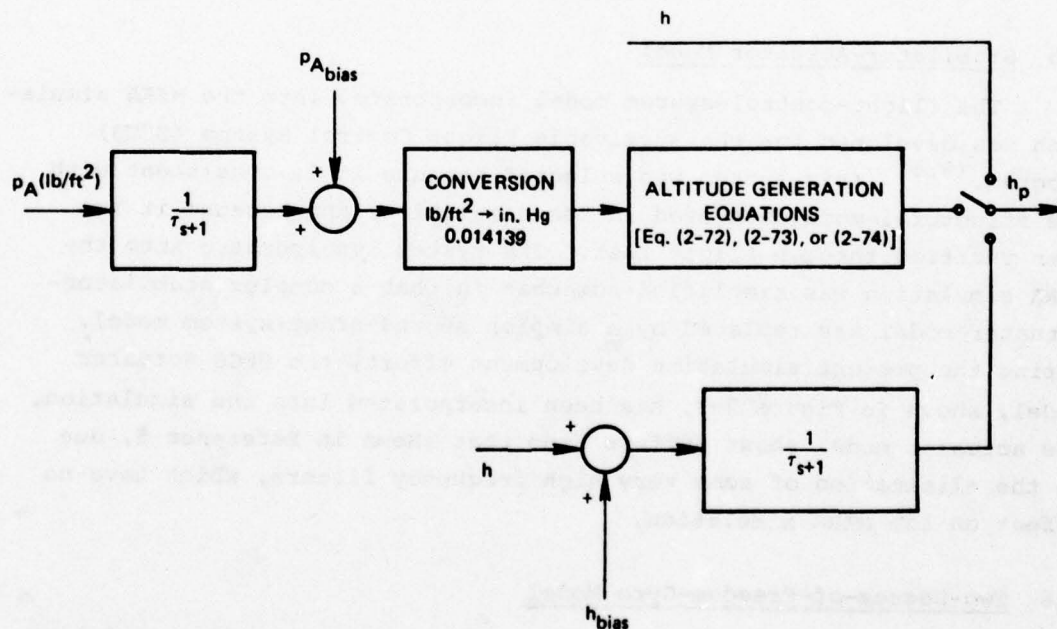
Figure 2-2. Altimeter model.

21

table lookup as a function of true altitude. The atmospheric signal
is lagged and a bias added to simulate the operation of the sensor.
The air-data computer is simulated by generating altitude from atmos-
pheric pressure using the following functions.[4]

For $h_p \leq 36089.23$ ($6.68323876 \leq p_A$)

$$h_p = 145442.156 \left\{ 1 - \left(\frac{p_A}{29.9212598} \right)^{0.190263105} \right\} \qquad (2-72)$$

For $36089.23 \leq h_p \leq 65616.79$ ($1.61673069 < p_A < 6.68323876$)

$$h_p = 36089.23 + 20805.8257 \, \ell n \left(\frac{6.68323876}{p_A} \right) \qquad (2-73)$$

For $65616.79 \leq h_p \leq 104986.87$ ($p_A \leq 1.61673069$)

$$h_p = 65616.7979 - 710793.963 \left\{ 1 - \left(\frac{p_A}{1.61673069} \right)^{-0.029271247} \right\} \qquad (2-74)$$

2.5 Stabilator-Actuator Model

The flight-control-system model incorporated into the MIRA simula-
tion was developed for the Survivable Flight Control System (SFCS)
Program.[5,6] This system was selected because it is consistent with
the structural-mode data used in the simulation, and because it has
been verified through flight test. The system incorporated into the
MIRA simulation was simplified somewhat in that a complex stabilator-
actuator model was replaced by a simpler second-order-system model.
During the present simulation development effort, the SFCS actuator
model, shown in Figure 2-3, has been incorporated into the simulation.
The actuator model shown differs from that shown in Reference 5, due
to the elimination of some very high frequency filters, which have no
effect on the MIRA simulation.

2.6 Two-Degree-of-Freedom-Gyro Model

Models of laser gyros were incorporated into the MIRA simulation
during the initial phase of the program. This capability has been
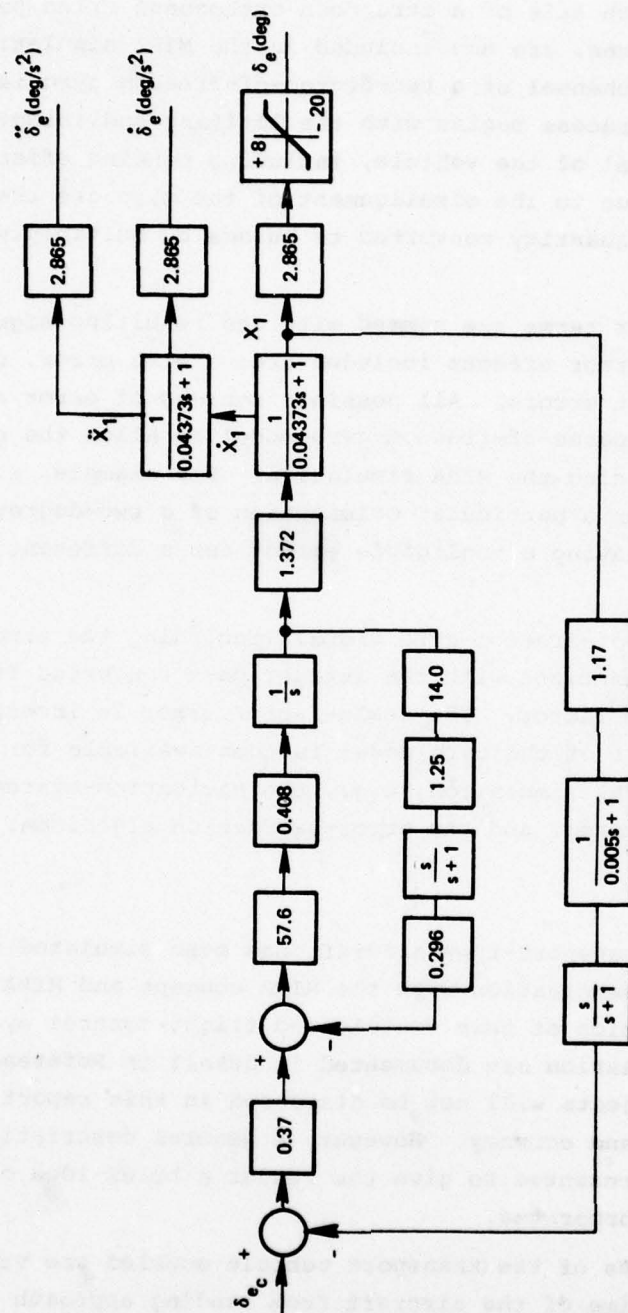
22

Figure 2-3. Survivable Flight Control System stabilizer-actuator model.

$\ddot{\delta}_e \, (\text{deg/s}^2)$ $\dot{\delta}_e \, (\text{deg/s}^2)$ $\delta_e \, (\text{deg})$

$+8$ / -20

2.865 2.865 2.865

$\dfrac{1}{0.04373s + 1}$ $\ddot{X}_1$ $\dfrac{1}{0.04373s + 1}$ $\dot{X}_1$

1.372

$\dfrac{1}{s}$ 14.0

1.25

$\dfrac{s}{s+1}$

0.296

0.408 57.6

$\dfrac{1}{0.005s + 1}$ 1.17

$\dfrac{s}{s+1}$

0.37

δ_{e_c}

X_1

expanded to include models of two-degree-of-freedom gyroscopes. Three models, representing a channel of a two-degree-of-freedom gyro instrument mounted along each axis of a strapdown orthogonal triad parallel to the vehicle-body axes, are now included in the MIRA simulation. A block diagram of one channel of a two-degree-of-freedom gyro is shown in Figure 2-4. The process begins with the limiting and integration of the roll-rate signal of the vehicle, including bending effects. The coupling errors due to the misalignment of the gyro are then added in and the resulting quantity converted to pulses by multiplying by the scale factor.

Additional error terms are summed with the resulting signal at this junction. The error effects included are: a bias error, g, g^2, $g \times g$- and $\omega \times \omega$-dependent errors. All possible sources of error are included in the two-degree-of-freedom-gyro model to allow the greatest flexibility in exercising the MIRA simulation. For example, a term may have an effect for a particular orientation of a two-degree-of-freedom gyro, while having a negligible effect for a different orientation.

The two-degree-of-freedom-gyro signal (including the error effects) is then lagged and quantized with the integer part converted from pulses to radians via the scale factor. The scale-factor error is incorporated at this time. The output of the gyro model is then available for use in other subroutines of the MIRA simulation, e.g., the navigation-system model, the flight-control system, and the error-navigation algorithm.

2.7 Transport Model

A model of a transport-type aircraft has been simulated in real time to allow its investigation with the MIRA concept and MIRA configurations. The aerodynamics of this vehicle and flight-control system included in the simulation are documented in detail in Reference 7. The details of these subjects will not be discussed in this report for the sake of brevity and economy. However, a general description of the transport model is presented to give the reader a brief idea of the features that it incorporates.

The aerodynamics of the transport vehicle modeled are valid over the whole flight regime of the aircraft from landing approach to cruise.
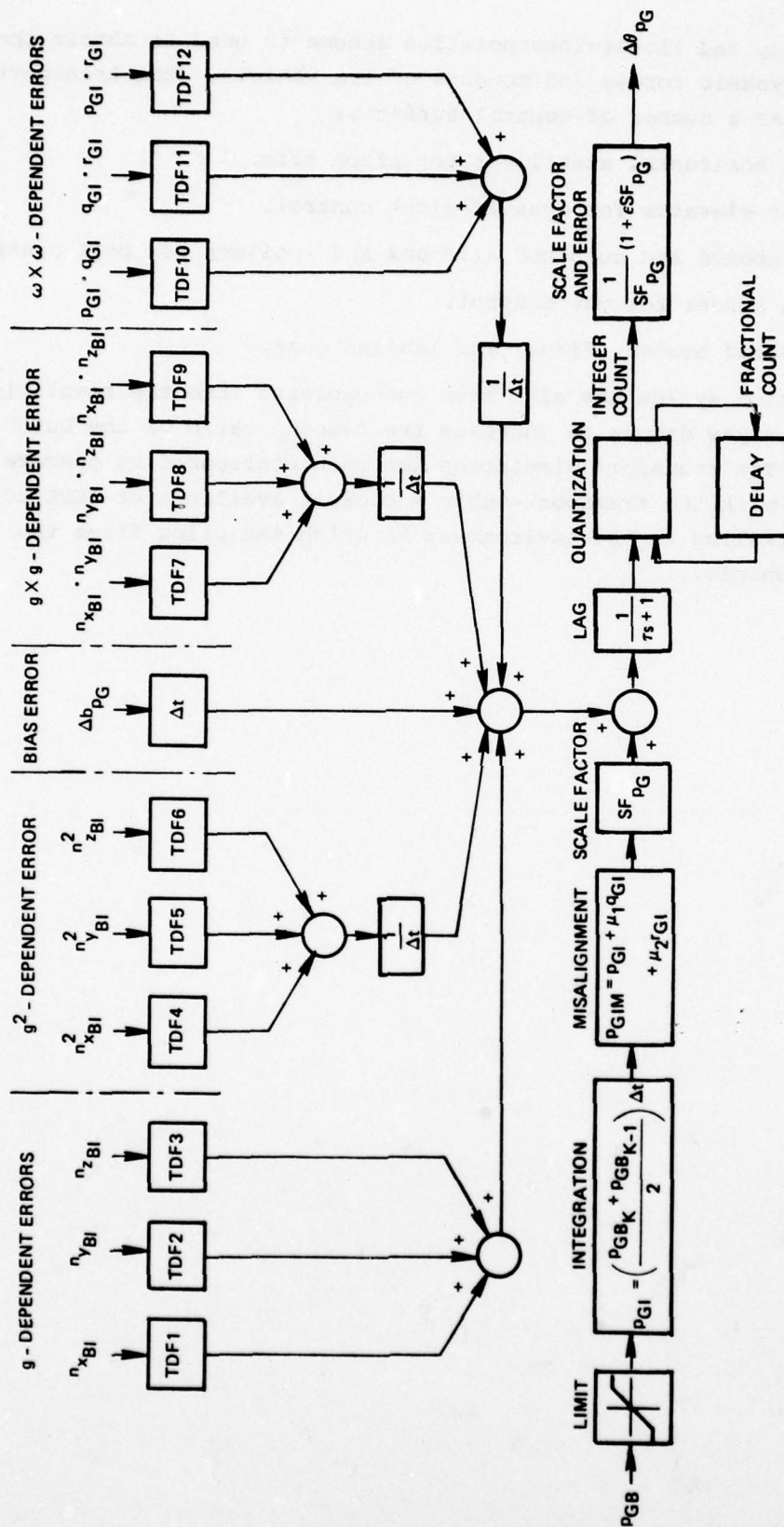
Figure 2-4. Roll channel of two-degree-of-freedom-gyro model.

A table-lookup and linear-interpolation scheme is used to obtain the proper aerodynamic forces and moments of the vehicle. The transport model includes a number of control surfaces:

  (1) A horizontal stabilizer for pitch trim.

  (2) An elevator for dynamic pitch control.

  (3) Inboard and outboard ailerons and spoilers for roll control.

  (4) A rudder for yaw control.

  (5) Speed brakes, flaps, and landing gear.

An augmentation system has also been incorporated into the simulation. It includes a yaw damper to increase the damping ratio of the Dutch-roll mode. The transport simulation has been configured to operate in conjunction with the transport-vehicle cockpit available at CSDL to give added realism to the environment in which the pilot flies the simulated vehicle.

SECTION 3

MIRA CONFIGURATION EVALUATION

This section is devoted to an evaluation of potential MIRA configurations using the simulation capability outlined in Section 2.1. The data runs were selected to provide a maximum amount of information with a minimum number of runs. From the data collected, it is possible to assess the comparative effects of:

    (1) A realistic and ideal environment.

    (2) Lever-arm effects due to sensor location.

    (3) Two-degree-of-freedom and laser gyros.

    (4) Different sensor configurations.

    (5) The effect of the sensor configurations on navigation and flight control.

    (6) The use of navigation sensors for flight-control purposes.

The initial part of this section is devoted to a discussion of the simulation input data, i.e., sensor configurations, flight trajectories, sensor-error coefficients, structural-mode effects on the sensors, etc. The results obtained via the MIRA simulation are then presented, followed by a discussion of the simulation results and conclusions drawn from the results.

3.1 Simulation Input Data

Two distinct sets of simulation runs were performed under this effort as outlined in Table 3-1. One set of runs is short-term (30-second) and was designed to excite the longitudinal and lateral-directional transient modes of the vehicle, so that the comparative effects of the potential MIRA configurations on the handling qualities of the vehicle could be investigated. A second set of runs of 1-hour duration was designed to evaluate the navigation performance of the potential MIRA configurations.

27

Table 3-1. MIRA configuration evaluation runs.

Configuration	Gyro Type	Sensor Location	Turbulence and Modes	Short Run	Long Run	Navigation Sensors for Flight Control
Triad	Laser	FS313	No	Yes	Yes	No
Triad	Two-degree-of-freedom	FS313	No	Yes	Yes	No
Triad	Laser	FS313	Yes	Yes	Yes	No
Triad	Laser	FS77	Yes	Yes	Yes	No
Triad	Two-degree-of-freedom	FS313	Yes	Yes	Yes	No
Triad	Two-degree-of-freedom	FS77	Yes	Yes	Yes	No
Dodecahedron	Laser	FS313	Yes	Yes	Yes	No
Octahedron	Two-degree-of-freedom	FS313	Yes	Yes	Yes	No
Triad	Laser	FS313	Yes	Yes	No	Yes
Triad	Two-degree-of-freedom	FS313	Yes	Yes	No	Yes

The nominal flight condition of the vehicle for all of the simulation runs is 0.5 Mach at an altitude of 5000 feet. Figure 3-1 depicts the autopilot-trajectory commands for the short-duration simulation runs. The bank-angle and heading commands were selected to cause the vehicle to undergo a coordinated 30-degree banked turn until the heading angle changed by 30 degrees. The 5-degree change in flight-path angle was arbitrarily selected to excite the longitudinal modes of the vehicle. For the long-duration navigation evaluation runs, the autopilot commands were selected so that the vehicle would fly due north at a constant speed and constant altitude. When turbulence is present, its nominal rms value is 6 feet per second, which corresponds to the level of clear-air turbulence specified in Reference 8 at the nominal altitude.

The orthogonal triad was selected as one of the basic sensor configurations for evaluation in this study. Results were obtained for this sensor configuration using either laser or two-degree-of-freedom gyros, located near the cg of the vehicle (FS313) or just in front of the pilot's station (FS77). In addition, the comparative effects of the environment were evaluated using this configuration by performing
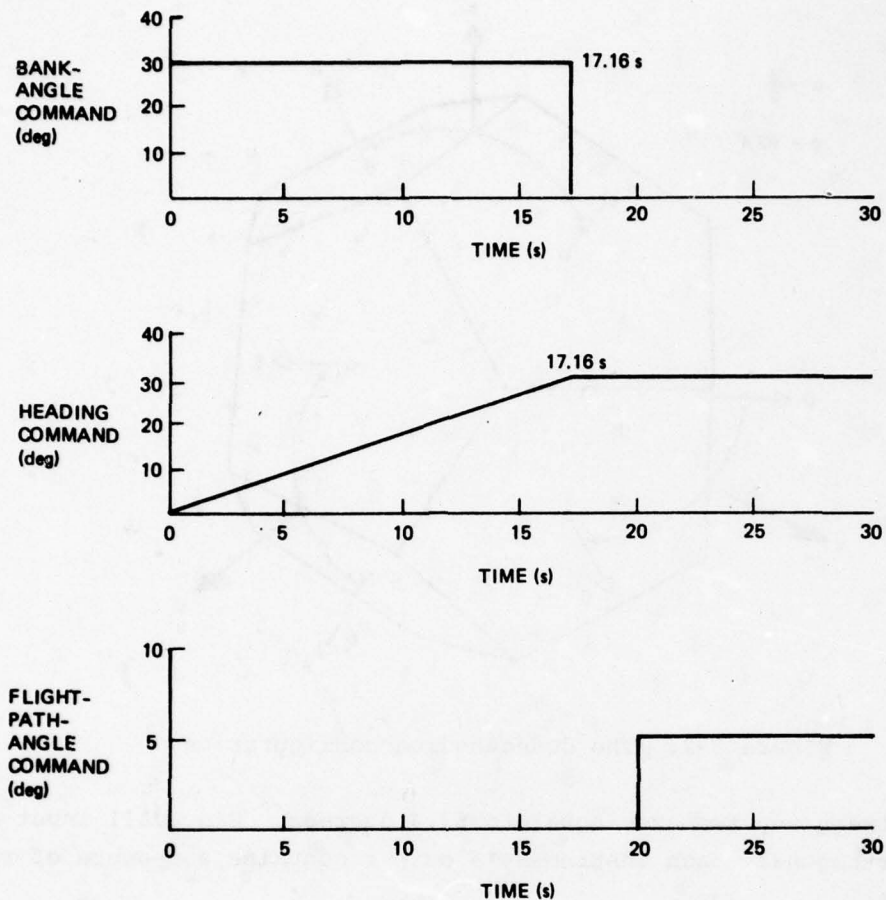
Figure 3-1.   Trajectory commands for short-duration
evaluation runs.

the simulation runs in a turbulent environment with the structural
modes excited, and in a nonturbulent environment solving only the rigid-
body equations of the vehicle. The effect of using navigation sensors
for flight-control purposes has also been assessed using the orthogonal-
triad configuration with laser or two-degree-of-freedom gyros.

Another sensor configuration selected for evaluation was the
Strapdown Inertial Reference Unit (SIRU), which employs six single-
degree-of-freedom gyros and six linear accelerometers. The instrument
input axes are arranged in a nonorthogonal pattern that corresponds to
the array of normals to the faces of a regular dodecahedron as shown
in Figure 3-2. This array is completely symmetrical, with the acute
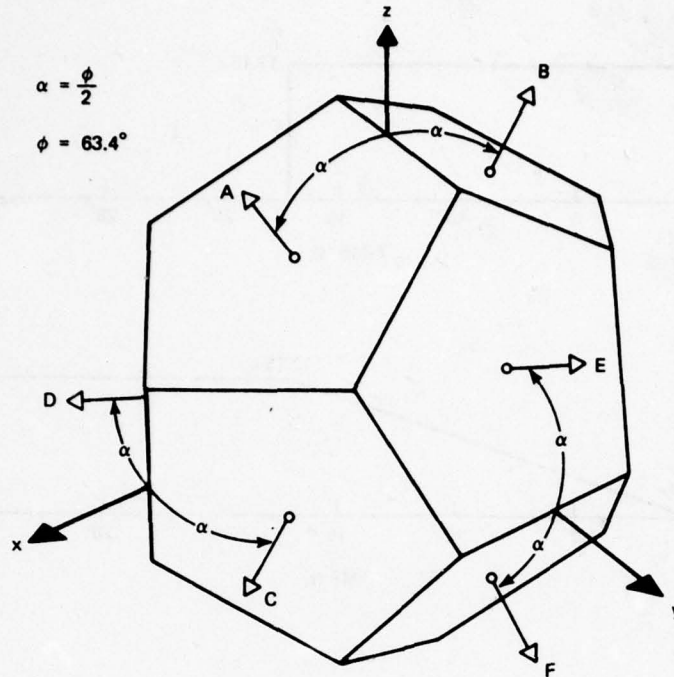
Figure 3-2. The dodecahedron configuration.

angle between any two axes equal to 63.4 degrees. Since all input axes
are nonorthogonal, each instrument's output contains a measure of redun-
dant data.

The question arises as to how a skewed sensor configuration is
evaluated using the MIRA simulation, which has only a laser or two-
degree-of-freedom gyro and accelerometer triad modeled. The approach
selected uses the covariance of the errors of the sensor outputs, which
are computed relative to an orthogonal triad. For example, the error-
covariance matrix of an orthogonal triad is $\sigma_e^2[I_0]$, assuming identical
instruments along each axis. It is shown in Reference 9 that, relative
to an orthogonal triad, the error-covariance matrix of the dodecahedron
configuration is $0.5\sigma_e^2[I_0]$. A nominal set of error coefficients has
been selected for the instruments of the orthogonal triad. These
coefficients are adjusted by the square root of 0.5 to account for the
effect due to the orientation of the sensors in the dodecahedron con-
figuration.

The last configuration selected for evaluation uses four two-
degree-of-freedom gyros with the gyro spin axes each normal to one of
the faces of a regular semi-octahedron. The sensor-measurement axes
are oriented such that they all lie on the surface of a cone where the

30

four spin axes lie. Figure 3-3 shows the orientation of the spin axes relative to the octahedron, and Figure 3-4 shows the orientation of the measurement axes relative to the spin axes. On a performance basis, the
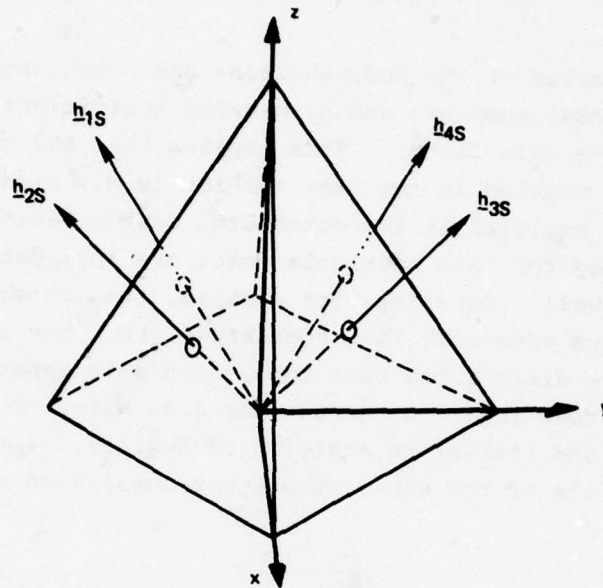

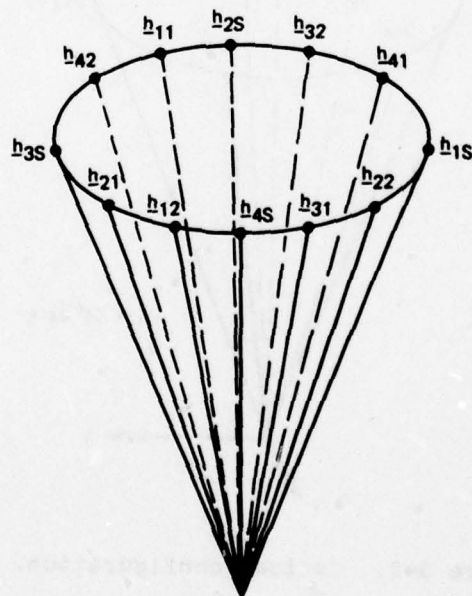Figure 3-3. Orientation of spin axes for the octahedron configuration.

Figure 3-4. Orientation of spin and measurement axes for the octahedron configuration.

31

the error-covariance matrix is $0.612\sigma_e^2[I_0]$, which is quite close to that of the dodecahedron configuration.[10] Therefore, when evaluating this configuration with the MIRA simulation, the two-degree-of-freedom error coefficients of the orthogonal triad were adjusted by the square root of 0.612.

In the evaluation of the dodecahedron- and octahedron-sensor configurations, the accelerometer- and gyro-error coefficients have been adjusted by the same gain factor. This implies that the gyros and accelerometers are mounted in the same fashion (e.g., eight linear accelerometers are employed in the octahedron configuration). However, the results obtained for this particular case are applicable to other configurations as well. Consider, for example, the configuration shown in Figure 3-5, which uses only five accelerometers. The input axes of the instruments are distributed on a cone, each axis separated from its neighbor by 72 degrees in azimuth about the cone axis. The cone axis is the roll axis, and lies at an angle of 54 degrees, 44 minutes, 8 seconds from the surface of the cone. The error-covariance matrix for
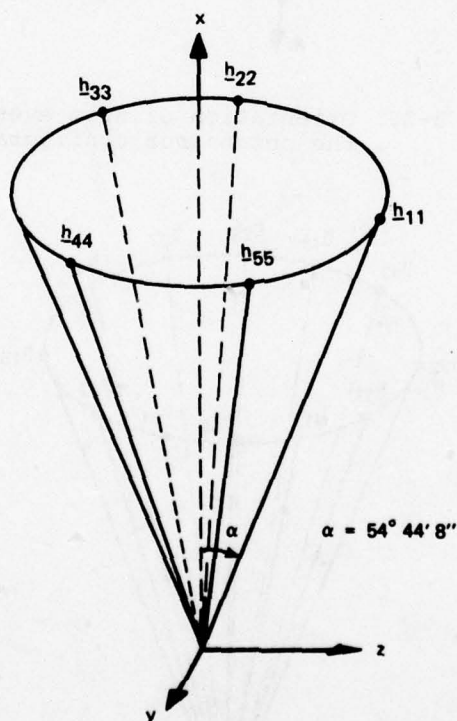
Figure 3-5. Conical configuration.

32

this configuration is $0.6\sigma_e^2[I_0]$, [7] which is extremely close to that obtained for the octahedron configuration. Thus, the result obtained from the MIRA simulation for the octahedron configuration would be applicable to the conical configuration as well.

All of the configurations selected were evaluated with the sensors colocated at FS313. This location is just forward of the vehicle cg, which is at FS320 for the particular vehicle configuration used. Table 3-2 gives the distances along the x- and z-body axes from the cg to the sensor package for this sensor location. This table also contains the body-axes distances from the vehicle cg to FS77 where the orthogonal triad configuration containing laser or two-degree-of-freedom gyros was evaluated to obtain an estimate of lever-arm effects upon the potential MIRA configurations. The pilot's station is located at FS119 as a point of reference. Both of these sensor locations were recommended in Reference 8 based upon the availability of space and the structural-mode characteristics of the vehicle.

Table 3-2. Sensor location relative to vehicle center of gravity.

Sensor Location	Distance from cg Along x-Body Axis (ft)	Distance from cg Along z-Body Axis (ft)
FS77	20.25	0.429
FS313	0.583	0.0

The effects of the three longitudinal- and three lateral-directional structural modes on the sensor responses are given in Table 3-3 for the two sensor locations just discussed. Parameters are given for the normal and lateral accelerometers, and the roll-, pitch-, and yaw-rate gyros. This information was taken from References 5 and 6, which do not include the effects of the modes on the longitudinal accelerometer since this instrument is not used for flight-control purposes. Therefore, the effect of the modes on this sensor has been assumed to be negligible. The effect of the modes on the gyro signals is given by the product of the coefficients in Table 3-3 and the mode rate in radians per second, while the effect on the accelerometer signals is given by the product of the appropriate coefficients and the mode acceleration in rad/s^2. The nominal frequencies of the longitudinal modes are 71.0, 87.5, and 141.0 radians per second, while those of the lateral-directional modes

33

Table 3-3. Aeroelastic coefficients of sensor responses.

Longitudinal Sensors					
Sensor	Location	Units	Coefficient of First Longitudinal Mode	Coefficient of Second Longitudinal Mode	Coefficient of Third Longitudinal Mode
Normal Accelerometer	FS77	ft	$4.774(10^{-3})$	$-1.467(10^{-3})$	$-8.333(10^{-4})$
	FS313	ft	$-1.840(10^{-3})$	$5.006(10^{-3})$	$-3.075(10^{-3})$
Pitch-Rate Gyro	FS77	rad	$-3.0608(10^{-4})$	$2.239(10^{-3})$	$-1.14(10^{-4})$
	FS313	rad	$-2.33 \ (10^{-4})$	$2.64 \ (10^{-4})$	0.0

Lateral-Directional Sensors					
Sensor	Location	Units	Coefficient of First Lateral-Directional Mode	Coefficient of Second Lateral-Directional Mode	Coefficient of Third Lateral-Directional Mode
Lateral Accelerometer	FS77	ft	0.0	0.0	$-3.885(10^{-4})$
	FS313	ft	0.0	0.0	$9.066(10^{-5})$
Roll-Rate Gyro	FS77	rad	$-5.5 \ (10^{-4})$	$6.3 \ (10^{-4})$	$2.9 \ (10^{-3})$
	FS313	rad	$-3.33(10^{-4})$	$5.333(10^{-4})$	$2.267(10^{-3})$
Yaw-Rate Gyro	FS77	rad	0.0	0.0	$-1.4(10^{-3})$
	FS313	rad	0.0	0.0	$-3.5(10^{-4})$

are 39.7, 67.6, and 80.8 radians per second. The lateral accelerometer and yaw-rate gyro are affected by only the highest frequency lateral-directional mode, while the roll-rate-gyro signal is influenced by all three lateral-directional modes. The three longitudinal-structural modes modeled influence both the pitch-rate gyro and normal accelerometer signals.

A nominal set of parameters was selected for the laser-gyro, quartz-flexure-accelerometer, and two-degree-of-freedom-gyro models for the MIRA evaluation runs. These parameters are given in Tables 3-4, 3-5, and 3-6. The nominal parameter set was used for each instrument of the orthogonal triad programmed in the MIRA simulation, with the sign of the error parameters selected to be positive or negative with equal probability to introduce some randomness into the parameter-selection process. The same set of accelerometer parameters was used

Table 3-4. Ring-laser-gyro nominal parameters.

Parameter	Value
Scale Factor	1.57 $\widehat{sec}$/pulse
Bias	0.01 deg/h
Scale-Factor Error	5 ppm
Misalignment Coefficients	$5(10^{-5})$ rad

Table 3-5. Quartz-flexure-accelerometer
nominal parameters.

Parameter	Value
Scale Factor	32,000 pps/g
Bias	50 μg
Scale-Factor Error	100 ppm
Misalignment Coefficients	$5(10^{-5})$ rad
Cross-Coupling Coefficient	$1.96(10^{-5})$ rad/g
Scale-Factor Nonlinearity Coefficient	40 $μg/g^2$

with either the laser or two-degree-of-freedom gyros. For configurations
other than the orthogonal triad, the magnitude of the error coefficients
was adjusted by the square root of the coefficient of the error-covariance
matrix.

It has been assumed for the orthogonal triad with two-degree-of-
freedom gryos that one instrument is aligned with the x-instrument out-
put axis along the x-body axis, to measure the roll rate; and the y-body
axis, to measure the pitch-rate signal. The spin axis of this instru-
ment is down, parallel to the vehicle z-body axis. The yaw-rate signal
was obtained from the y-output axis of a two-degree-of-freedom gyro
mounted with the x-instrument axis parallel to the y-body axis, the
y-instrument axis parallel to the z-body axis, and the gyro spin axis
parallel to the x-body axis. The x-axis output signal of this gyro was
not used in the simulation. It has been assumed that the instruments
are mounted on the vehicle in this fashion to minimize the effects of
the g-dependent errors on the gyro output signals.

35

Table 3-6. Two-degree-of-freedom-gyro nominal parameters.

Parameter	Units	x-Output-Axis Value	y-Output-Axis Value	Source
Scale Factor	sec/pulse	1.57	1.57	
Bias	deg/h	0.01	0.01	
Scale-Factor Error	ppm	50	50	
Misalignment Coefficients	rad	10^{-4}	10^{-4}	ω_{g_y}, ω_{g_z} for x-output ω_{g_x}, ω_{g_z} for y-output
g-Dependent Errors	deg/h/g	0.02 0.04 0.01	0.04 0.02 0.01	a_{g_x} a_{g_y} a_{g_z}
g^2-Dependent Errors	deg/h/g^2	0.02 0.0 0.005	0.0 0.02 0.005	$a_{g_x}^2$ $a_{g_y}^2$ $a_{g_z}^2$
g×g-Dependent Errors	deg/h/g^2	0.01 0.04 0.04	0.01 0.04 0.04	a_{g_x}, a_{g_y} a_{g_y}, a_{g_z} a_{g_x}, a_{g_z}
ω×ω-Dependent Errors	deg/h/$(rad/s)^2$	0.0 80 20	0.0 20 80	ω_{g_x}, ω_{g_y} ω_{g_y}, ω_{g_z} ω_{g_z}, ω_{g_x}

3.2 Simulation Results

This section contains the results obtained for the cases described in Section 3.1, using the CSDL-designed and developed MIRA simulation. The 1-hour runs designed to evaluate the navigation performance of the candidate MIRA systems will be discussed first.

Figure 3-6 shows the system responses obtained with the orthogonal-triad configuration using two-degree-of-freedom gyros located near the cg of the vehicle at FS313. The results obtained for this case are typical of those obtained for the other cases in the study.

The autopilot causes the vehicle to follow the desired true-north trajectory at constant speed and altitude very well in the turbulent environment over the duration of the flight. The Euler
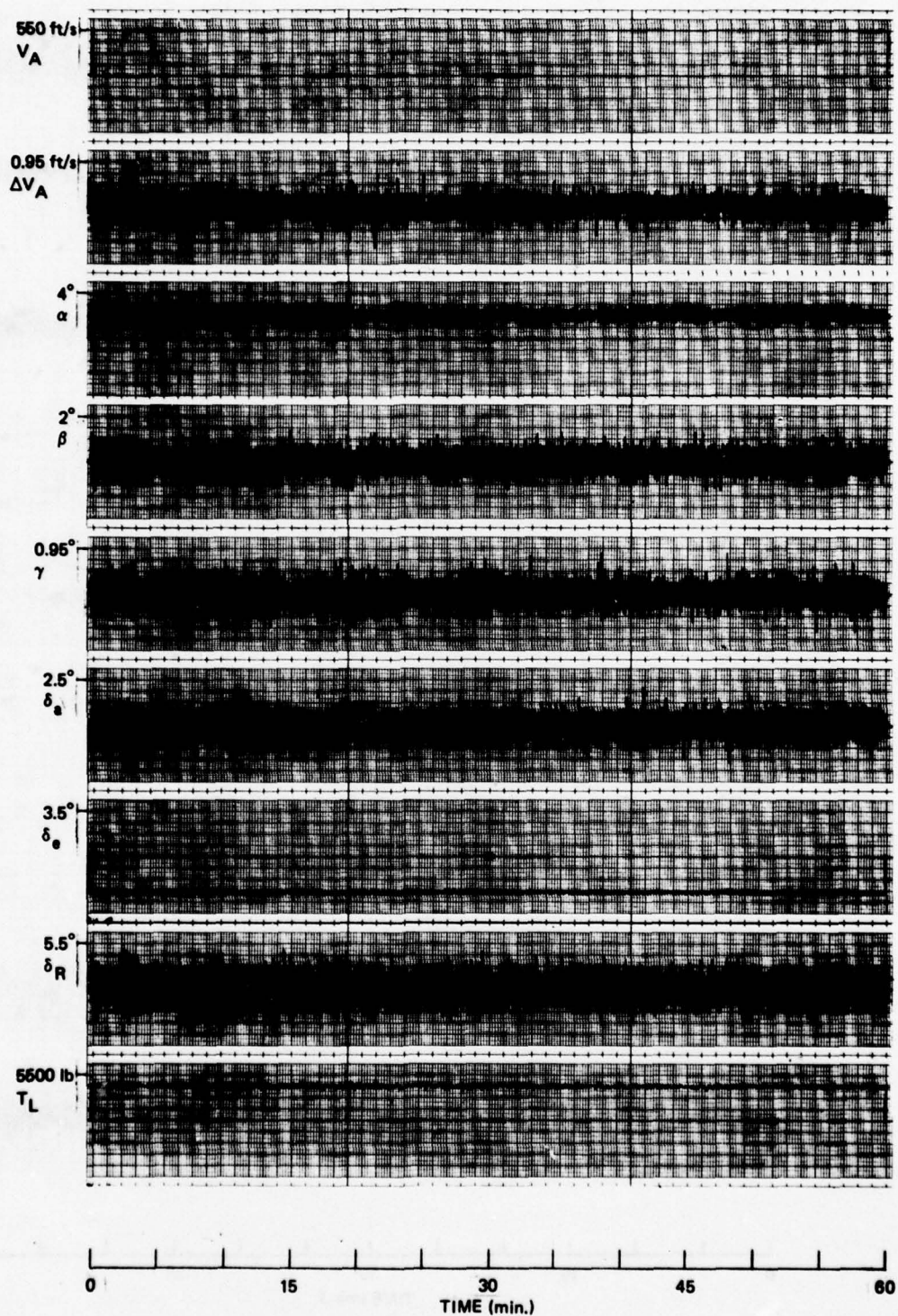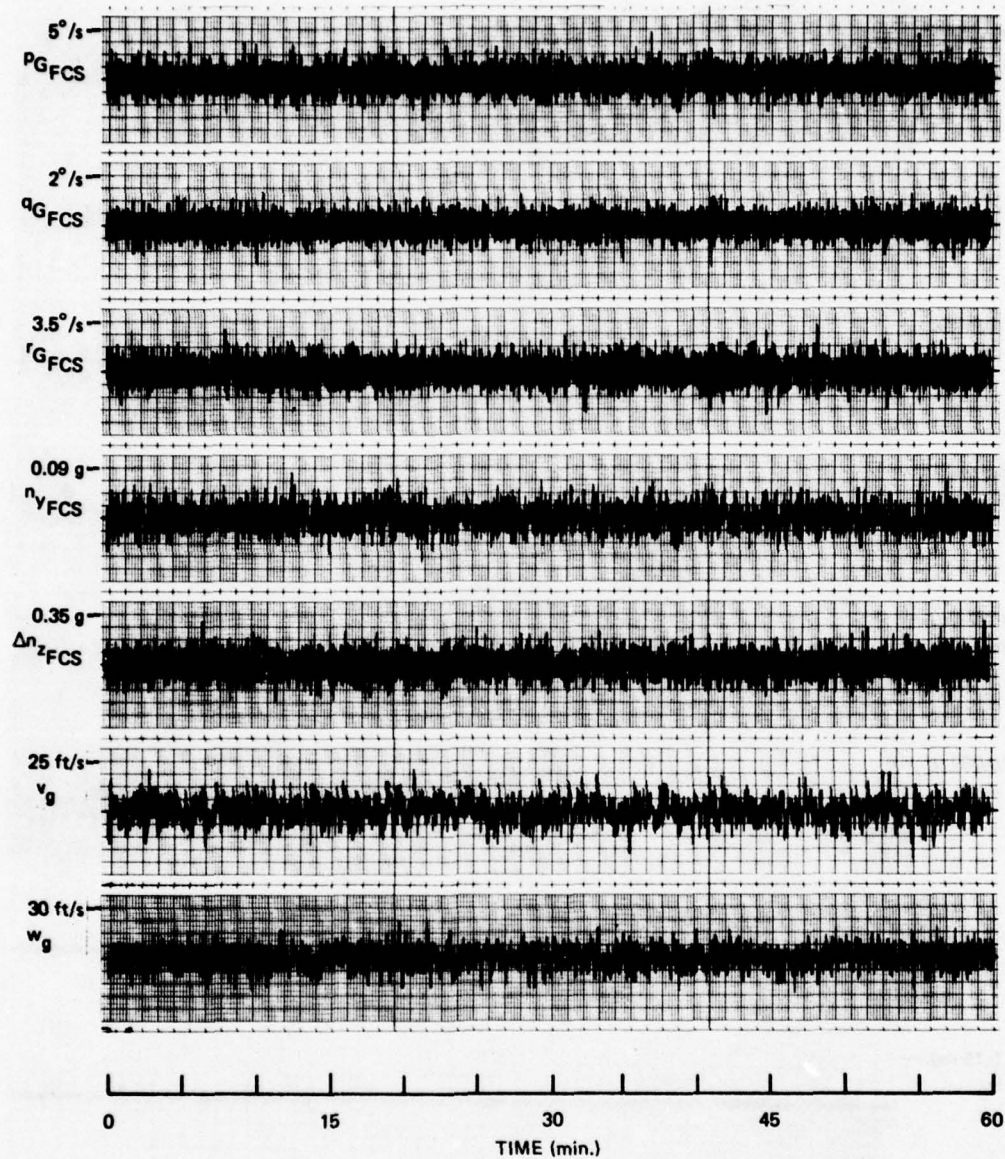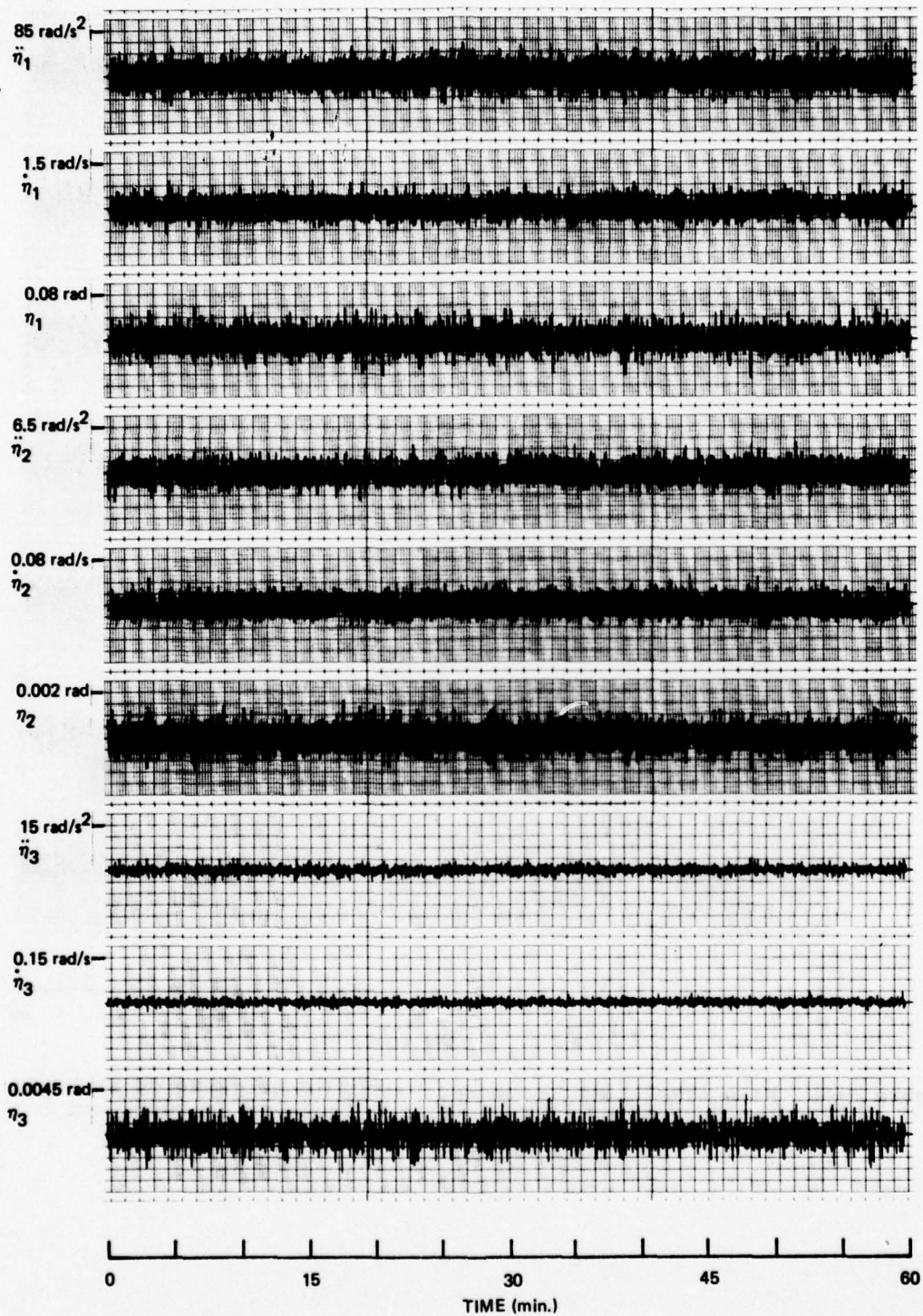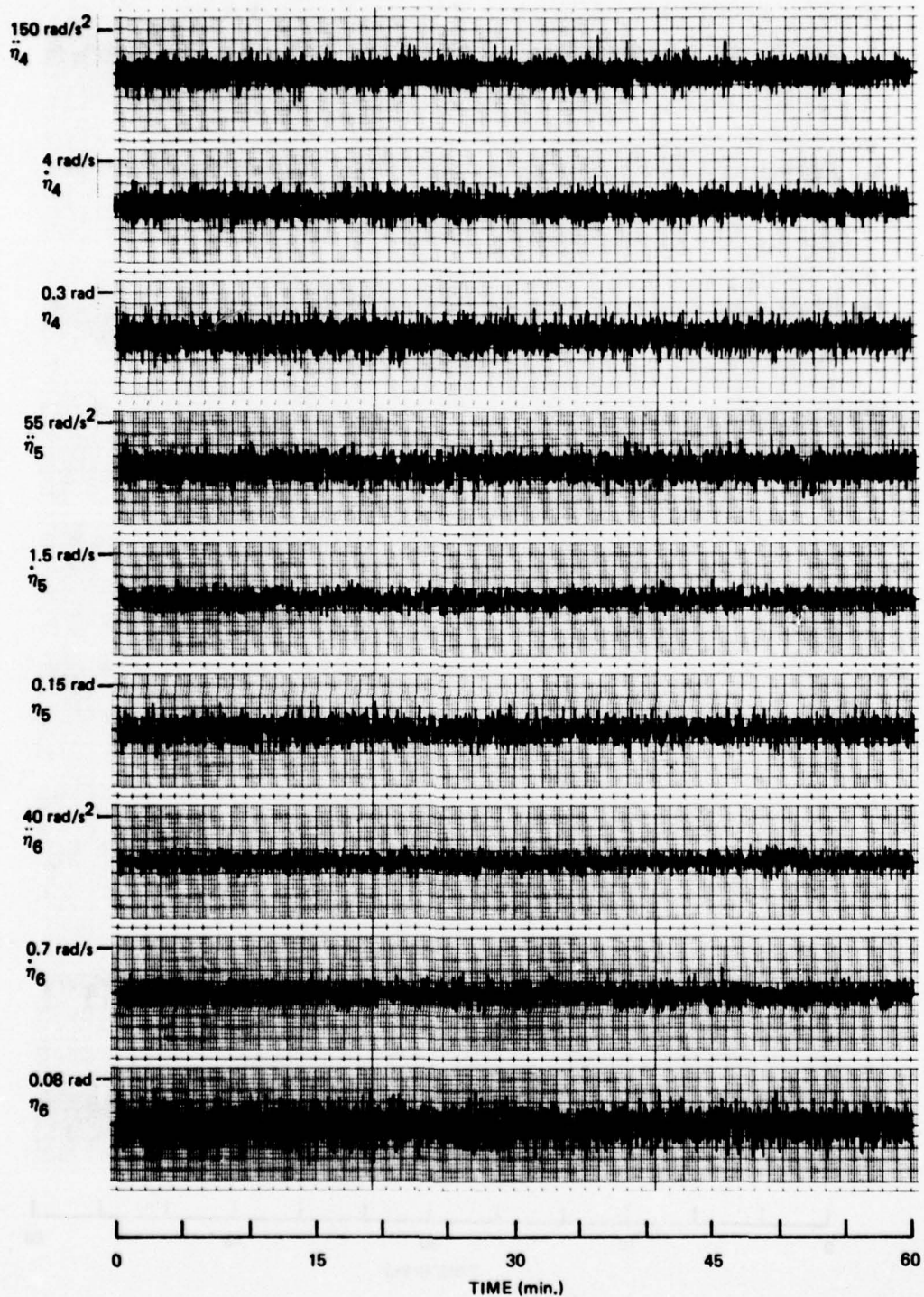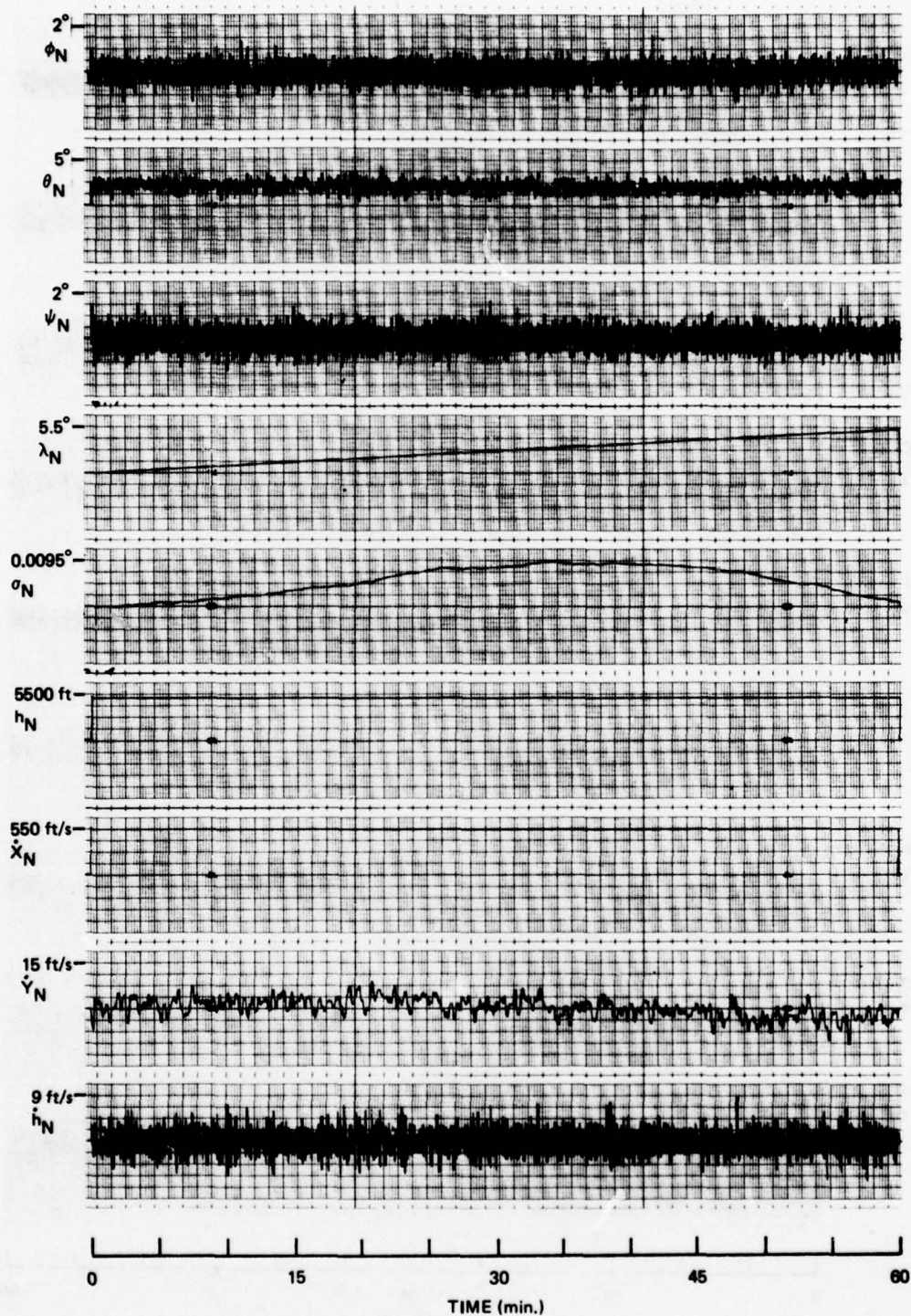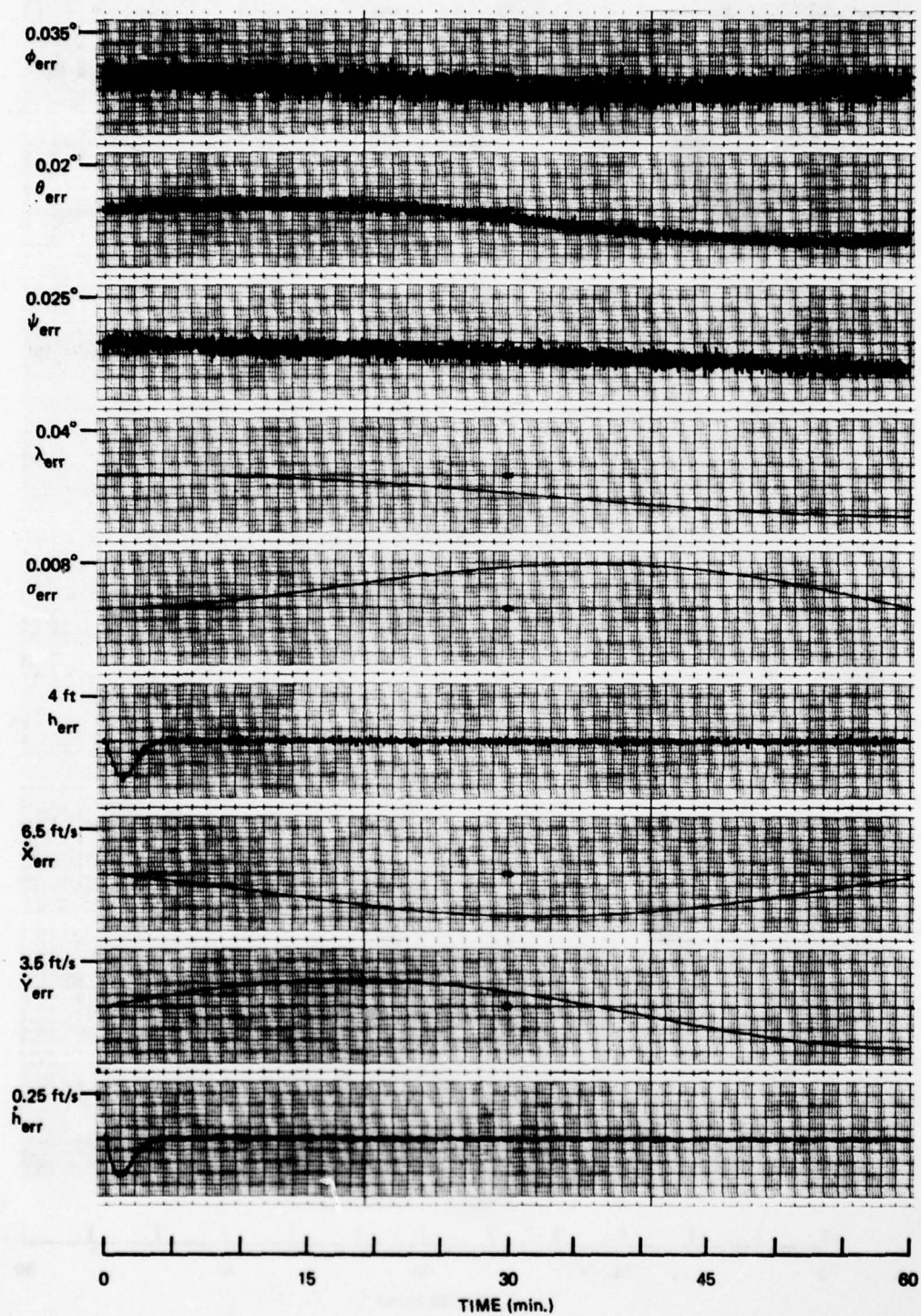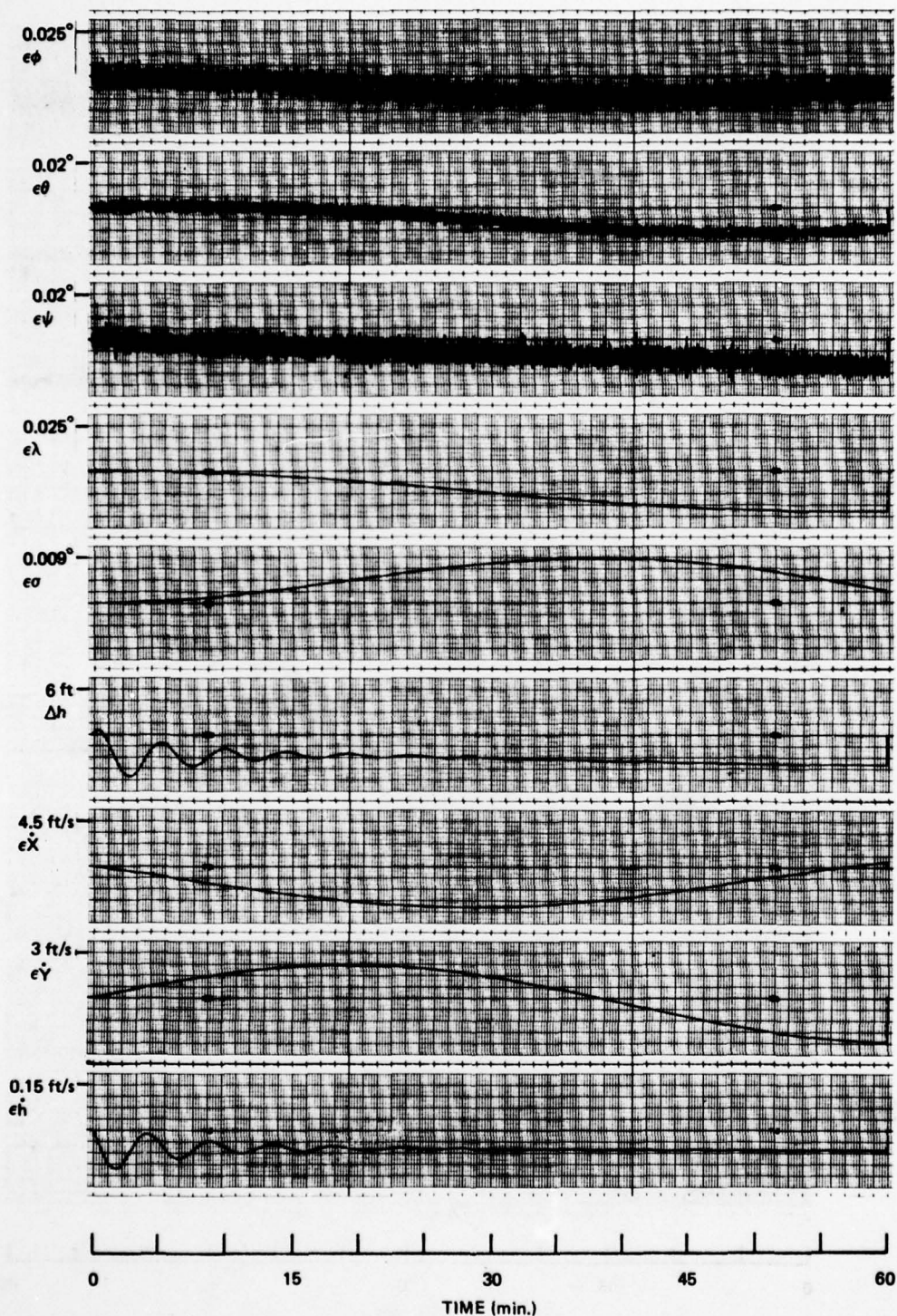
Figure 3-6. MIRA simulation responses: triad configuration at FS313;
two-degree-of-freedom gyros; 1-hour run in turbulent
environment (sheet 1 of 8).
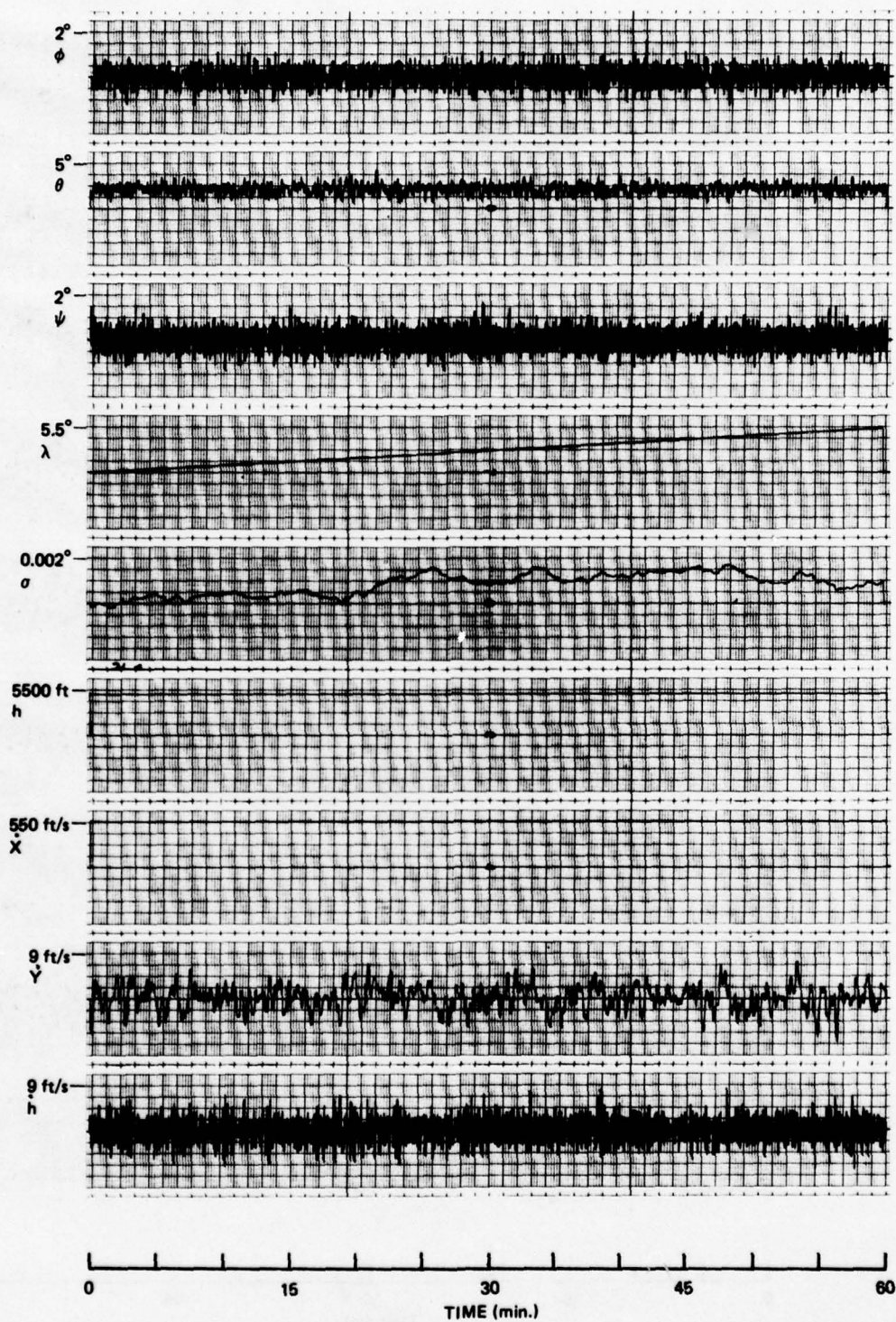
37

Figure 3-6. MIRA simulation responses: triad configuration at FS313;
two-degree-of-freedom gyros; 1-hour run in turbulent
environment (sheet 2 of 8).

38

Figure 3-6. MIRA simulation responses: triad configuration at FS313;
two-degree-of-freedom gyros; 1-hour run in turbulent
environment (sheet 3 of 8).

39

Figure 3-6. MIRA simulation responses: triad configuration at FS313;
two-degree-of-freedom gyros; 1-hour run in turbulent
environment (sheet 4 of 8).

Figure 3-6.   MIRA simulation responses: triad configuration at FS313;
two-degree-of-freedom gyros; 1-hour run in turbulent
environment (sheet 5 of 8).

Figure 3-6.   MIRA simulation responses: triad configuration at FS313;
two-degree-of-freedom gyros; 1-hour run in turbulent
environment (sheet 6 of 8).

42

Figure 3-6. MIRA simulation responses: triad configuration at FS313; two-degree-of-freedom gyros; 1-hour run in turbulent environment (sheet 7 of 8).

Figure 3-6. MIRA simulation responses: triad configuration at FS313;
two-degree-of-freedom gyros; 1-hour run in turbulent
environment (sheet 8 of 8).

44

angles deviate less than ±1.5 degrees from their trim values, as do the angle of attack and sideslip angle. The speed of the vehicle is maintained within 1 foot per second, while the maximum deviation of the altitude from the 5000-foot trim value is 17 feet. Other flight-profile variables of interest are the flight-path angle, which is less than 1 degree in magnitude, and the altitude rate and east ground velocity, which are less than 9 feet per second in magnitude. The horizontal tail and and throttle deflections, commanded to keep the vehicle on its trajectory, are of relatively small magnitude. The commanded lateral-directional controls are of much larger magnitude, approximately 5 degrees maximum for the rudder, and 2 degrees maximum for the aileron. However, these are not unreasonable values. Also presented in Figure 3-6 are the flight-control-sensor time histories. The yaw- and roll-rate signals are less than 2.5 degrees per second, and the pitch-rate-gyro signal less than 1 degree per second. The incremental normal acceleration is on the order of ±0.2 g, while the lateral acceleration peaks at 0.05 g.

The structural-mode accelerations, rates, and shapes are included in Figure 3-6 to give an indication of the magnitude and character of the excitations. The level of mode excitation is very nearly the same for all of the simulation runs. The effect of the modes on the sensor signals can be estimated from these time histories and the data contained in Table 3-3. For example, the effect of both the first and second longitudinal modes on the normal accelerometer signal is less than 0.006 g. The effect of the third longitudinal mode is even less, about 0.001 g. The maximum contribution to the pitch-rate-gyro signal is caused by the first longitudinal mode, and its magnitude is 0.024 degree per second. The roll-rate gyro is affected almost equally by the three lateral-directional modes with the respective peak contribution to the signal 0.1, 0.06, 0.1 degree per second. The yaw-rate gyro is affected by the third lateral-directional mode only, and the peak level of its effect is less than 0.01 degree per second. The same is true of the lateral accelerometer with the magnitude of the effect less than 0.0005 g.

Figure 3-6 also includes the output responses of the navigation-system model included in the MIRA simulation. These responses appear

to be almost duplicates of their vehicle counterparts. Perhaps the most noticeable differences are evident in the east ground velocity, which has a long-term bias in the navigation-system output; and longitude error, which is four times larger in magnitude, although it is an extremely small quantity.

The capability and accuracy of the navigation system is better understood and evaluated by considering error responses along with the outputs of the system rather than just the system responses alone. With this in mind, two sets of navigation-error variables have been included in Figure 3-6. One set is obtained by differencing the navigation-system outputs and the vehicle responses. The corresponding set of error signals obtained from the error-navigation algorithm (and due solely to the sensor errors) is also included for comparison. On the whole, the two sets of error responses agree remarkably well for this case, being almost identical overlays in most cases. The altitude- and altitude-rate-error signals do not agree, but this is due to the fact that the navigation system includes a third-order loop in the vertical channel, while that in the error-navigation algorithm is only second order. The navigation-system errors tend to be noisier due to the differencing with the true state of the vehicle. Although not evident from the responses of Figure 3-6, the Schuler period for the system shown is of the correct magnitude as determined from a 2-hour rather than a 1-hour run.

The comparative navigation performance of the other MIRA systems investigated was determined from the system-error responses obtained by differencing the navigation-system and vehicle outputs, as well as from the outputs of the error-navigation algorithm. These responses are presented in Figures 3-7 through 3-13 for the configuration presented previously in Table 3-1. The simulation runs in these figures are again 1-hour long.

The error responses given in Figure 3-7 represent a baseline case for the simulation runs performed in that they were obtained with an orthogonal-triad configuration located at FS313 in a nonturbulent environment with only the vehicle rigid-body equations being solved. The structural-mode equations of the vehicle were not solved. The responses for the corresponding system in a turbulent environment with the structural modes of the vehicle being excited are given in Figure 3-8.
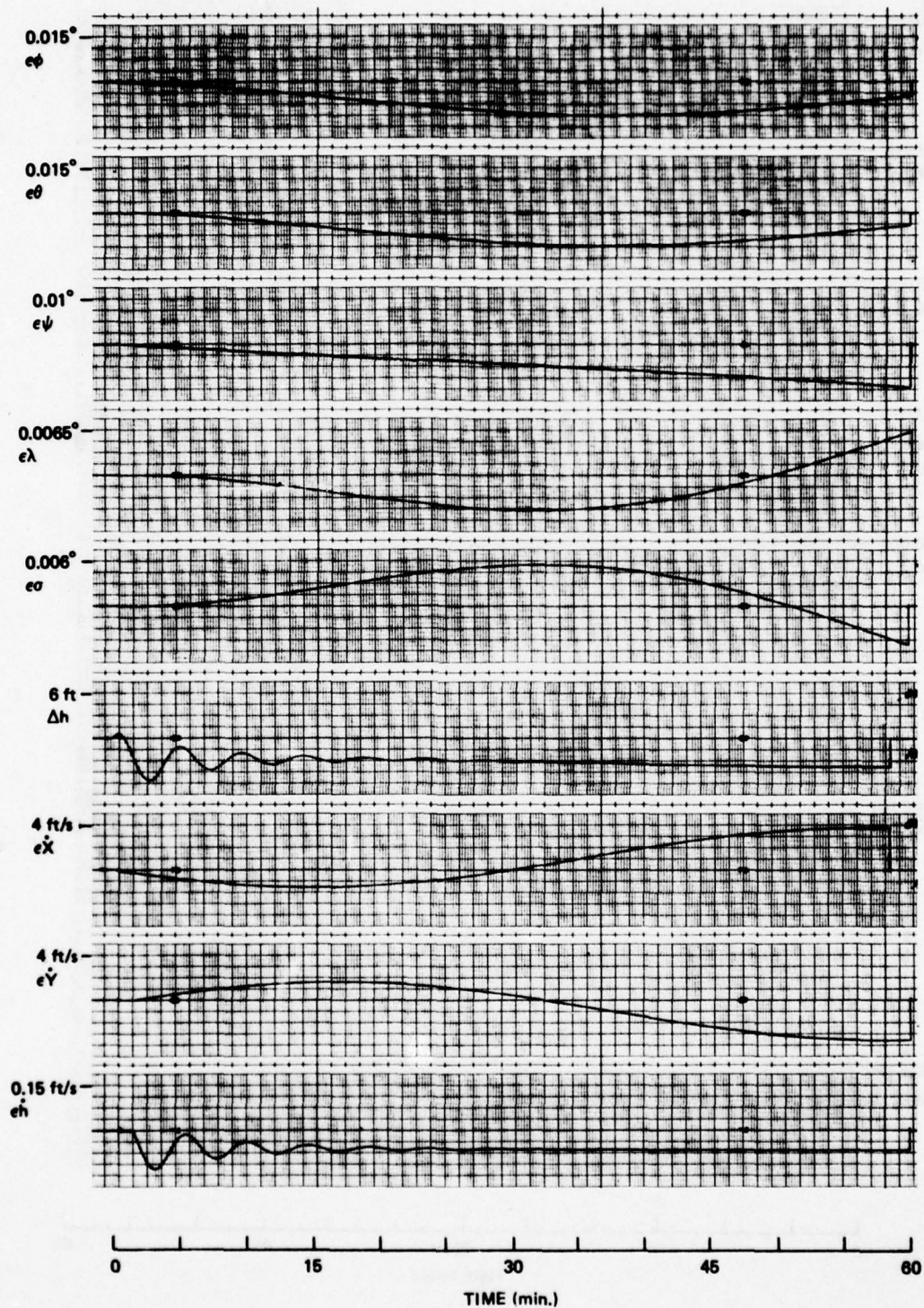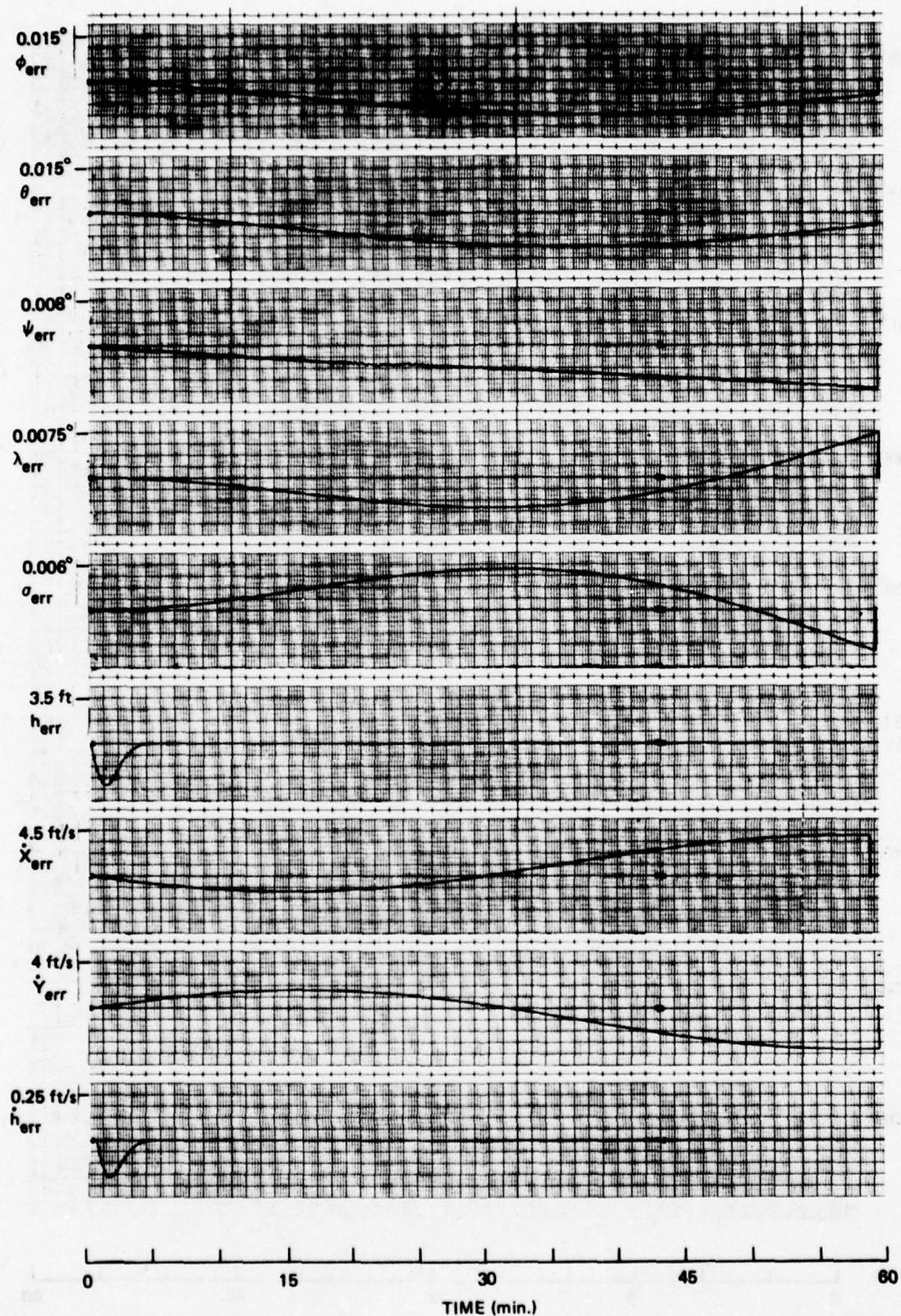
Figure 3-7. MIRA simulation responses: triad configuration at FS313;
laser gyros; 1-hour run in nonturbulent environment
without structural modes (sheet 1 of 2).

47

Figure 3-7.   MIRA simulation responses: triad configuration at FS313;
laser gyros; 1-hour run in nonturbulent environment
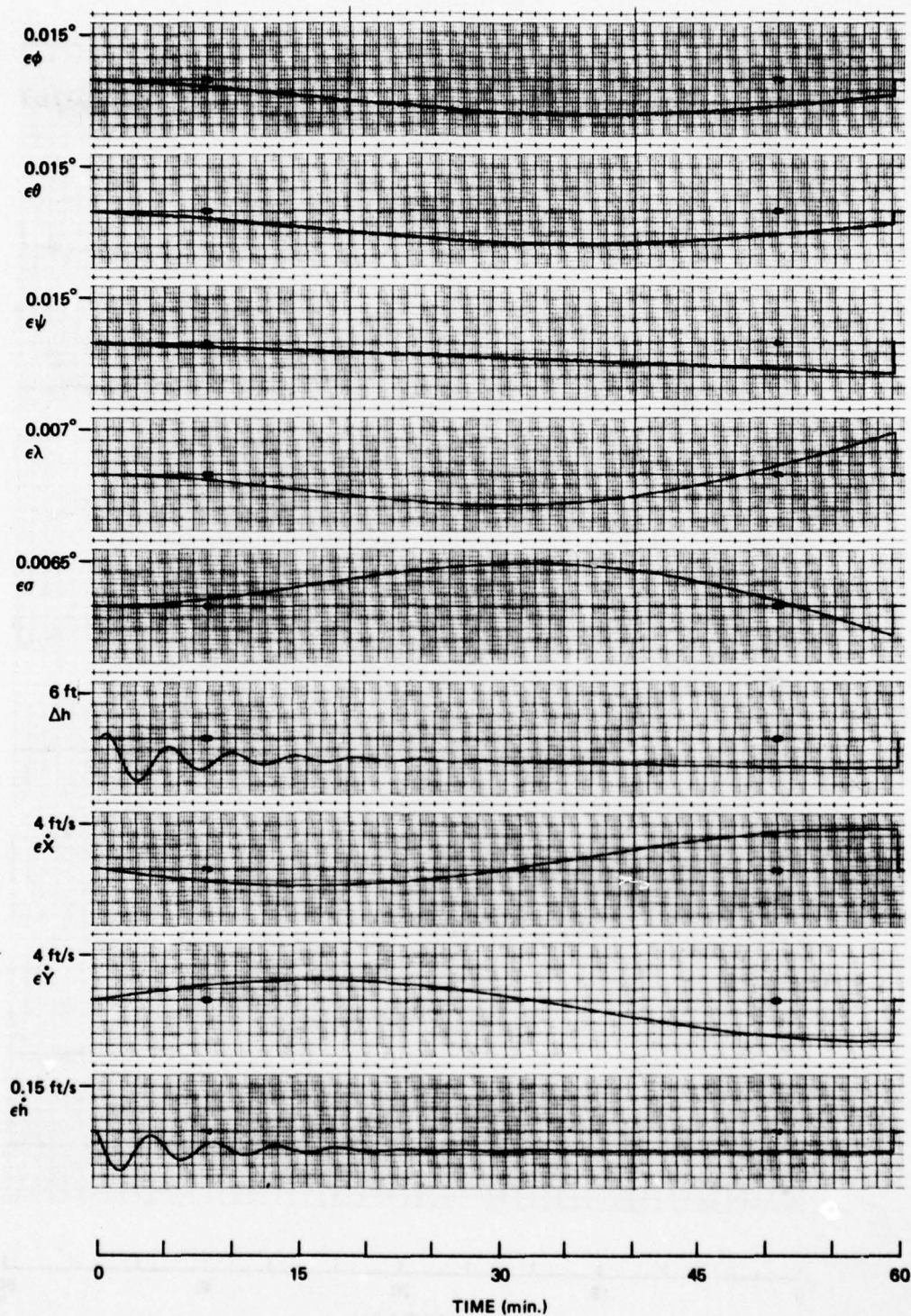without structural modes (sheet 2 of 2).

48

Figure 3-8. MIRA simulation responses: triad configuration at FS313; laser gyros; 1-hour run in turbulent environment (sheet 1 of 2).
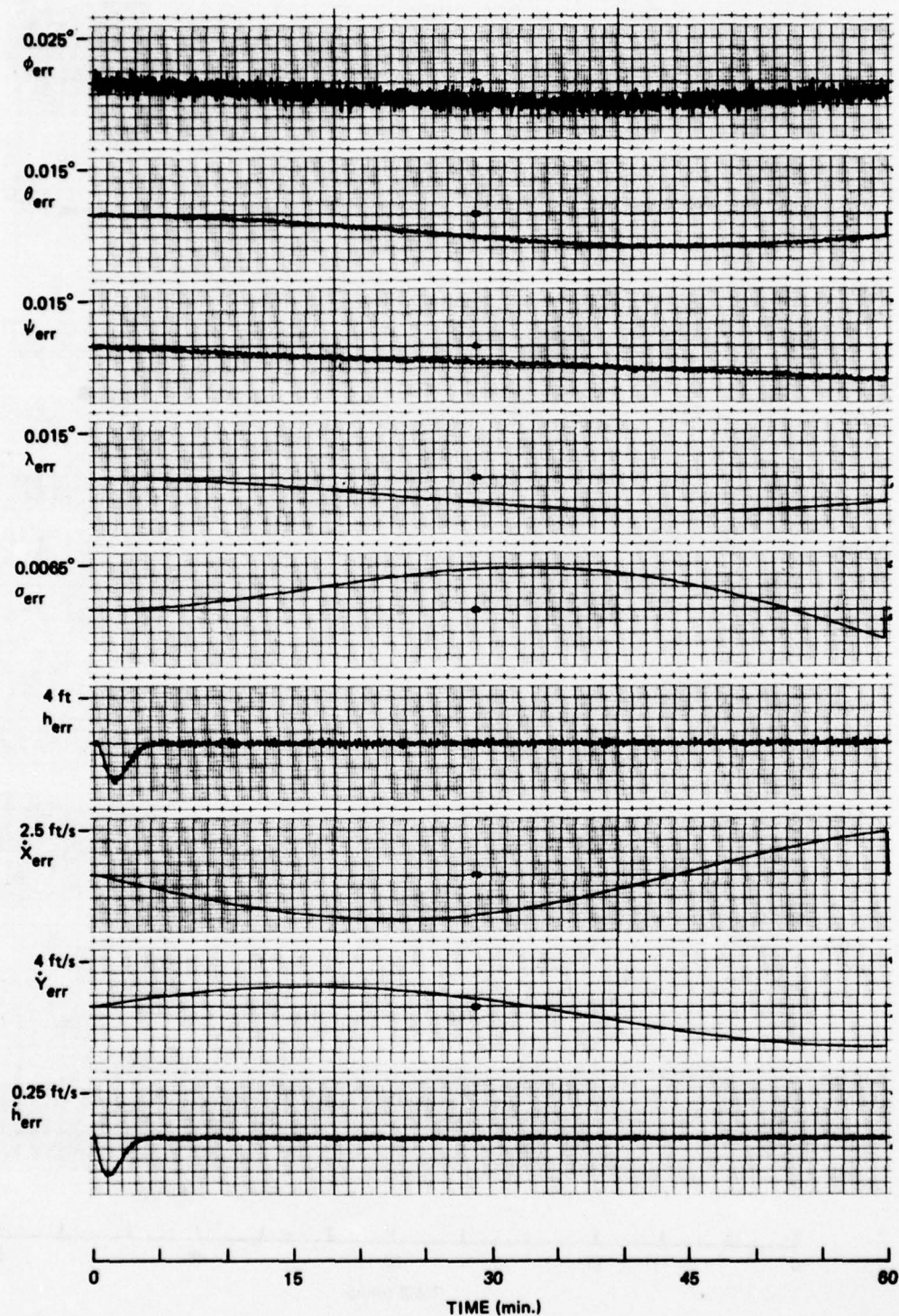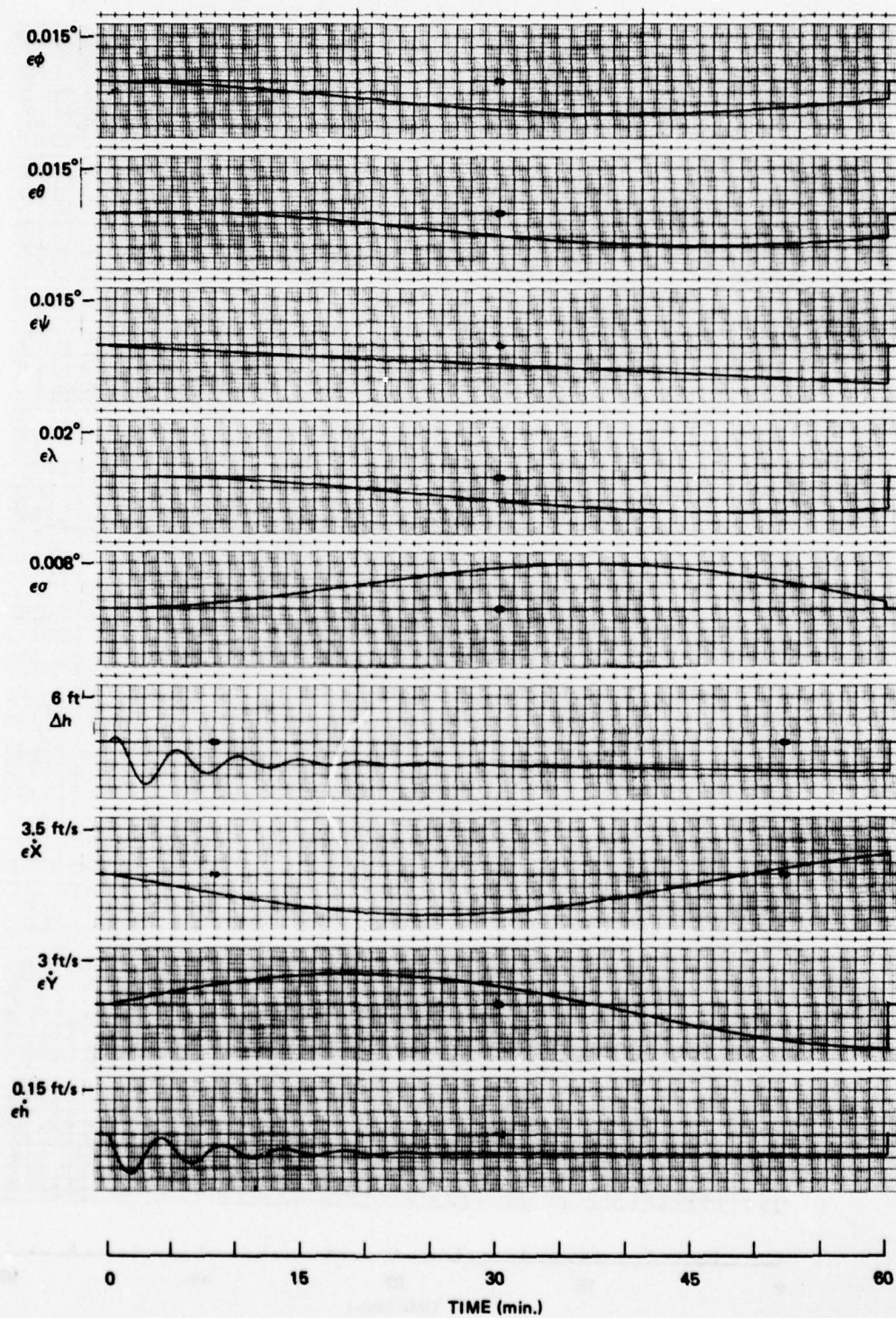
49

Figure 3-8. MIRA simulation responses: triad configuration at FS313;
laser gyros; 1-hour run in turbulent environment
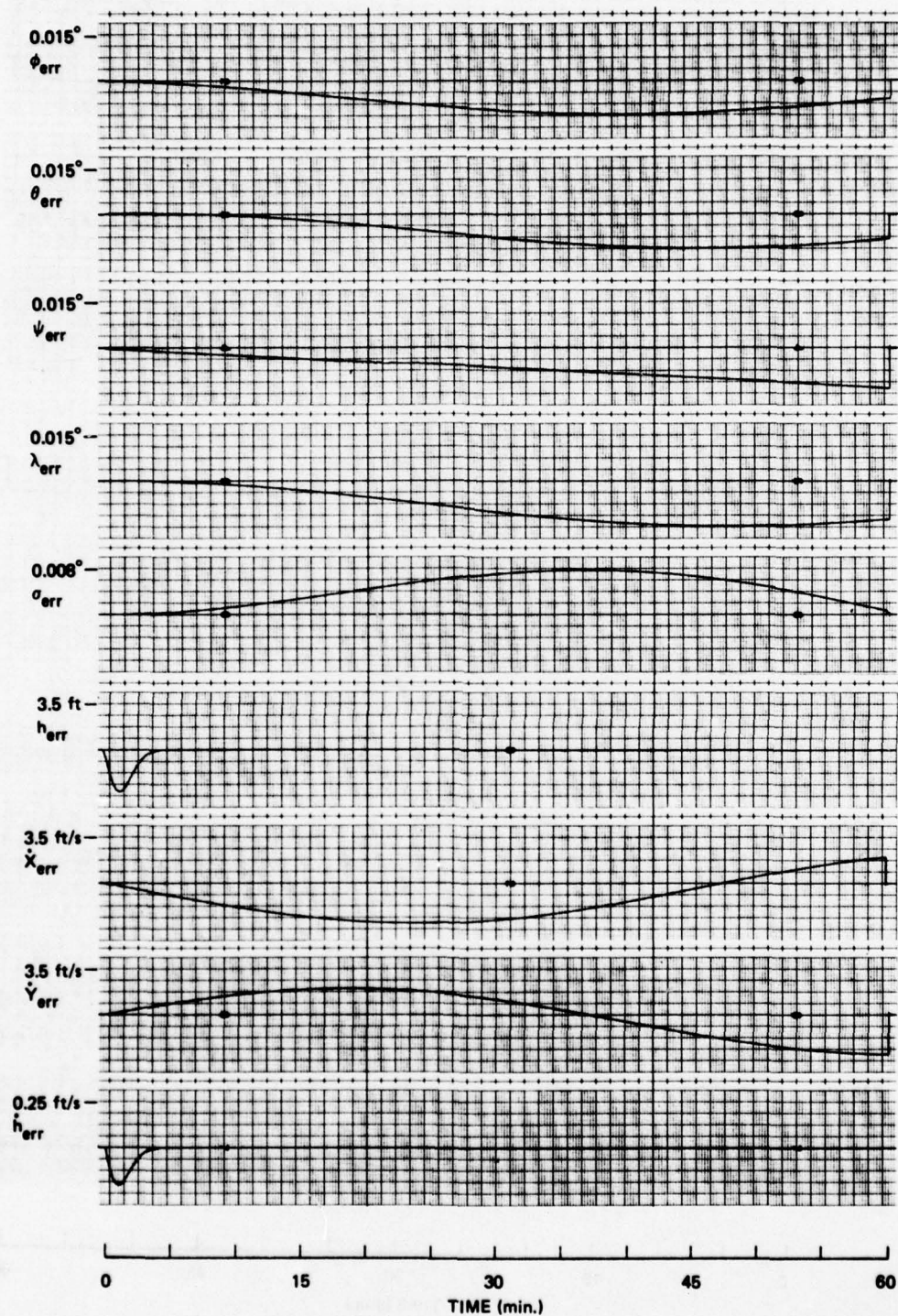(sheet 2 of 2).

Figure 3-9. MIRA simulation responses: triad configuration at FS313; two-degree-of-freedom gyros; 1-hour run in nonturbulent environment without structural modes (sheet 1 of 2).

51

Figure 3-9. MIRA simulation responses: triad configuration at FS313; two-degree-of-freedom gyros; 1-hour run in nonturbulent environment without structural modes (sheet 2 of 2).
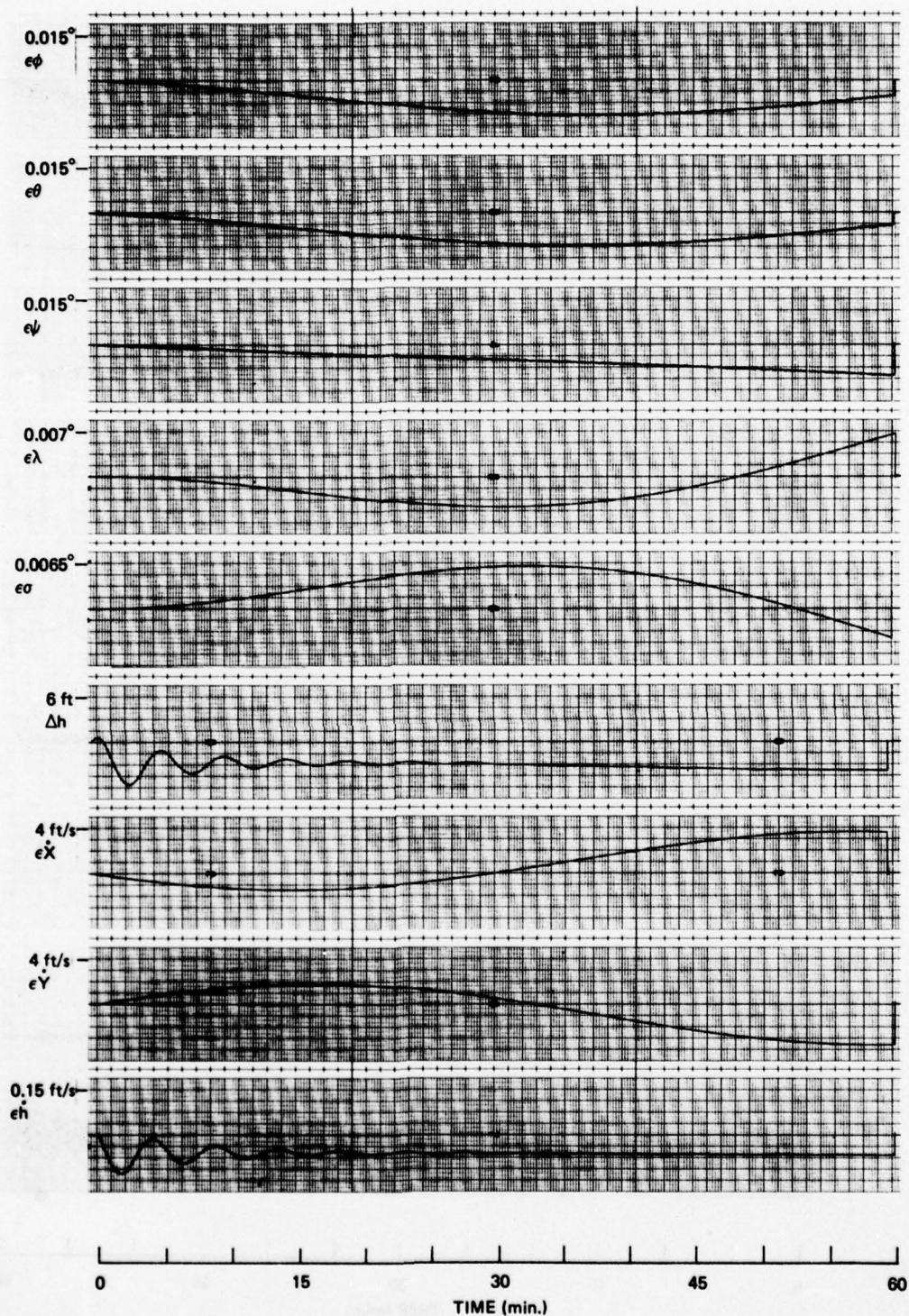
Figure 3-10. MIRA simulation responses: triad configuration at FS77;
laser gyros; 1-hour run in turbulent environment
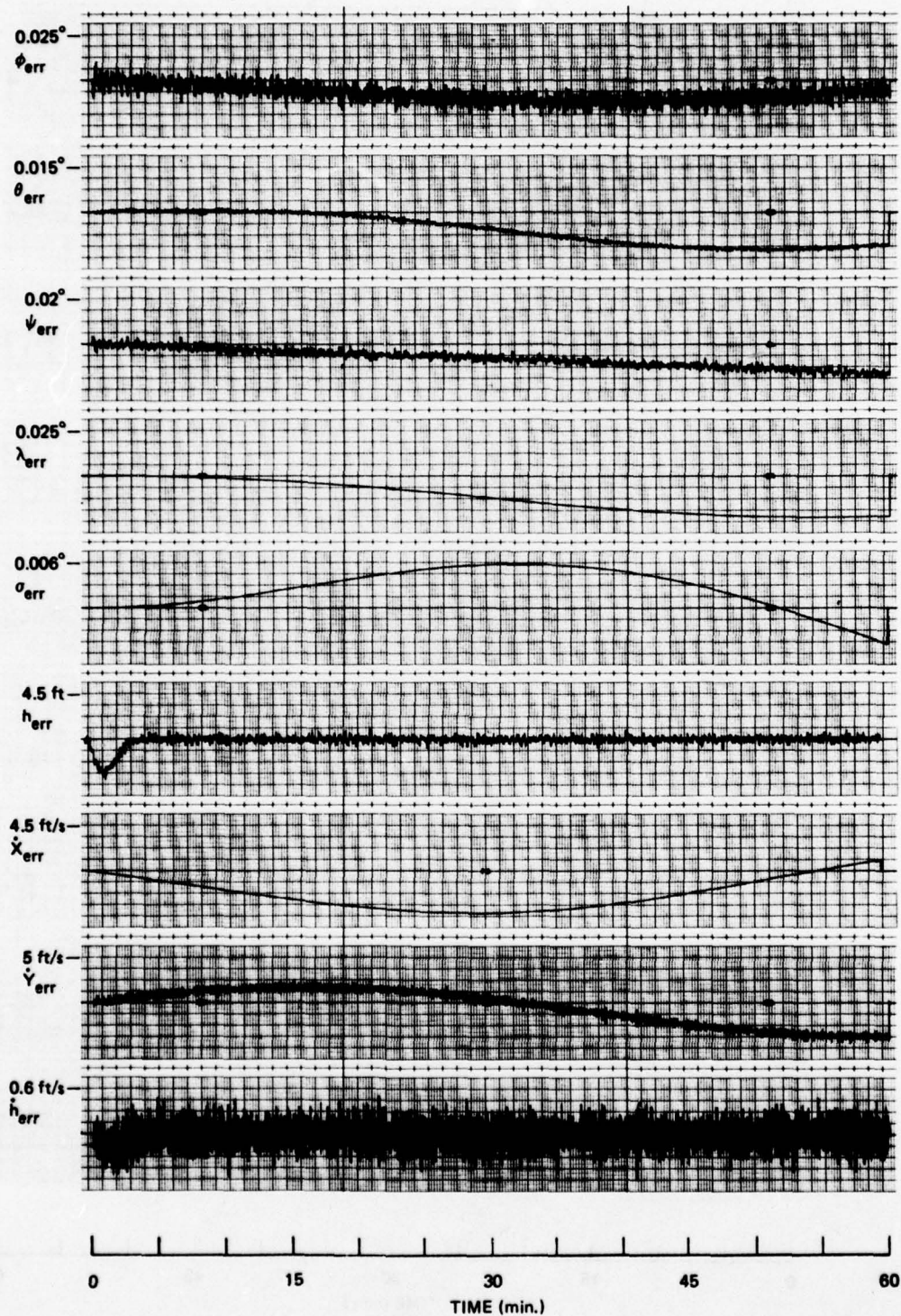(sheet 1 of 2).

53

Figure 3-10.   MIRA simulation responses: triad configuration at FS77; laser gyros; 1-hour run in turbulent environment (sheet 2 of 2).
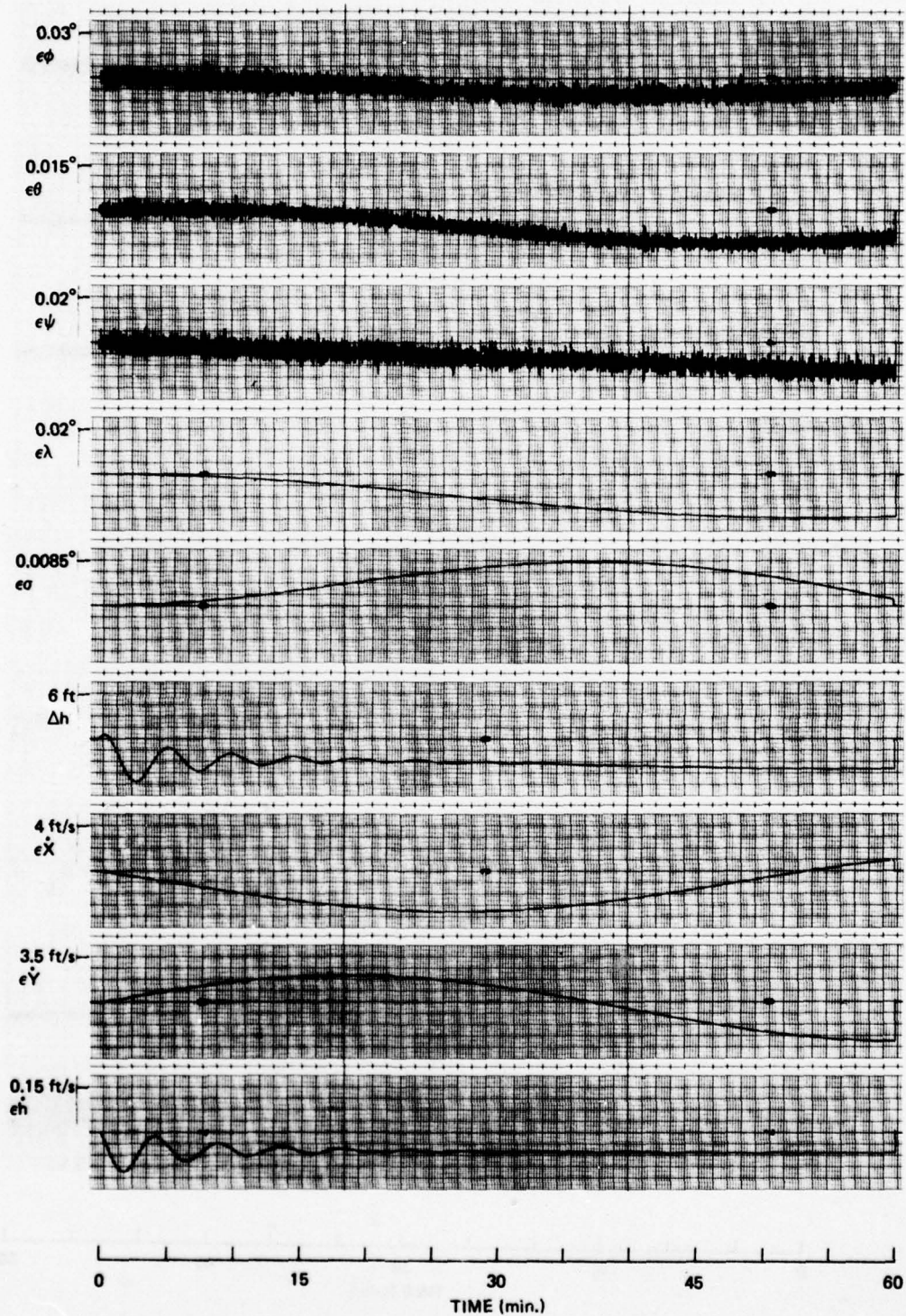
Figure 3-11. MIRA simulation responses: triad configuration at FS77;
two-degree-of-freedom gyros; 1-hour run in turbulent
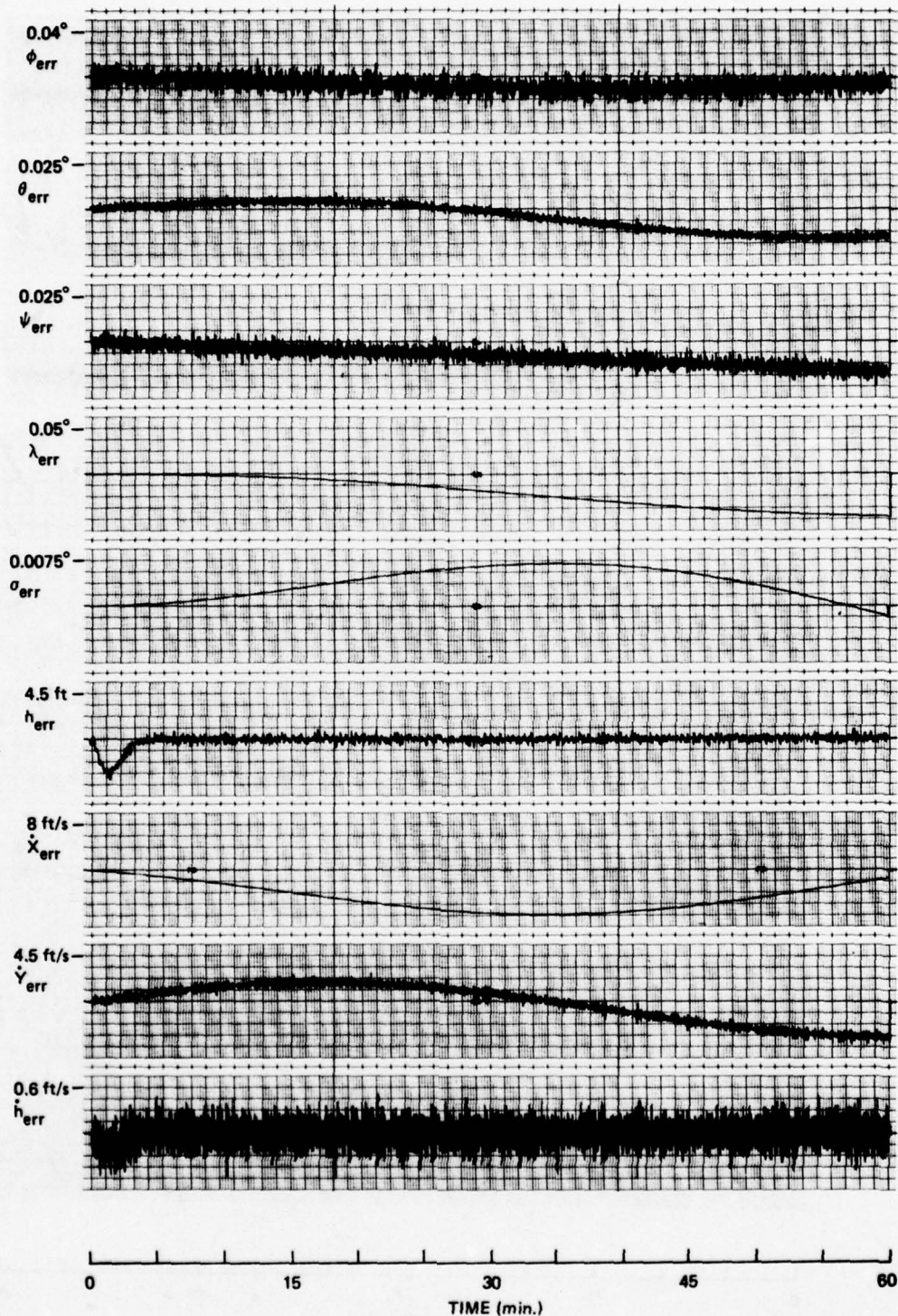environment (sheet 1 of 2).

55

Figure 3-11. MIRA simulation responses: triad configuration at FS77; two-degree-of-freedom gyros; 1-hour run in turbulent environment (sheet 2 of 2).
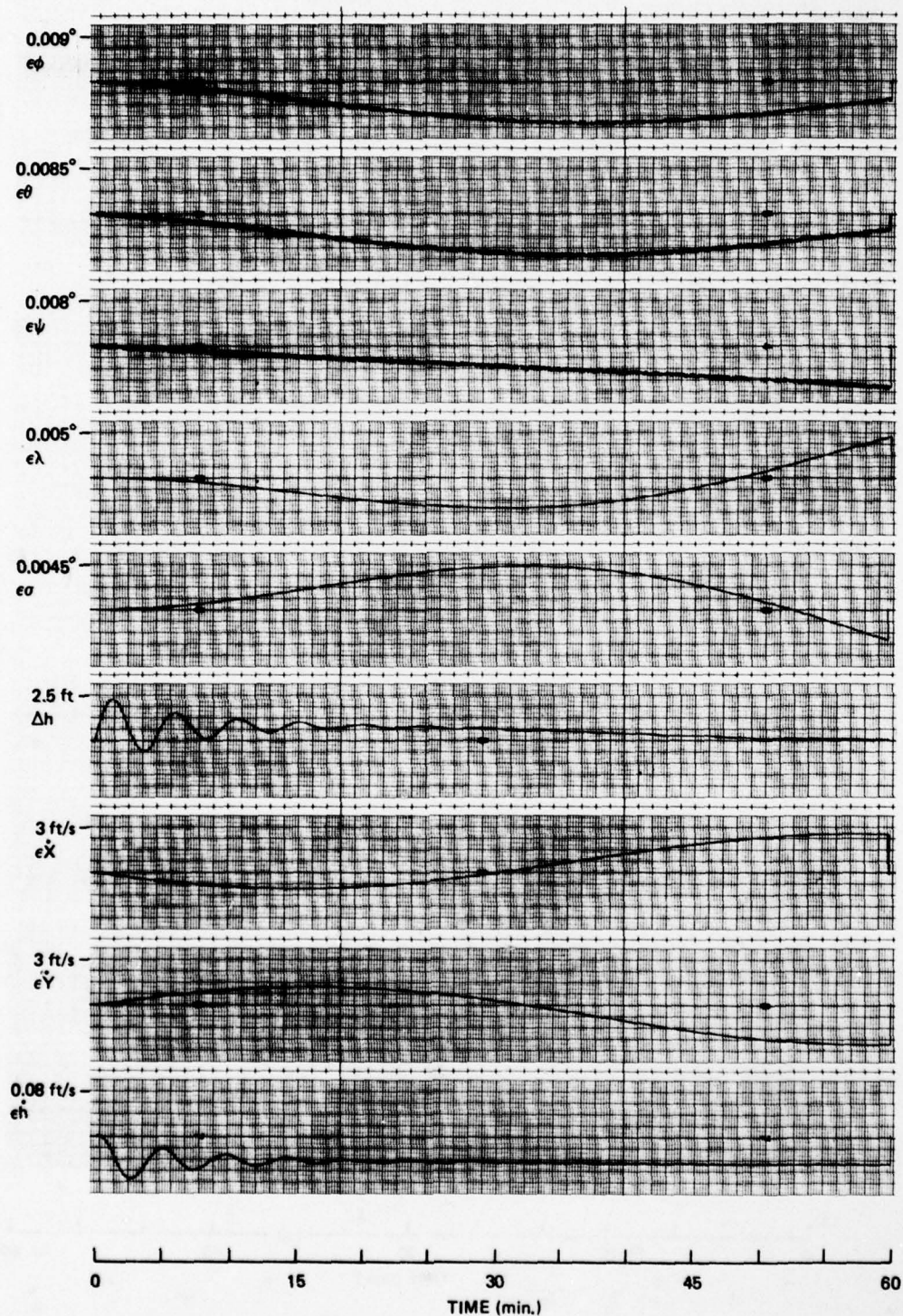
56

Figure 3-12. MIRA simulation responses: dodecahedron configuration at FS313; laser gyros; 1-hour run in turbulent environment (sheet 1 of 2).
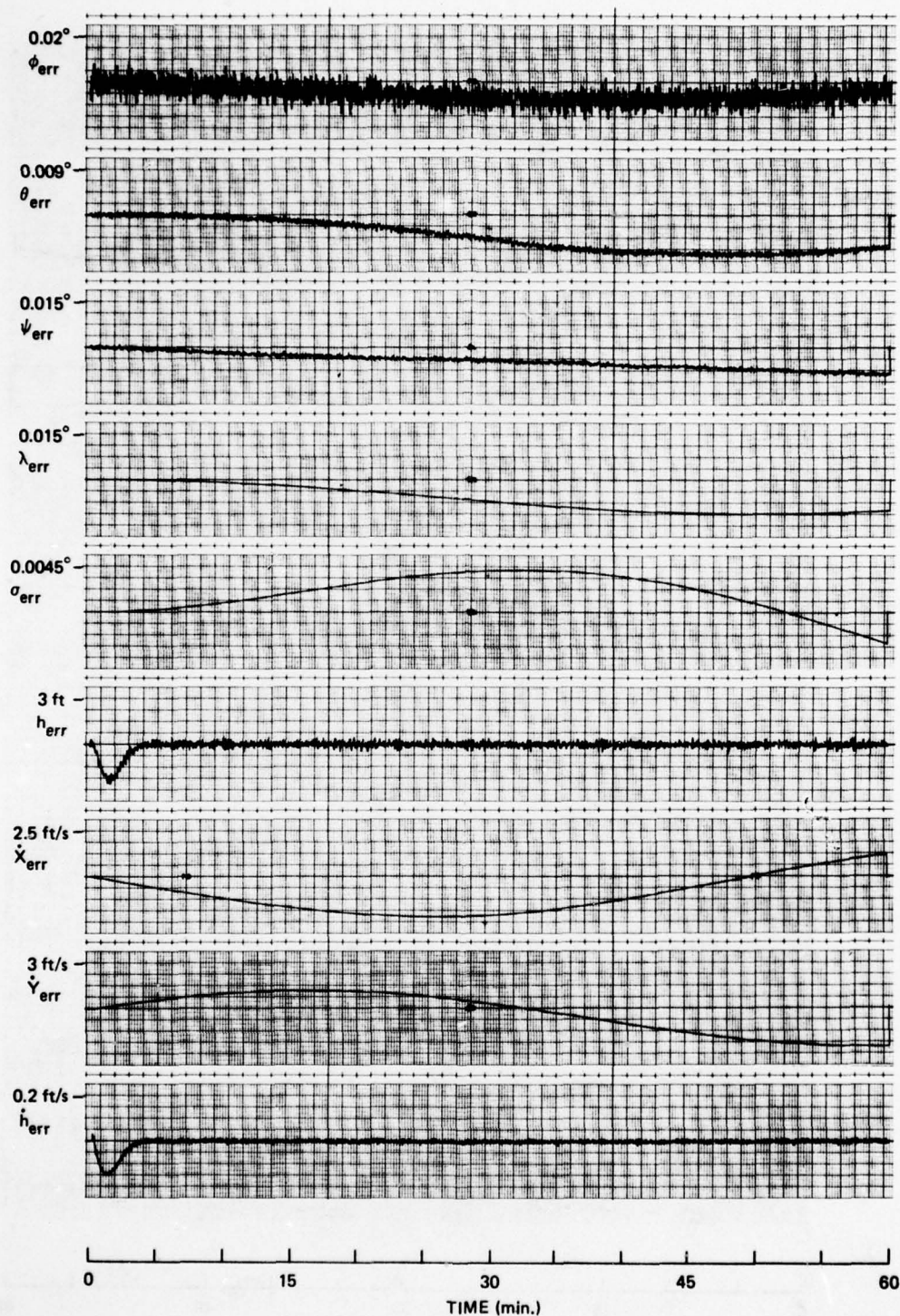
57

Figure 3-12. MIRA simulation responses: dodecahedron configuration at FS313; laser gyros; 1-hour run in turbulent environment (sheet 2 of 2).

58

Figure 3-13. MIRA simulation responses: octahedron configuration at FS313; two-degree-of-freedom gyros; 1-hour run in turbulent environment (sheet 1 of 2).
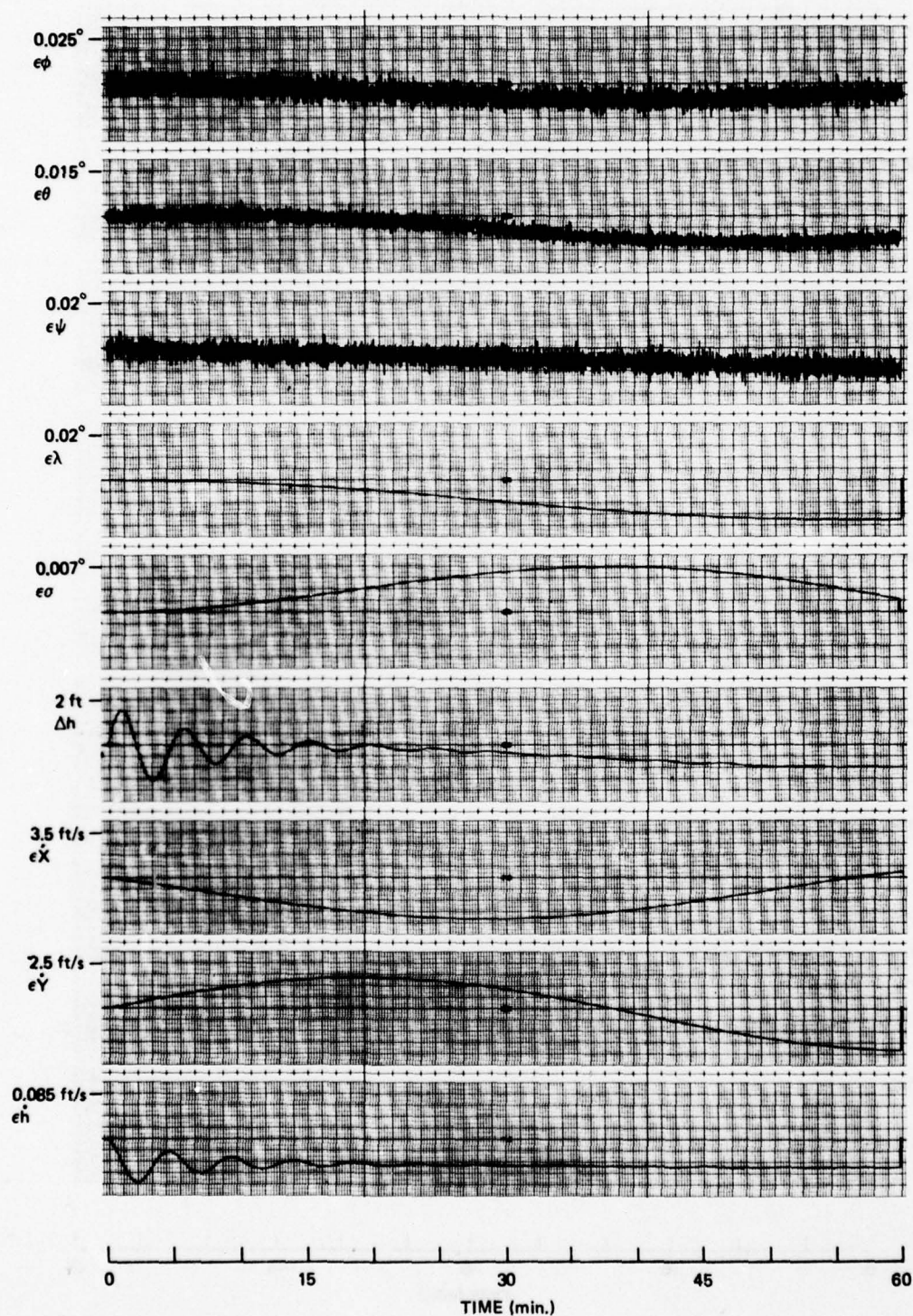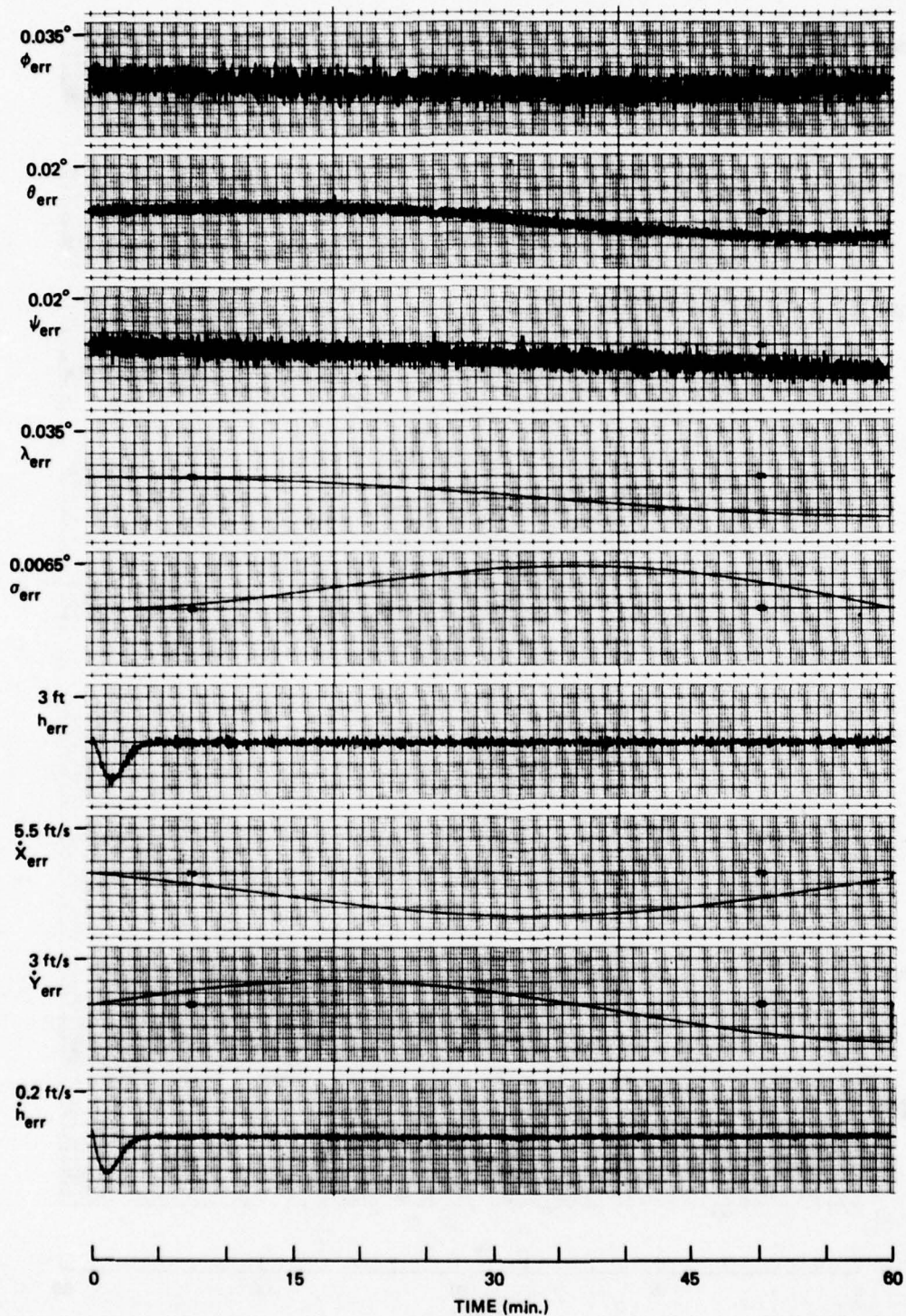
Figure 3-13. MIRA simulation responses: octahedron configuration at FS313; two-degree-of-freedom gyros; 1-hour run in turbulent environment (sheet 2 of 2).

A comparison of the responses in these two figures leads to the conclusion that the error-navigation outputs obtained are almost exact duplicates of each other. That is, the navigation errors due to the sensor errors are the same in both environments. The maximum error in latitude and longitude due to the sensor errors is about 0.4 nautical mile. The errors obtained by differencing the navigation-system and vehicle responses are the same as the responses of the error-navigation algorithm outputs for the benign-environment case. This verifies the operation and development of the navigation-system algorithm. The responses obtained for the turbulent environment are slightly noisier, as would be expected. The effect of the turbulence and structural modes on the navigation accuracy can be determined by comparing the navigation-system errors and error-navigation responses of Figure 3-8. First of all, the navigation-system Euler angle errors tend to be quite a bit noisier due to the high frequencies present in the vehicle Euler angles. Perhaps the most dramatic difference between the two sets of error variables is in the latitude response. This variable is biased negatively for the navigation-system error rather than oscillating about zero, as in the case of the error-navigation-algorithm output. A maximum latitude error of 0.7 nautical mile results. A bias is present in the north ground-velocity navigation-system error as well.

Using Figures 3-9 and 3-6, a similar comparison may be made for an orthogonal-triad-sensor configuration comprised of two-degree-of-freedom gyros. The responses of Figure 3-9 are for the benign environment, while the responses of Figure 3-6 have already been discussed. In the nonturbulent environment, the navigation-system errors and the error-algorithm outputs match extremely well. The sensors introduce latitude errors on the order of 0.9 nautical mile, while the longitude error is one-half of that. The errors obtained with the two-degree-of-freedom-gyro system appear to be slightly larger than those obtained with the laser-gyro triad presented in Figure 3-7. More specifically, most of the differences appear to be due to different drift rates associated with the sensor models that result in the laser and two-degree-of-freedom triad responses being skewed with respect to each other.

A comparison of the responses obtained with the two-degree-of-freedom-gyro triads in the calm and turbulent environment leads to the conclusion that the error-navigation-algorithm outputs are basically the

same in each case. The error-navigation outputs in the turbulent environment tend to be noisier, particularly the Euler-angle errors, but the mean signal tend to be the same. The navigation system errors in the turbulent environment are noisier yet due to the high frequencies present in the vehicle variables. Some of the navigation-system errors are also larger, such as latitude and north ground velocity.

A comparison of the responses in the turbulent environment for the laser-gyro and two-degree-of-freedom-gyro triad configurations (Figures 3-8 and 3-6) reveals that the two-degree-of-freedom-gyro model introduces much more noise into the output signal, particularly the Euler-angle-error signals. In addition, the latitude error is on the order of three times larger with the two-degree-of-freedom-gyro sensors. It is on the order of 2.5 nautical miles for the configuration chosen.

The lever-arm effects on navigation performance may be assessed by comparing Figures 3-10 and 3-11 with the figures just discussed. Figure 3-10 shows the error responses obtained at FS77 with the laser-gyro orthogonal triad, while Figure 3-11 shows the corresponding responses for the orthogonal triad with two-degree-of-freedom gyros. As for the sensor-error-induced navigation errors, they tend to be the same without respect to sensor location for the trajectory flown. This is true for both the two-degree-of-freedom- and laser-gyro configurations. As far as the navigation system is concerned, it tends to introduce noise into the system as evidenced by the noisier error-navigation-algorithm responses. This is particularly true of the ground-velocity-error signals. In addition, the latitude error is larger as a result of the navigation algorithm, and a bias is introduced into the north-ground-velocity error.

The last two sets of navigation-error responses obtained were those for the dodecahedron and octahedron sensor configurations located at FS313. Figures 3-12 and 3-13 show these results. A comparison of the dodecahedron-configuration responses with the orthogonal laser-triad responses reveals that the error responses for the dodecahedron are essentially scaled-down versions of their laser-triad counterparts. This is as it should be since the error coefficients of the sensor models for the dodecahedron configurations were scaled down by the square root of the error covariance gain. The only noticeably different response is the error-navigation-algorithm attitude error, which

has a different sign for the two cases of interest. The same conclusions are reached when the results for the octahedron configuration are compared to the laser-triad results. A direct comparison of the results obtained for the dodecahedron and octahedron configurations reveals that the dodecahedron responses are cleaner and smaller than those of the octahedron.

A further comparison of the navigation performance of the various sensor configurations considered is provided in Tables 3-7, 3-8, and 3-9. These tables contain the maximum magnitude, mean, and standard deviation of the error signals obtained for the 1-hour simulation runs. A consideration of the maximum magnitudes of the various error signals leads to the following conclusions:

(1) The values of the error-navigation-algorithm maximums are independent of environment and position for the laser-triad configuration.

(2) The maximum values of the error-navigation outputs for the two-degree-of-freedom-gyro triad tend to be the same for both FS313 and FS77. However, these quantities tend to be larger than those obtained in the benign environment.

(3) The maximum values of the navigation-system- and error-algorithm outputs are the same in the calm environment.

(4) The smallest maximum errors are obtained for the dodecahedron configuration. The laser orthogonal triad appears to follow, being slightly better than the octahedron configuration.

(5) The octahedron configuration produces smaller maximum errors than the triad with two-degree-of-freedom gyros.

(6) On the average, in a turbulent environment the maximum magnitudes of the navigation-system errors tend to be about 50-percent larger than their error-navigation-algorithm counterparts.

The results available from Table 3-8 (the listing of the mean navigation errors) tend to be less conclusive and fewer in number than those obtained by considering the magnitude of the maximum errors. However, some of the same conclusions are evident. For example,

(1) The mean errors obtained with the laser-triad configuration appear to be independent of position and environment.

Table 3-7. The maximum magnitude of the navigation-error signals for the 1-hour simulation runs.

Parameter	Units	Laser-Gyro Triad FS313	Laser-Gyro Triad FS77	Two-Degree-of-Freedom-Gyro Triad FS313	Two-Degree-of-Freedom-Gyro Triad FS77	Dodecahedron FS313	Octahedron FS313	Laser-Gyro Triad (no gusts) FS313	Two-Degree-of-Freedom-Gyro Triad (no gusts) FS313
ϕ_{err}	deg	0.0217	0.0231	0.0344	0.03506	0.0184	0.0320	0.0117	0.0114
θ_{err}	deg	0.0116	0.0136	0.0180	0.0204	0.0088	0.0157	0.0114	0.0111
ψ_{err}	deg	0.0127	0.0166	0.02198	0.02427	0.0100	0.0193	0.0079	0.0135
λ_{err}	deg	0.0114	0.0232	0.0365	0.04788	0.01128	0.0316	0.0074	0.0149
σ_{err}	deg	0.00603	0.00589	0.0078	0.0070	0.00418	0.00605	0.0057	0.00776
$\dot{h}_{err}$	ft/s	0.2129	0.5812	0.212	0.5816	0.1557	0.1700	0.2048	0.2048
$\dot{Y}_{err}$	ft/s	3.6506	4.596	3.248	4.259	2.5829	2.538	3.658	3.063
$\dot{X}_{err}$	ft/s	2.4754	4.230	6.073	7.8683	2.2199	5.208	4.023	3.0616
h_{err}	ft	3.604	4.026	3.589	4.0326	2.6697	2.890	3.194	3.1938
$\epsilon\phi$	deg	0.0122	0.01227	0.0247	0.0251	0.00884	0.0224	0.0117	0.0114
$\epsilon\theta$	deg	0.0112	0.0112	0.0152	0.0145	0.00804	0.0127	0.0111	0.0111
$\epsilon\psi$	deg	0.0107	0.0108	0.0195	0.0195	0.00772	0.01686	0.00979	0.0135
$\epsilon\lambda$	deg	0.00668	0.00667	0.0229	0.0193	0.00472	0.01795	0.00648	0.0149
$\epsilon\sigma$	deg	0.00612	0.00614	0.00886	0.0083	0.00433	0.00693	0.00553	0.00776
$\epsilon\dot{h}$	ft/s	0.1305	0.1301	0.1296	0.1306	0.0764	0.08297	0.1297	0.2049
$\epsilon\dot{Y}$	ft/s	3.642	3.633	2.9365	3.043	2.576	2.297	3.6189	3.063
$\epsilon\dot{X}$	ft/s	3.647	3.647	4.0612	3.575	2.579	3.1804	3.747	3.06155
Δh	ft	5.645	5.617	5.555	5.657	2.2956	1.54875	5.599	3.194

Table 3-8. The mean of navigation-error signals for the 1-hour simulation runs.

Parameter	Units	Laser-Gyro Triad FS313	Laser-Gyro Triad FS77	Two-Degree-of-Freedom-Gyro Triad FS313	Two-Degree-of-Freedom-Gyro Triad FS77	Dodecahedron FS313	Octahedron FS313	Laser-Gyro Triad (no gusts) FS313	Two-Degree-of-Freedom-Gyro Triad (no gusts) FS313
ϕ_{err}	deg	-0.007397	-0.007411	-0.007136	-0.00722	-0.005214	-0.00557	-0.007447	-0.007117
θ_{err}	deg	-0.006203	-0.00551	-0.00480	-0.004293	-0.041507	-0.003618	-0.007046	-0.00604
ψ_{err}	deg	-0.005744	-0.006445	-0.007027	-0.007911	-0.004384	-0.005714	-0.004098	-0.006579
λ_{err}	deg	-0.006823	-0.01221	-0.01717	-0.02131	-0.006454	-0.01453	-0.001546	-0.00882
α_{err}	deg	0.002697	0.002517	0.004371	0.003655	0.001845	0.003372	0.002083	0.004385
$\dot{h}_{err}$	ft/s	-0.006793	-0.006963	-0.00686	-0.00707	-0.004817	-0.005369	-0.006699	-0.006718
$\dot{Y}_{err}$	ft/s	-0.4371	-0.4973	0.01054	-0.1924	-0.3198	0.001684	-0.5728	0.0594
$\dot{X}_{err}$	ft/s	-0.8042	-2.3091	-3.70359	-4.853	-1.0349	-3.2063	0.7510	-1.2839
h_{err}	ft	-0.1129	-0.1158	-0.1140	-0.11758	-0.07994	-0.08915	-0.1117	-0.1120
$\epsilon\phi$	deg	-0.00744	-0.00744	-0.007036	-0.007097	-0.005264	-0.005503	-0.00743	-0.007051
$\epsilon\theta$	deg	-0.00685	-0.00685	-0.005379	-0.005591	-0.004844	-0.004226	-0.00690	-0.005819
$\epsilon\psi$	deg	-0.00502	-0.00506	-0.006059	-0.006539	-0.00355	-0.00474	-0.004705	-0.006369
$\epsilon\lambda$	deg	-0.001516	-0.00152	-0.01212	-0.01068	-0.001074	-0.009494	-0.001759	-0.009161
$\epsilon\alpha$	deg	0.002731	-0.002757	0.005198	0.004768	0.00193	0.004066	0.002217	0.004581
$\epsilon\dot{h}$	ft/s	-0.06344	-0.06333	-0.06371	-0.06399	-0.04415	-0.04925	-0.0634	-0.06356
$\epsilon\dot{Y}$	ft/s	-0.4427	-0.4345	0.24097	0.1255	-0.3130	0.18843	-0.5384	0.1223
$\epsilon\dot{X}$	ft/s	0.6767	0.6760	-2.3048	-1.8986	0.4785	-1.8026	0.6572	-1.4309
Δh	ft	-3.1429	-3.1221	-3.1948	-3.2499	0.5358	-0.43668	-3.1468	-3.170

Table 3-9. The standard deviation of the navigation-error signals for the 1-hour simulation runs.

Parameter	Units	Laser-Gyro Triad FS313	Laser-Gyro Triad FS77	Two-Degree-of-Freedom-Gyro Triad FS313	Two-Degree-of-Freedom-Gyro Triad FS77	Dodecahedron FS313	Octahedron FS313	Laser-Gyro Triad (no gusts) FS313	Two-Degree-of-Freedom-Gyro Triad (no gusts) FS313
ϕ_{err}	deg	0.00456	0.004660	0.006786	0.006473	0.003799	0.00638	0.00344	0.003542
θ_{err}	deg	0.00375	0.005037	0.00633	0.007695	0.002967	0.00535	0.003506	0.004224
ψ_{err}	deg	0.00320	0.003964	0.004936	0.005581	0.002472	0.004279	0.00205	0.003667
λ_{err}	deg	0.00403	0.008605	0.01299	0.01679	0.004184	0.01117	0.003144	0.005476
σ_{err}	deg	0.00269	0.00277	0.002673	0.002598	0.001902	0.002070	0.00281	0.00262
$\dot{h}_{err}$	ft/s	0.03067	0.1505	0.03053	0.1505	0.02209	0.02414	0.0299	0.02991
$\dot{Y}_{err}$	ft/s	1.9109	1.9649	1.7935	1.8805	1.3449	1.3943	1.9095	1.7141
$\dot{X}_{err}$	ft/s	1.4792	1.5379	1.8787	2.4104	0.9995	1.5946	2.032	1.5211
h_{err}	ft	0.5094	0.5650	0.50713	0.5656	0.3794	0.4099	0.4799	0.4799
$\varepsilon\phi$	deg	0.00361	0.003607	0.005109	0.00492	0.002559	0.004550	0.003455	0.003533
$\varepsilon\theta$	deg	0.00327	0.00327	0.004836	0.004537	0.00232	0.003896	0.003401	0.004071
$\varepsilon\psi$	deg	0.00292	0.00293	0.00433	0.004489	0.002071	0.003748	0.002591	0.003502
$\varepsilon\lambda$	deg	0.00289	0.002887	0.00842	0.007160	0.002043	0.006591	0.002926	0.005782
$\varepsilon\sigma$	deg	0.00273	0.00272	0.002946	0.002777	0.001932	0.002305	0.0276	0.002668
$\varepsilon\dot{h}$	ft/s	0.0141	0.01405	0.01397	0.0141	0.00834	0.008289	0.01394	0.01394
$\varepsilon\dot{Y}$	ft/s	1.935	1.931	1.724	1.7496	1.3687	1.3488	1.9005	1.679
$\varepsilon\dot{X}$	ft/s	1.8676	1.8679	1.4089	1.3656	1.3211	1.1049	1.9312	1.4047
Δh	ft	0.7944	0.7913	0.8136	0.81727	0.4326	0.4953	0.7817	0.7869

(2) The smallest mean errors result with the dodecahedron configuration. However, the next best configuration is not clear.

(3) The navigation-system errors and the error-navigation-algorithm outputs have the same mean value in the nonturbulent environment.

(4) The mean errors obtained with the octahedron configuration are smaller than those obtained with the two-degree-of-freedom-triad configuration.

(5) In the calm environment, the mean values of the laser-triad-error variables are smaller than those of the triad comprised of two-degree-of-freedom gyros.

(6) The mean errors obtained with the two-degree-of-freedom-gyro triad are a function of position and environment.

(7) The largest mean errors are obtained with the sensors located at FS313 in a turbulent environment, while the smallest errors are obtained at FS313 without the turbulence.

Table 3-9 (the standard deviations of the error variables) provides many conclusions concerning the relative merits of the navigation performance of the sensor configurations evaluated. The following conclusions may be drawn from the table:

(1) The standard deviations of the error variables associated with the laser configurations are less than the corresponding entries for the two-degree-of-freedom gyros.

(2) The quantities obtained with the error-navigation algorithm for the laser-gyro configuration do not appear to be affected greatly by position and environment. However, when the standard deviations of the navigation output errors are considered, this does not appear to be true to the same extent.

(3) The error-algorithm outputs obtained for the two-degree-of-freedom-triad configuration show a relatively large variation with position and environment.

(4) The dodecahedron configuration appears to produce the smallest standard deviations. The next best configuration, when all of the results are taken into consideration, is not clear.

67

(5) The octahedron configuration produced better results than the two-degree-of-freedom orthogonal triad.

The results of the short-duration simulation runs will now be considered. As mentioned previously, the commanded trajectory was selected to excite the transient modes of the system. This was done by having the vehicle undergo a 30-degree banked turn until a 30-degree change in heading was achieved. The wings were then leveled and a 5-degree change in flight-path angle commanded.

Figure 3-14 contains a complete set of time histories obtained for one of the short-duration runs. The flight-control and navigation sensors are all colocated at FS313. The autopilot causes the vehicle to follow the commanded trajectory reasonably well. The bank angle settles at 30 degrees after a slight initial overshoot, and the heading increases linearly until a 30-degree change is achieved. The speed is maintained within 3 feet per second of the trim value, and it deviates by about that much only when the change in flight-path angle is commanded. The flight-path angle achieves a peak of 8 degrees, and this is due to the coupling in the vehicle responses. The leveling of the vehicle's wings after the desired heading is achieved causes a transient in the flight-path angle. The 5-degree commanded change in flight-path angle comes when this transient is occurring. The turn is fairly well coordinated with a side acceleration of less than 0.1 g. A normal acceleration of 0.8 g results when the pull-up command is initiated. The flight-control-sensor signals are oscillatory, reflecting the vehicle modal responses in the turbulent environment. The vehicle-control deflections are reasonable with a 12.0-degree aileron pulse required to achieve the 30-degree bank angle, while the rudder deflection is essentially parabolic in shape, reflecting a command to maintain a constant yaw rate and zero sideslip angle. The longitudinal controls are excited primarily when the flight-path-angle command is initiated. More thrust is called for to maintain speed, while the horizontal tail deflection causes the vehicle to pitch up.

The time histories obtained for the calm environment, which correspond to those just discussed, have also been obtained. They are just smoothed versions of the responses of Figure 3-14 and are not presented for this reason.

The structural-mode responses are also included in Figure 3-14 to provide an indication of the magnitude and character of their
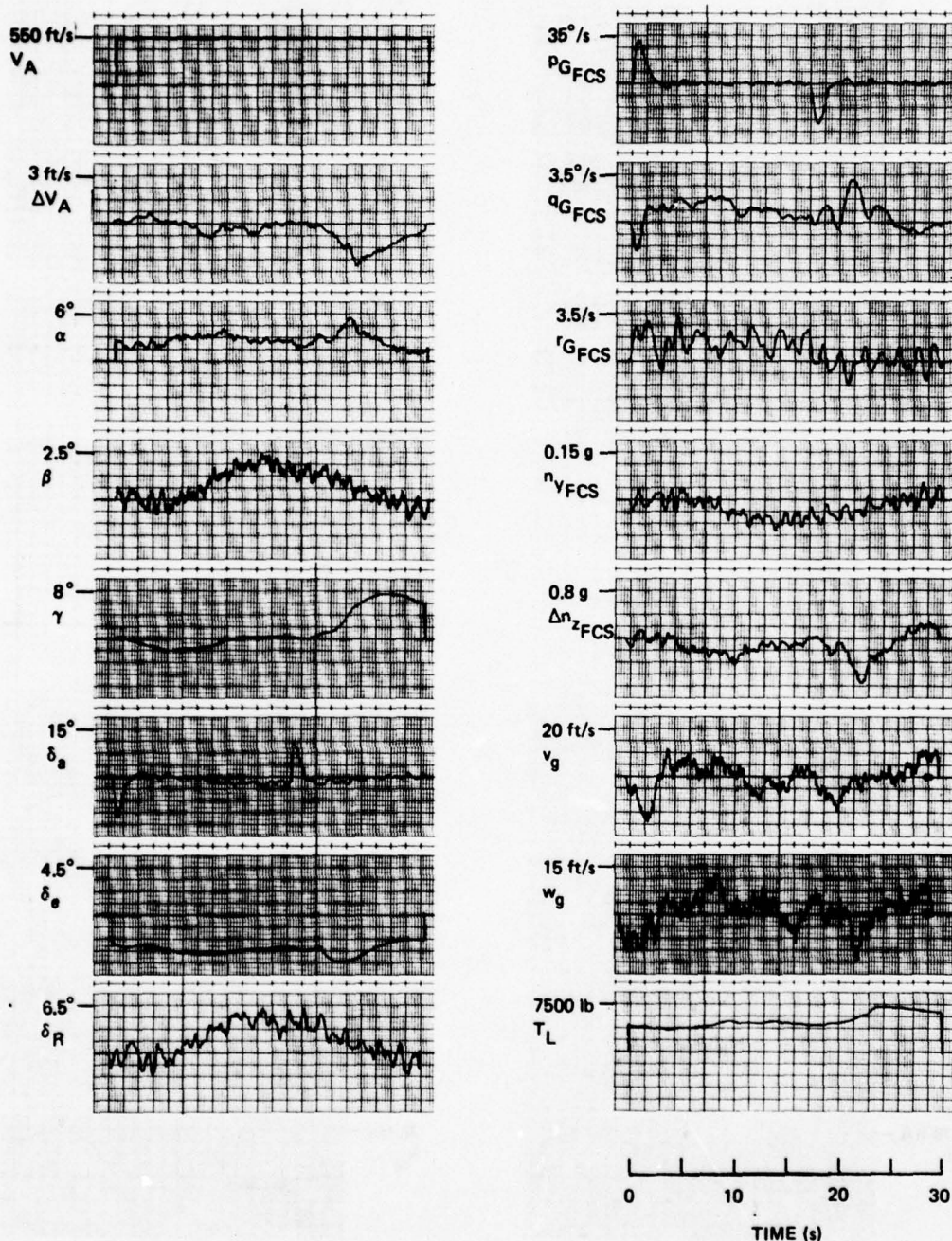
Figure 3-14.   MIRA simulation responses: all sensors located at FS313;
laser navigation gyros; 30-second run in turbulent
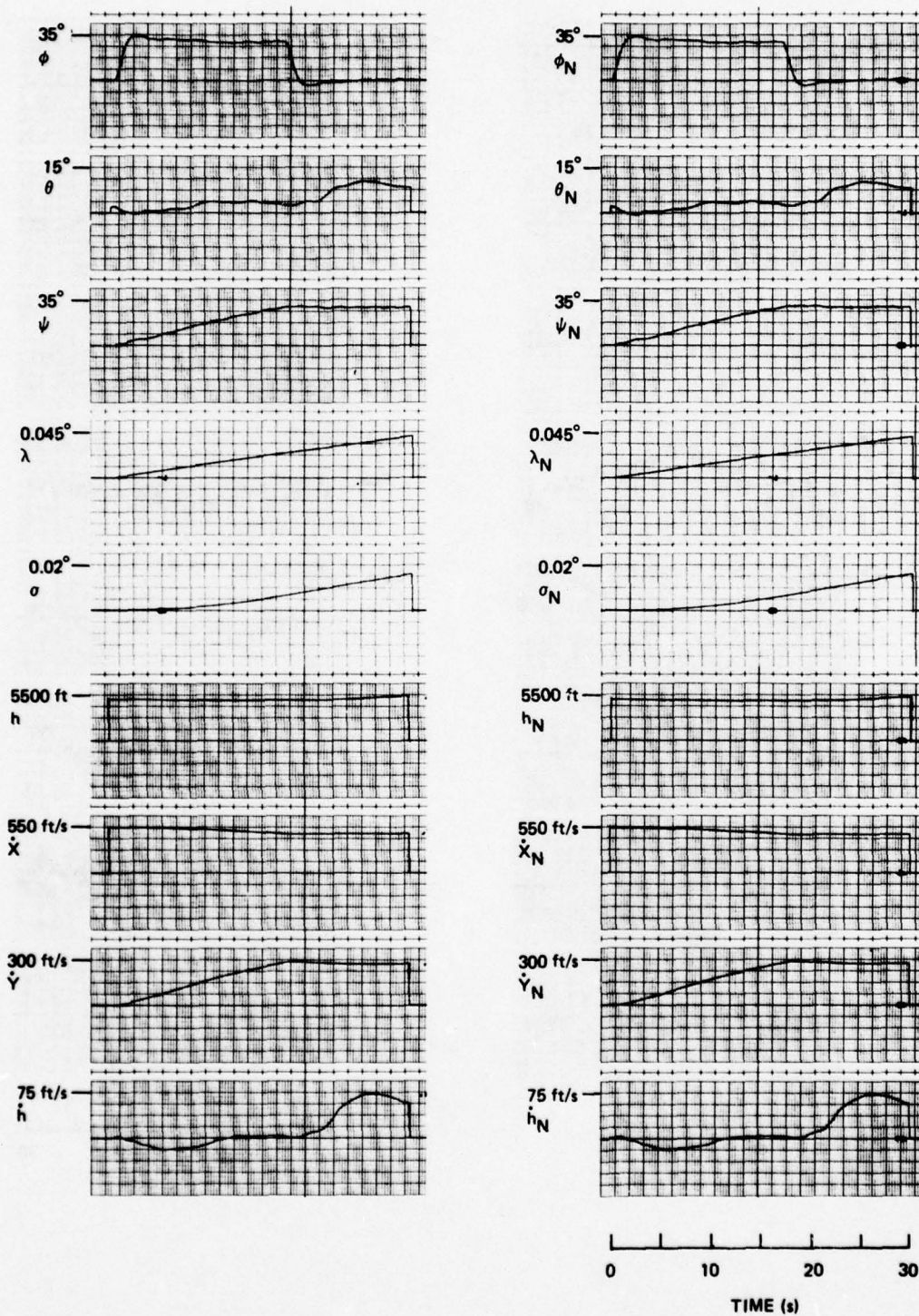environment (sheet 1 of 4).

Figure 3-14. MIRA simulation responses: all sensors located at FS313; laser navigation gyros; 30-second run in turbulent environment (sheet 2 of 4).
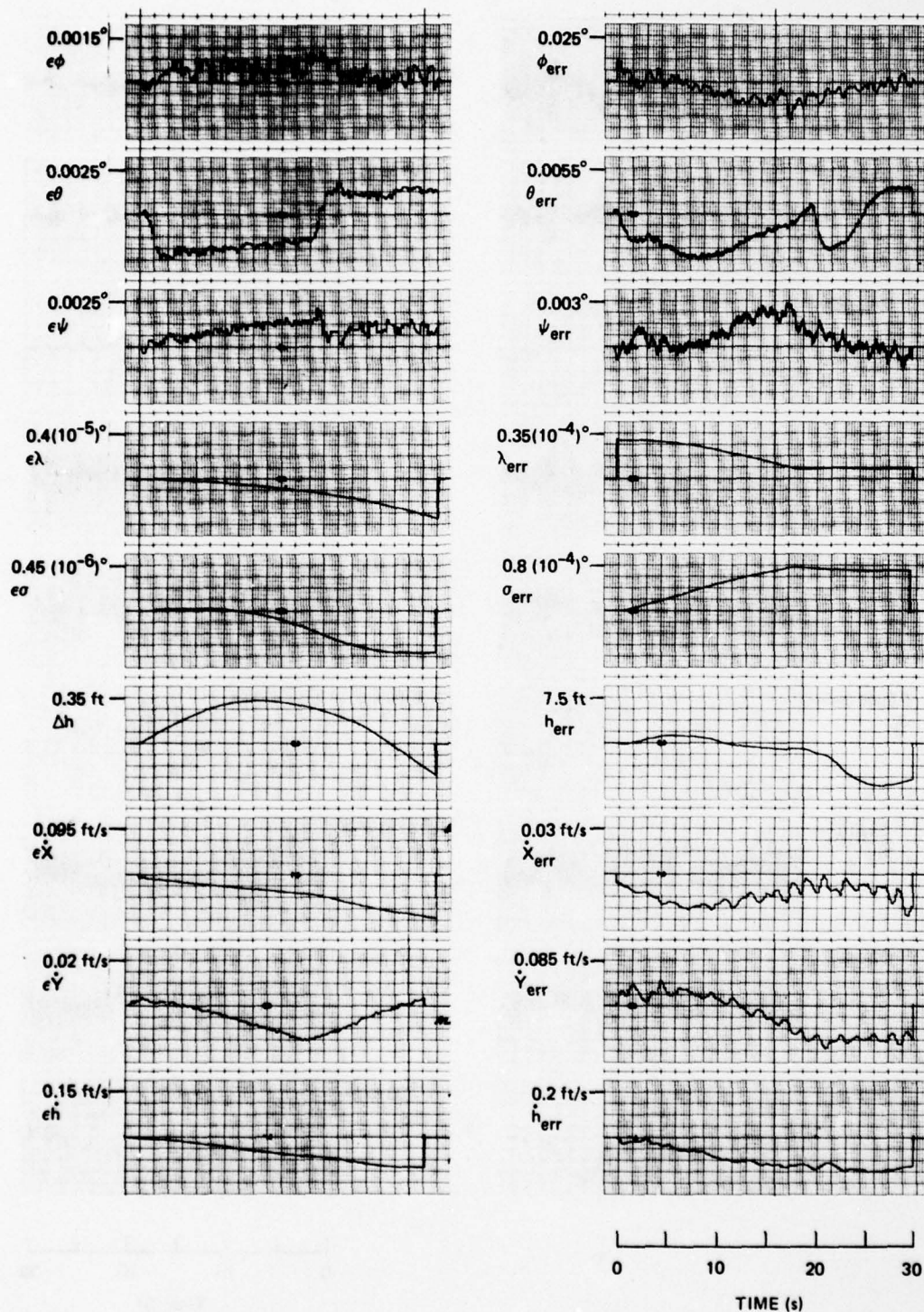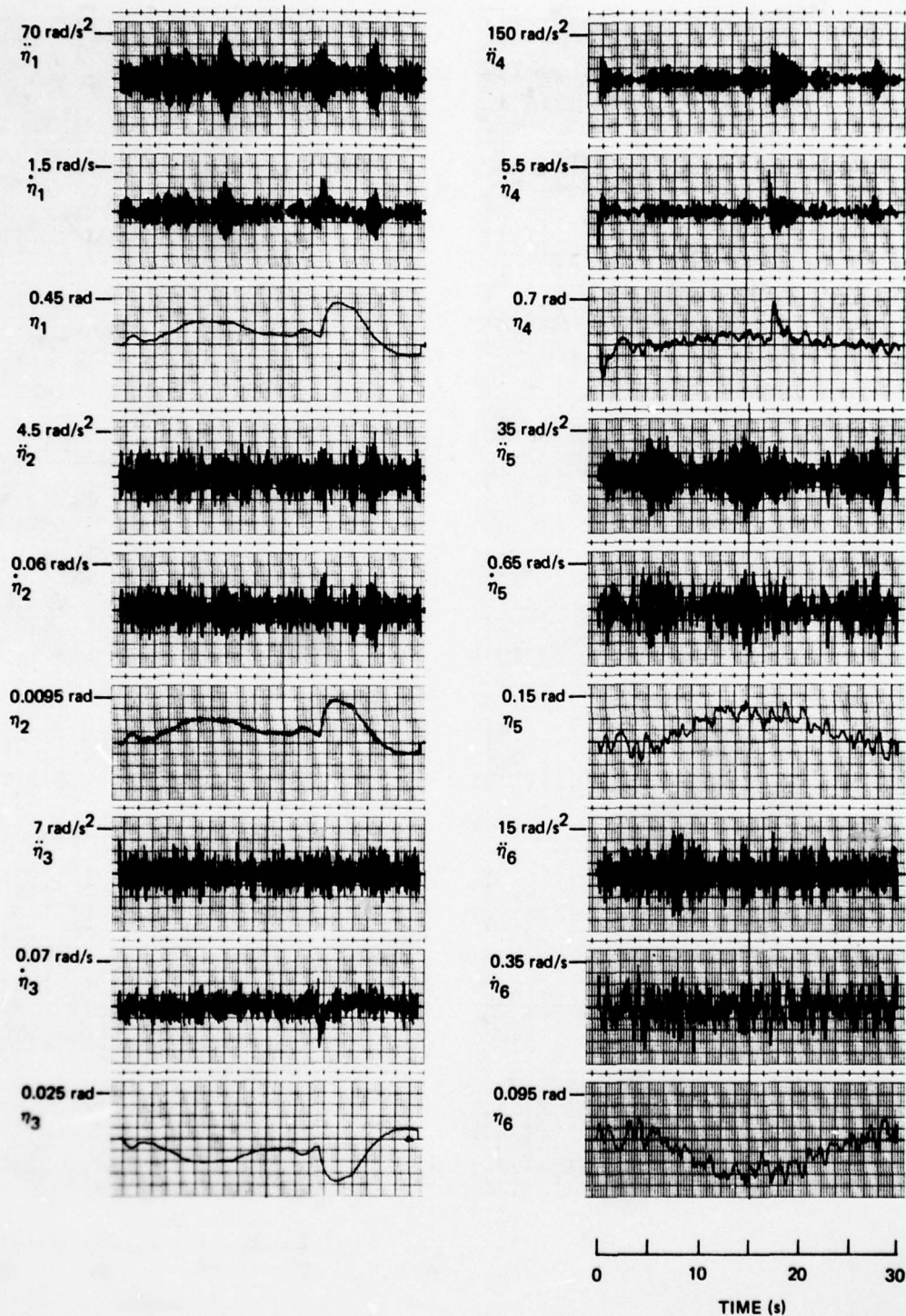
70

Figure 3-14. MIRA simulation responses: all sensors located at FS313; laser navigation gyros; 30-second run in turbulent environment (sheet 3 of 4).

Figure 3-14. MIRA simulation responses: all sensors located at FS313; laser navigation gyros; 30-second run in turbulent environment (sheet 4 of 4).

excitation. The mode excitation results in the following maximum effect on the sensors:

(1) 0.004 g on the normal accelerometer and 0.002 degree per second on the pitch-rate gyro, each due to the first longitudinal mode.

(2) $4.0(10^{-5})$ g on the lateral accelerometer and 0.007 degree per second on the yaw-rate-gyro signal, each due to the third lateral-directional mode.

(3) 0.1 degree per second on the roll-rate gyro, due to the first lateral-directional mode.

None of these effects is of major importance.

The last set of variables included in Figure 3-14 are the outputs of the navigation-system model and the error responses due to the differencing of the navigation system, and vehicle responses and the output of the error-navigation algorithm. First, the error-navigation outputs are almost identical to those obtained in the nonturbulent environment without structural modes. It is also evident that the environment and dynamic behavior of the vehicle cause large navigation-system errors relative to those caused by the sensor errors.

The MIRA simulation responses included in Figure 3-15 correspond to those of Figure 3-14 with the exception that the sensors are located at FS77 rather than near the cg of the vehicle. There are several differences evident from these two sets of responses. One of them is that the damping of the lateral-directional responses is greater when the sensors are located at FS77, resulting in less oscillatory responses. On the other hand, the longitudinal responses are about the same in this regard. The lateral-directional structural modes are also excited to a slightly greater degree when the sensors are located near the pilot's station. However, this change is not significant enought to cause a major effect on the sensors. A comparison of Figures 3-14 and 3-15 shows that the navigation errors due to the sensor errors are independent of sensor location. The navigation-system errors are larger when the sensors are located at FS77, reflecting the lever-arm effects present in this case.

The next two sets of time histories presented are the same as those just discussed with the exception that two-degree-of-freedom-gyro models were used instead of laser-gyro models. The responses in
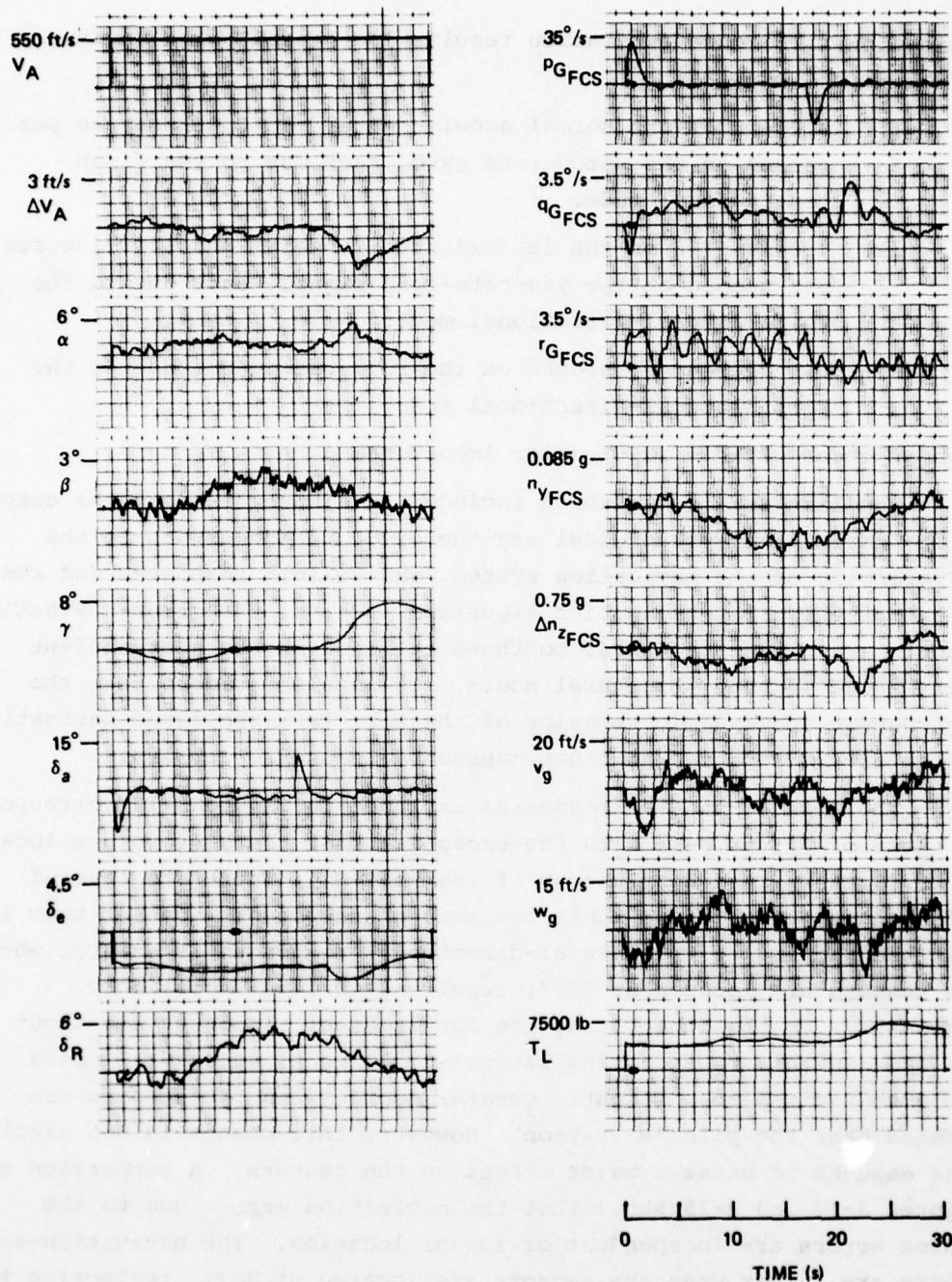
Figure 3-15. MIRA simulation responses: all sensors located at FS77;
laser navigation gyros; 30-second run in turbulent
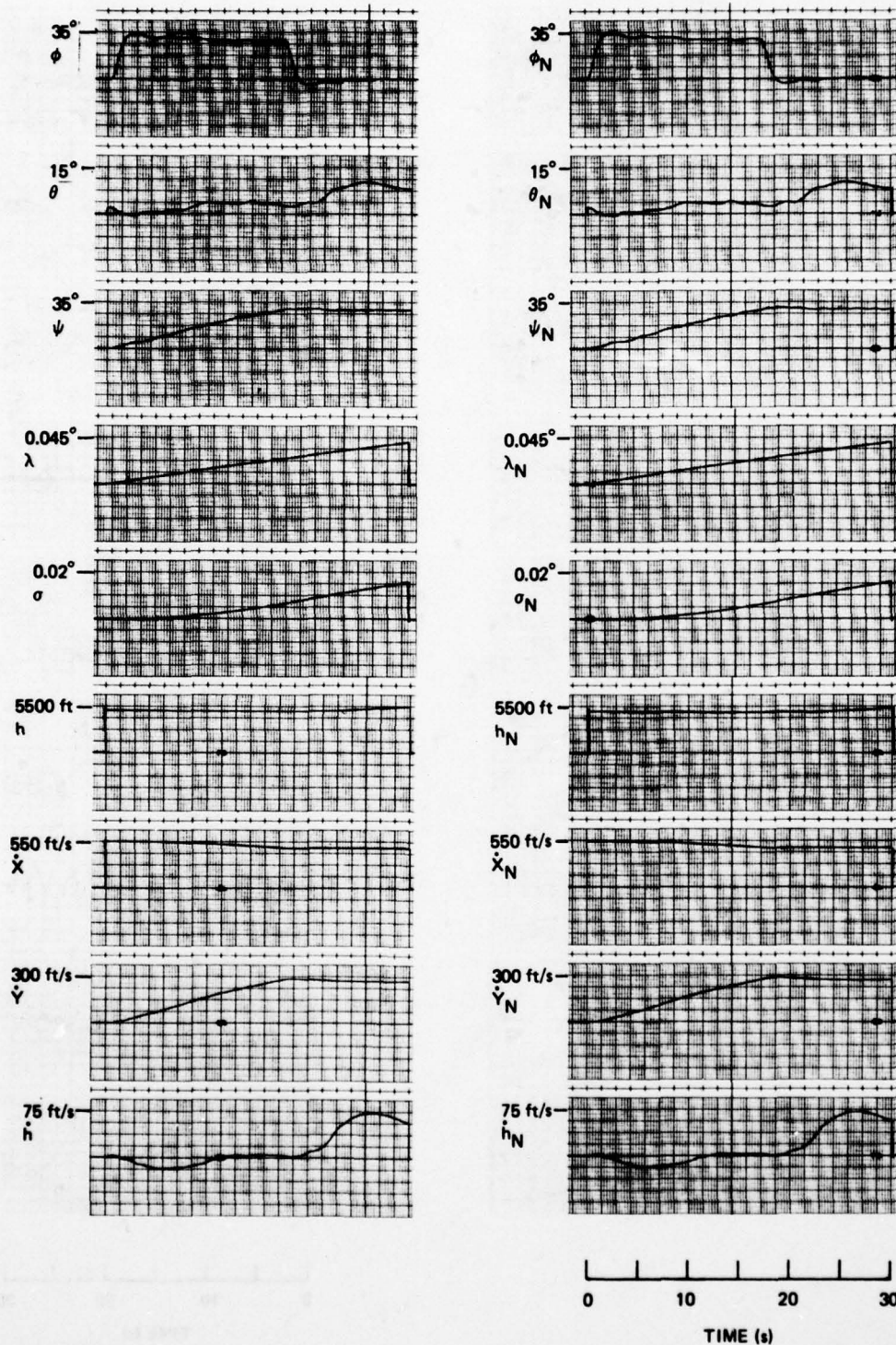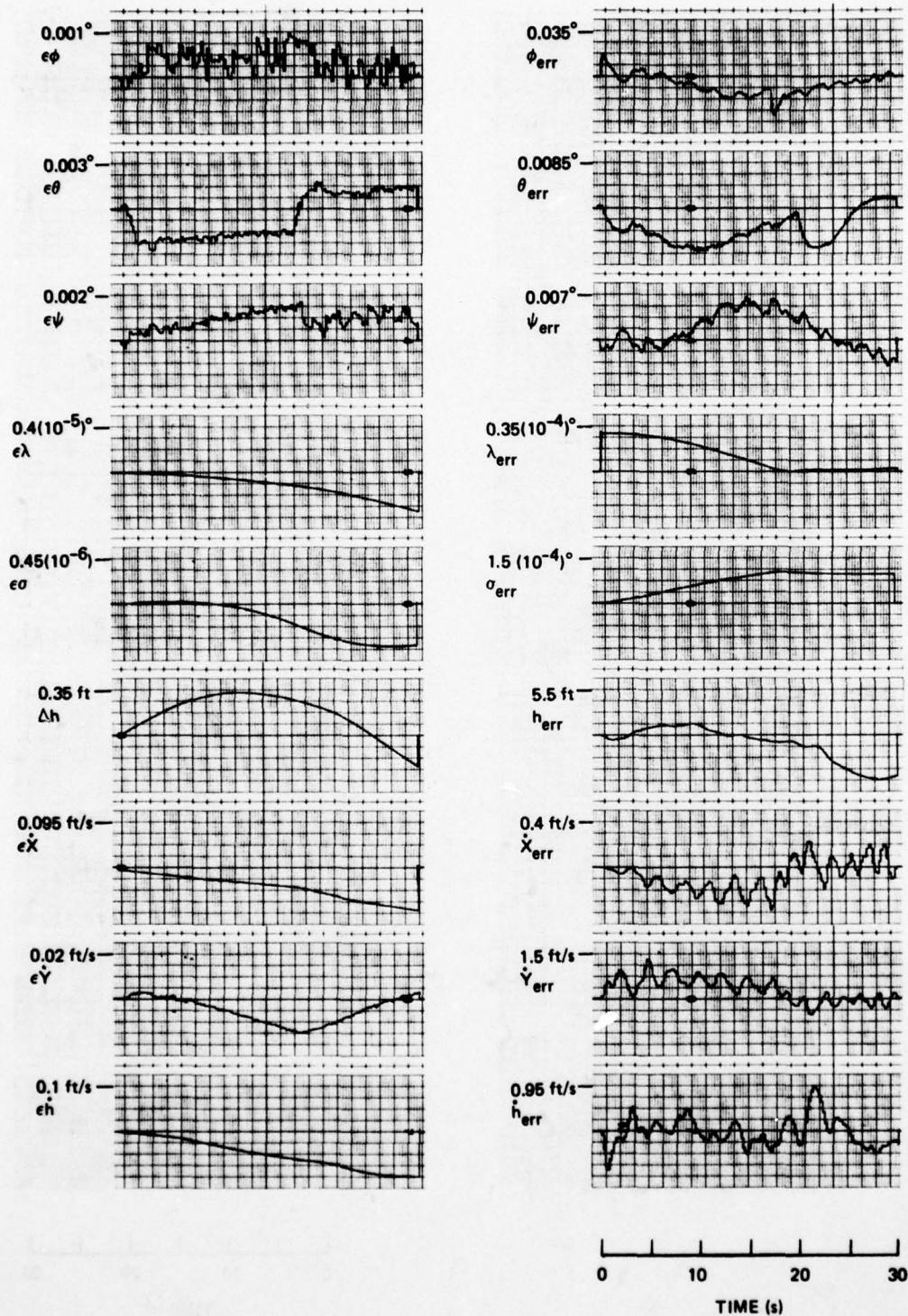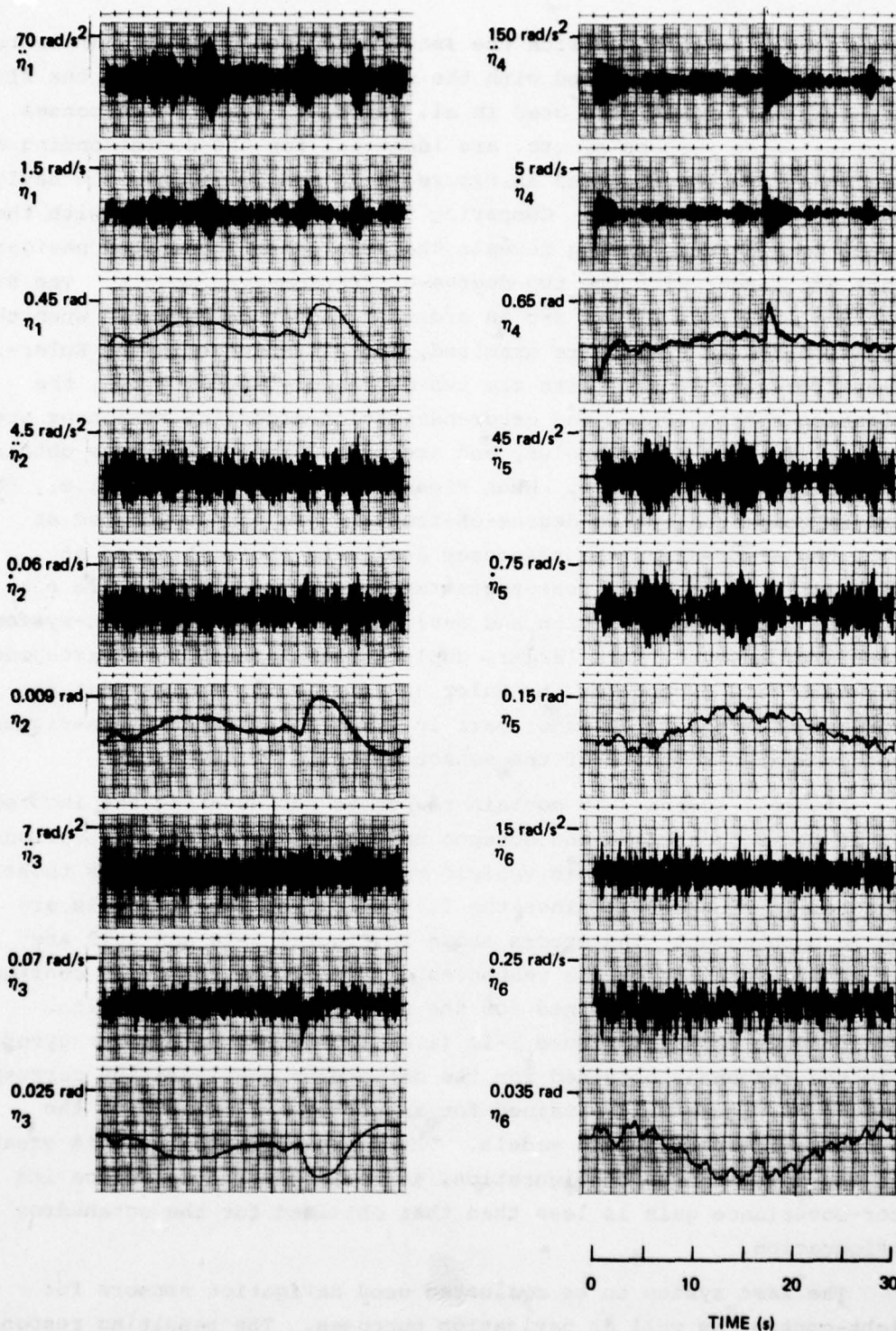environment (sheet 1 of 4).

74

Figure 3-15. MIRA simulation responses: all sensors located at FS77;
laser navigation gyros; 30-second run in turbulent
environment (sheet 2 of 4).

Figure 3-15. MIRA simulation responses: all sensors located at FS77; laser navigation gyros; 30-second run in turbulent environment (sheet 3 of 4).

Figure 3-15. MIRA simulation responses: all sensors located at FS77; laser navigation gyros; 30-second run in turbulent environment (sheet 4 of 4).

Figure 3-16 were obtained with the sensors located at FS313, while those of Figure 3-17 were obtained with the sensors at FS77. Since the flight-control-sensor models were used in all cases, the vehicle responses, structural-mode responses, etc. are identical for the corresponding cases. Hence, they are not repeated in Figures 3-16 and 3-17; only the navigation errors are presented. Comparing the responses obtained with the sensors located near the cg reveals that the sensor-generated navigator errors are larger with the two-degree-of-freedom-gyro models. The Euler-angle and longitude errors are an order of magnitude larger. When the navigation-system errors are examined, the differences in the Euler-angle errors stand out. With the two-degree-of-freedom gyros, the navigation-system errors and error-navigation-algorithm responses are identical for the Euler angles, and are much larger than those obtained with the laser-gyro models. When Figure 3-17 is considered (i.e., the triad is comprised of two-degree-of-freedom-gyro models located at FS77), the error-algorithm responses duplicate those obtained at FS313, implying that the sensor-generated navigation errors are not a strong function of position and environment. The navigation-system errors are, however, much larger, duplicating those of the corresponding laser-gyro case except for the Euler angles. This implies that the lever-arm effects play a major part in the generation of the navigation errors compared to those of the sensor errors.

Figure 3-18 and 3-19 contain responses representing the incorporation of the dodecahedron and octagon navigation-sensor configurations into the vehicle. The basic vehicle responses are the same as those presented in Figure 3-14 since the flight-control-sensor models are used in both cases. The errors shown in Figures 3-18 and 3-19 are just scaled versions of the responses obtained with the triad configuration. The responses obtained for the dodecahedron configuration correspond to those of Figure 3-14 (i.e., the triad with laser gyros), while the responses obtained for the octahedron configuration correspond to those of Figure 3-16 obtained for an orthogonal triad with the two-degree-of-freedom-gyro models. The relative improvement is greater with the dodecahedron configuration, as would be expected since its error-covariance gain is less than that obtained for the octahedron configuration.

The last system to be evaluated used navigation sensors for flight-control as well as navigation purposes. The resulting responses are presented in Figure 3-20. These responses, obtained for an
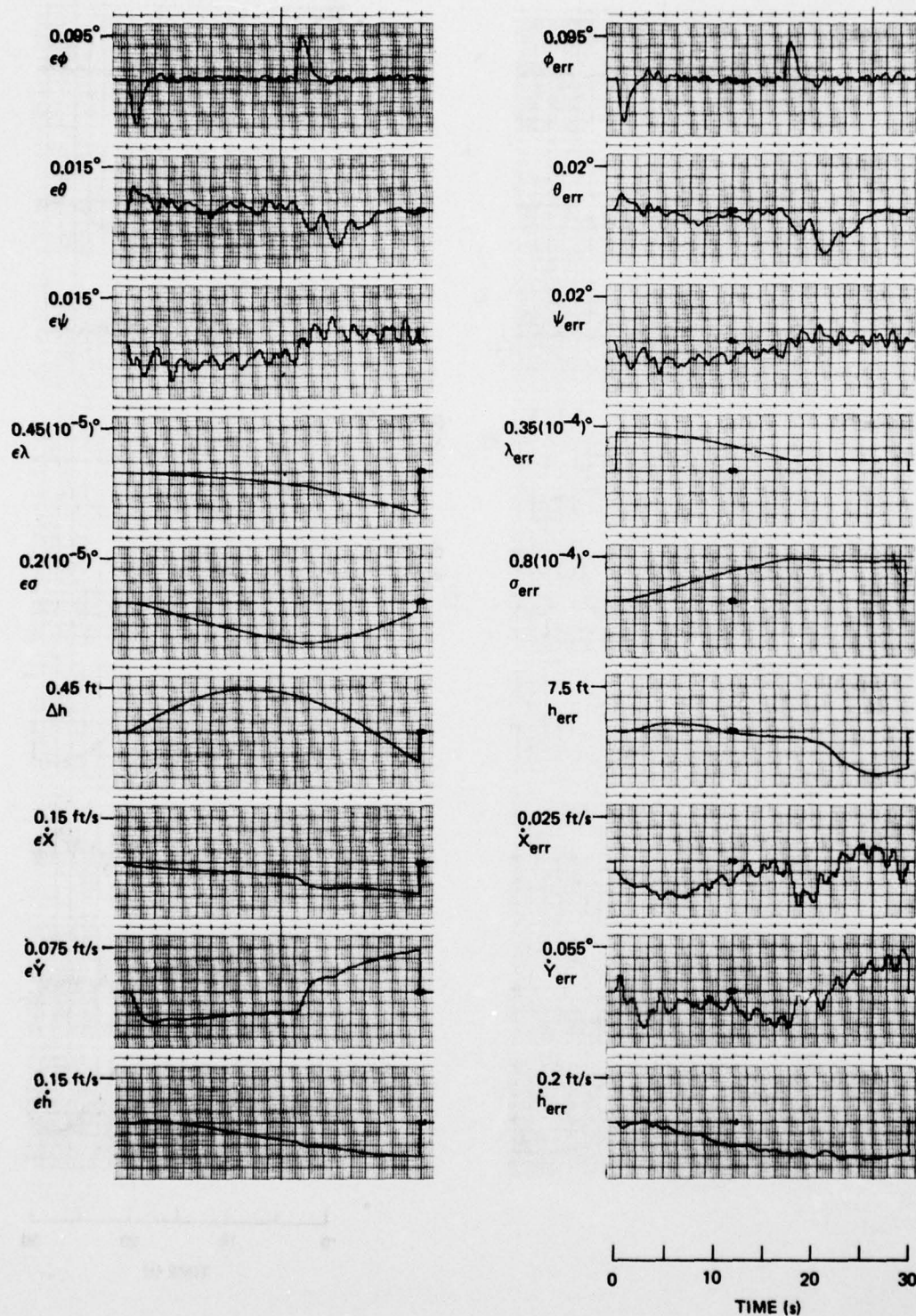
78

Figure 3-16. MIRA simulation responses: all sensors located at FS313; two-degree-of-freedom navigation gyros; 30-second run in turbulent environment.
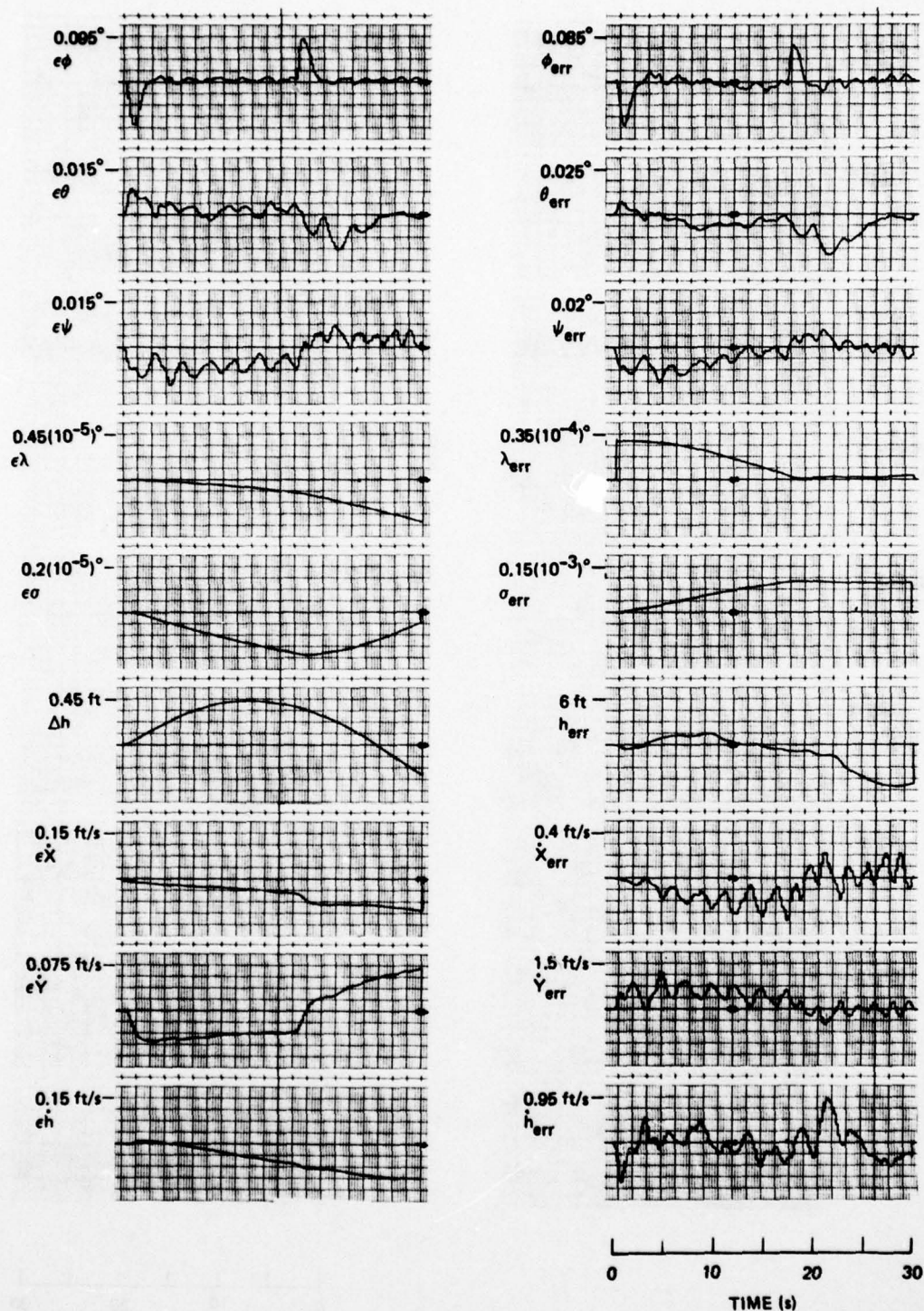
79

Figure 3-17. MIRA simulation responses: all sensors located at FS77; two-degree-of-freedom navigation gyros; 30-second run in turbulent environment.
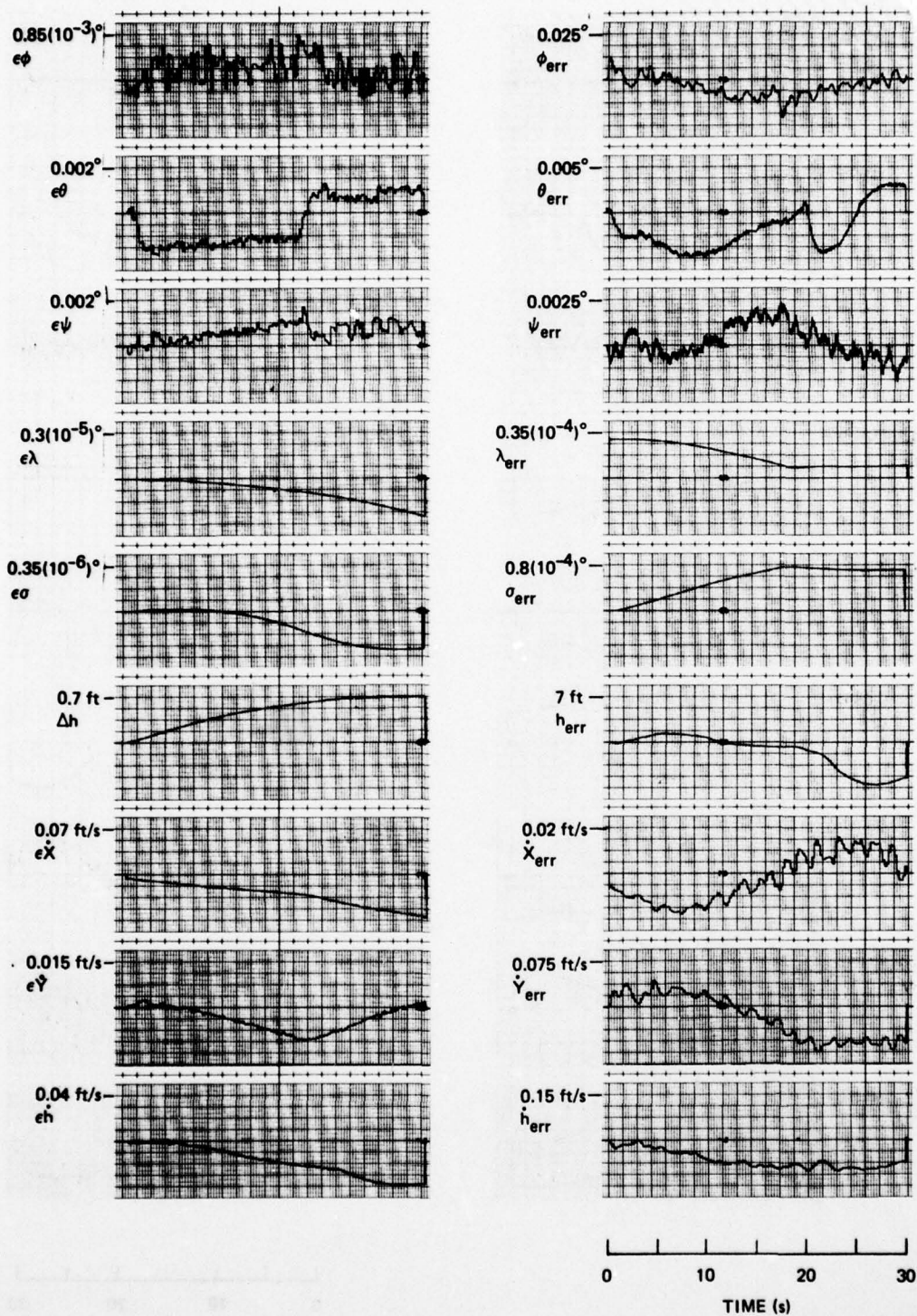
Figure 3-18. MIRA simulation responses: all sensors located at FS313;
dodecahedron navigation sensor configuration; 30-second
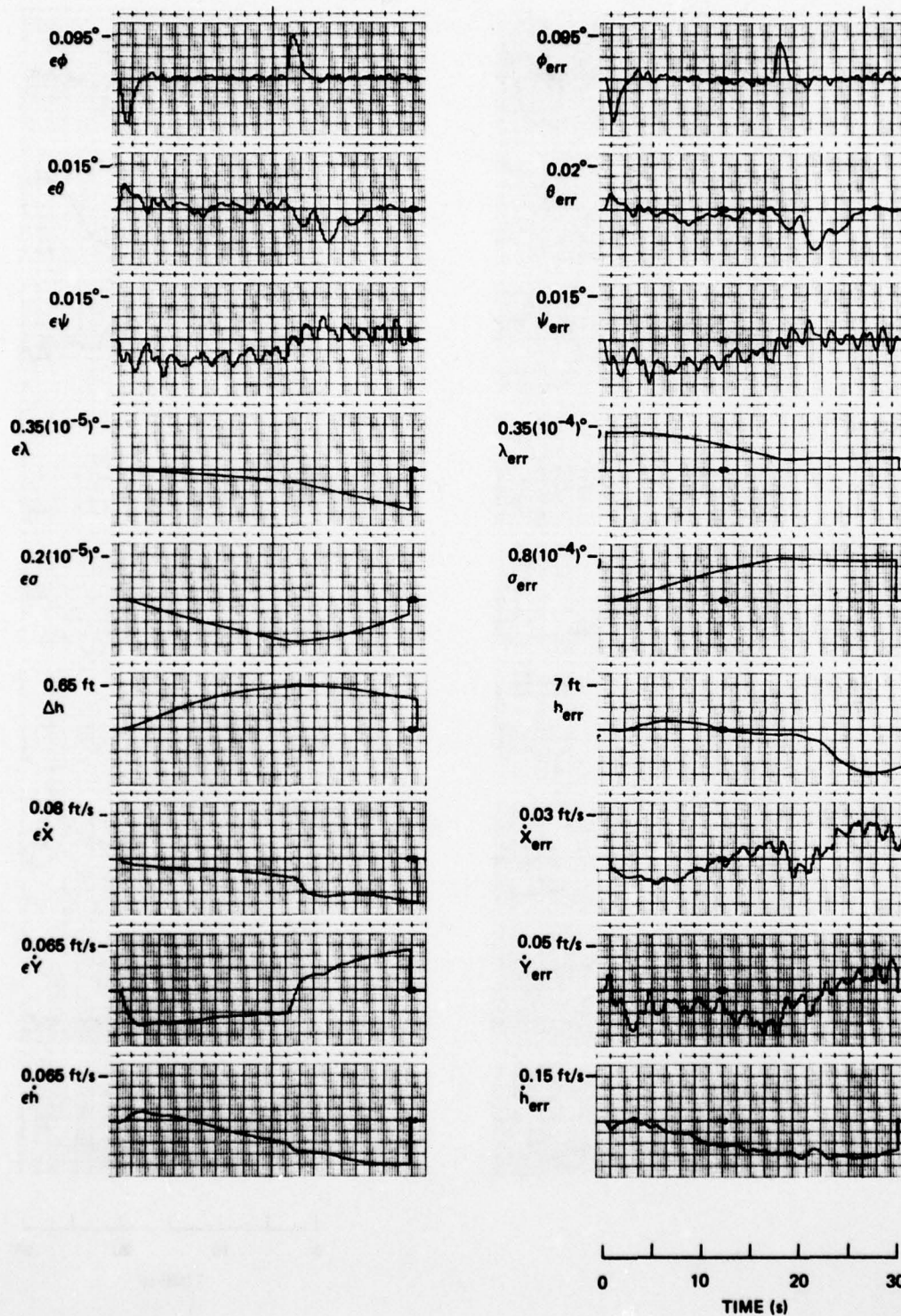run in turbulent environment.

81

Figure 3-19.   MIRA simulation responses: all sensors located at FS313;
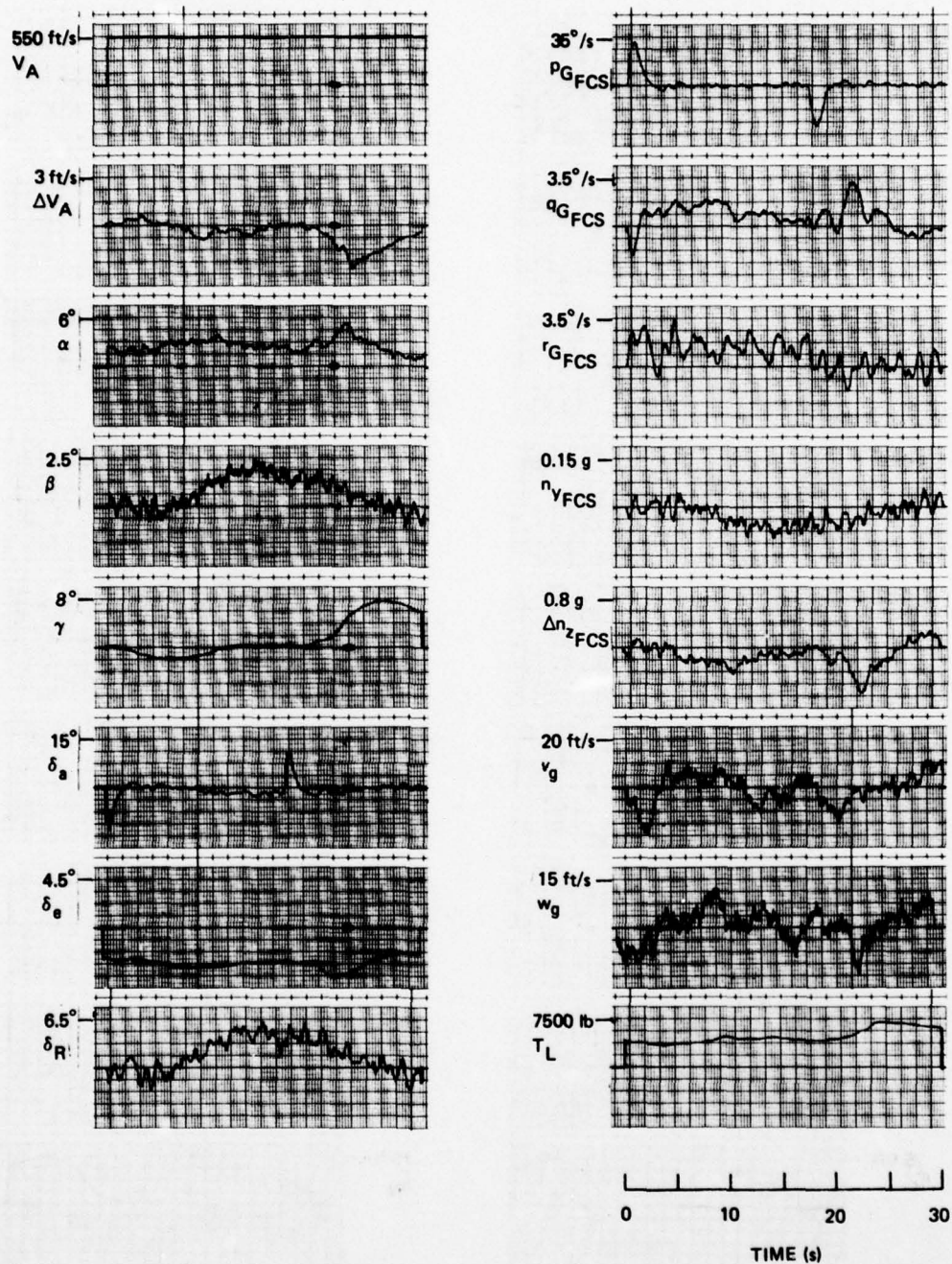octahedron navigation sensor configuration; 30-second run
in turbulent environment.

Figure 3-20. MIRA simulation responses: all sensors located at FS313; laser navigation gyros—navigation sensors used for flight control; 30-second run in turbulent environment (sheet 1 of 4).
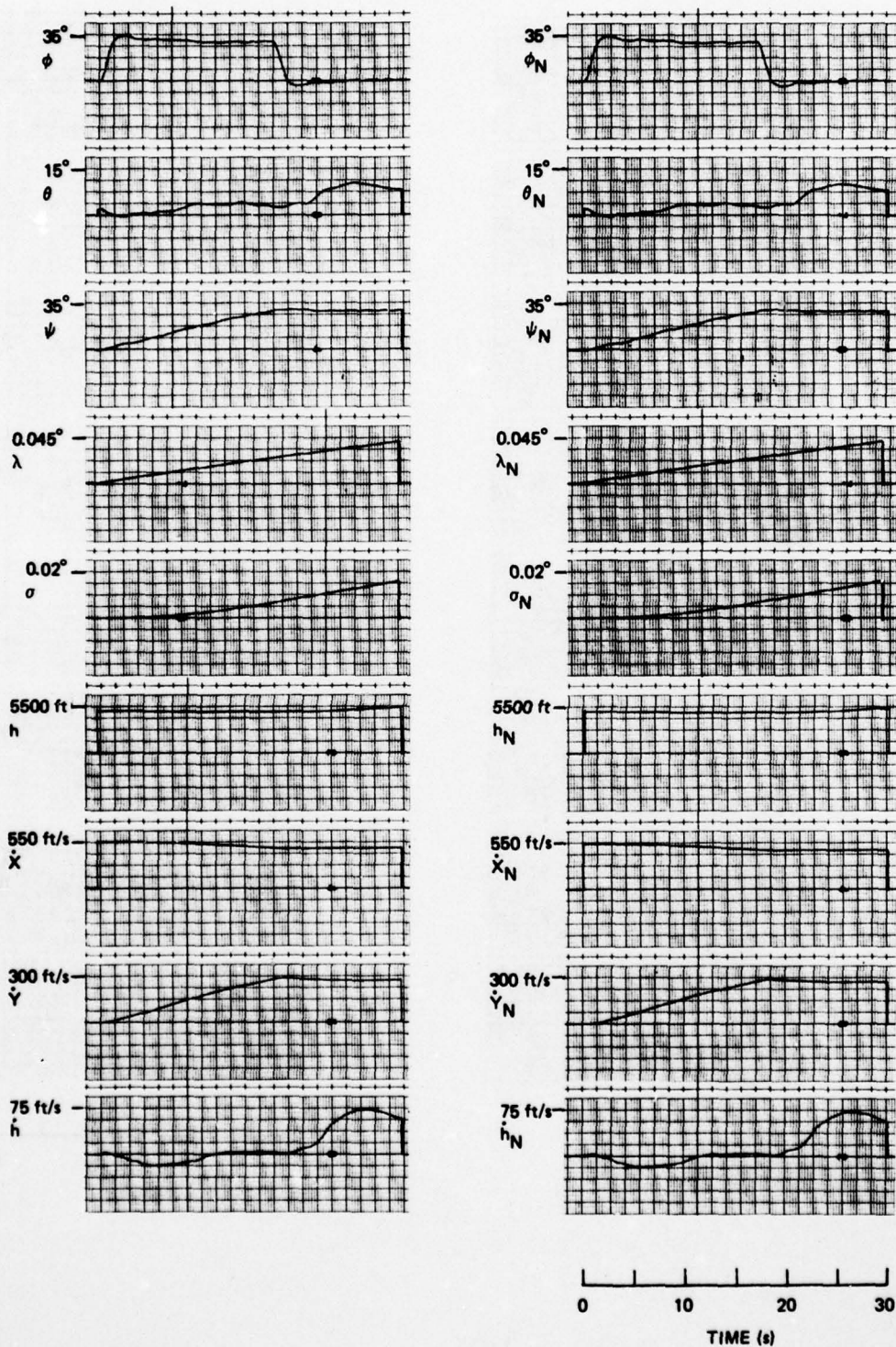
Figure 3-20. MIRA simulation responses: all sensors located at FS313; laser navigation gyros—navigation sensors used for flight control; 30-second run in turbulent environment (sheet 2 of 4).

Figure 3-20. MIRA simulation responses: all sensors located at FS313; laser navigation gyros—navigation sensors used for flignt control; 30-second run in turbulent environment (sheet 3 of 4).
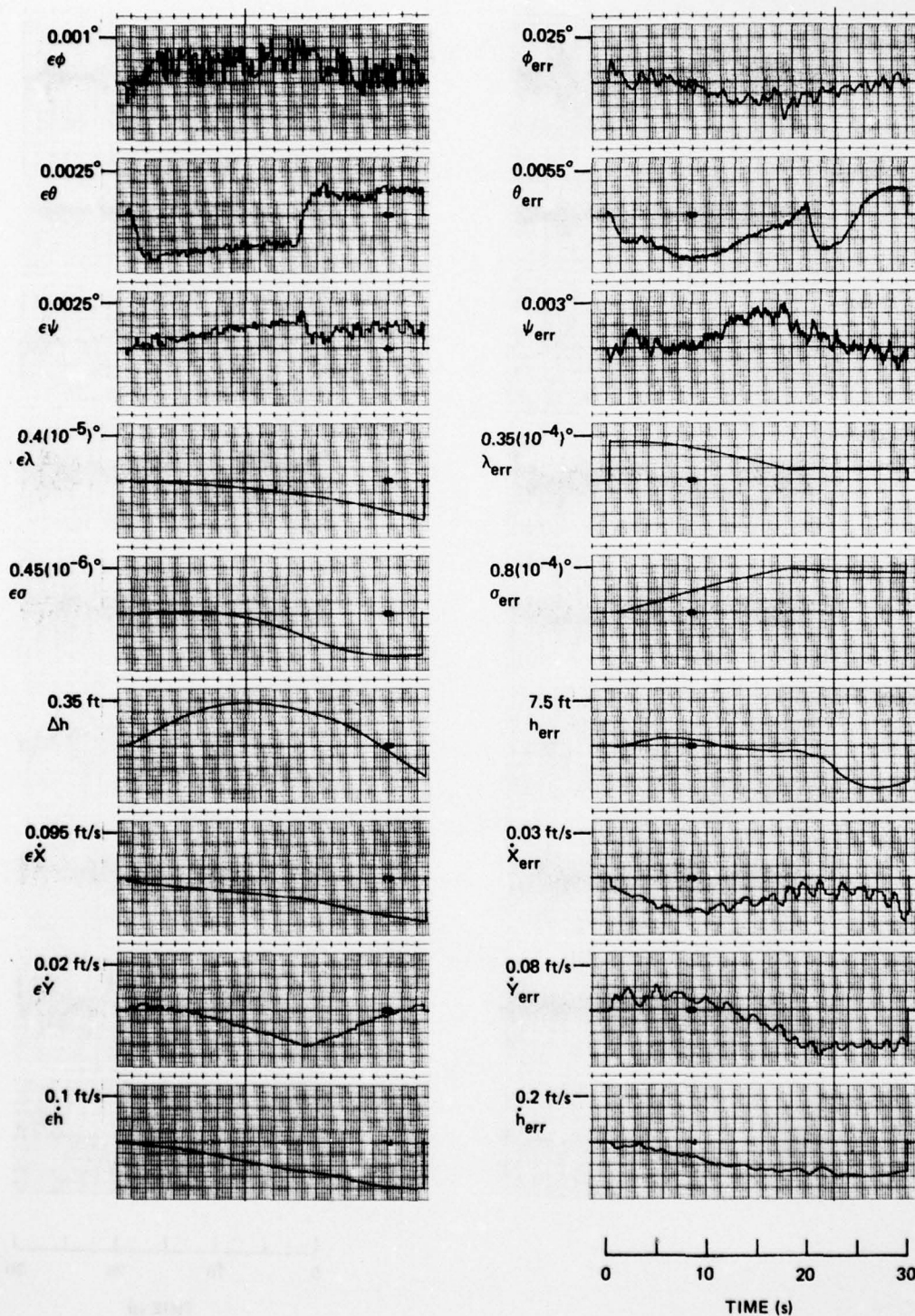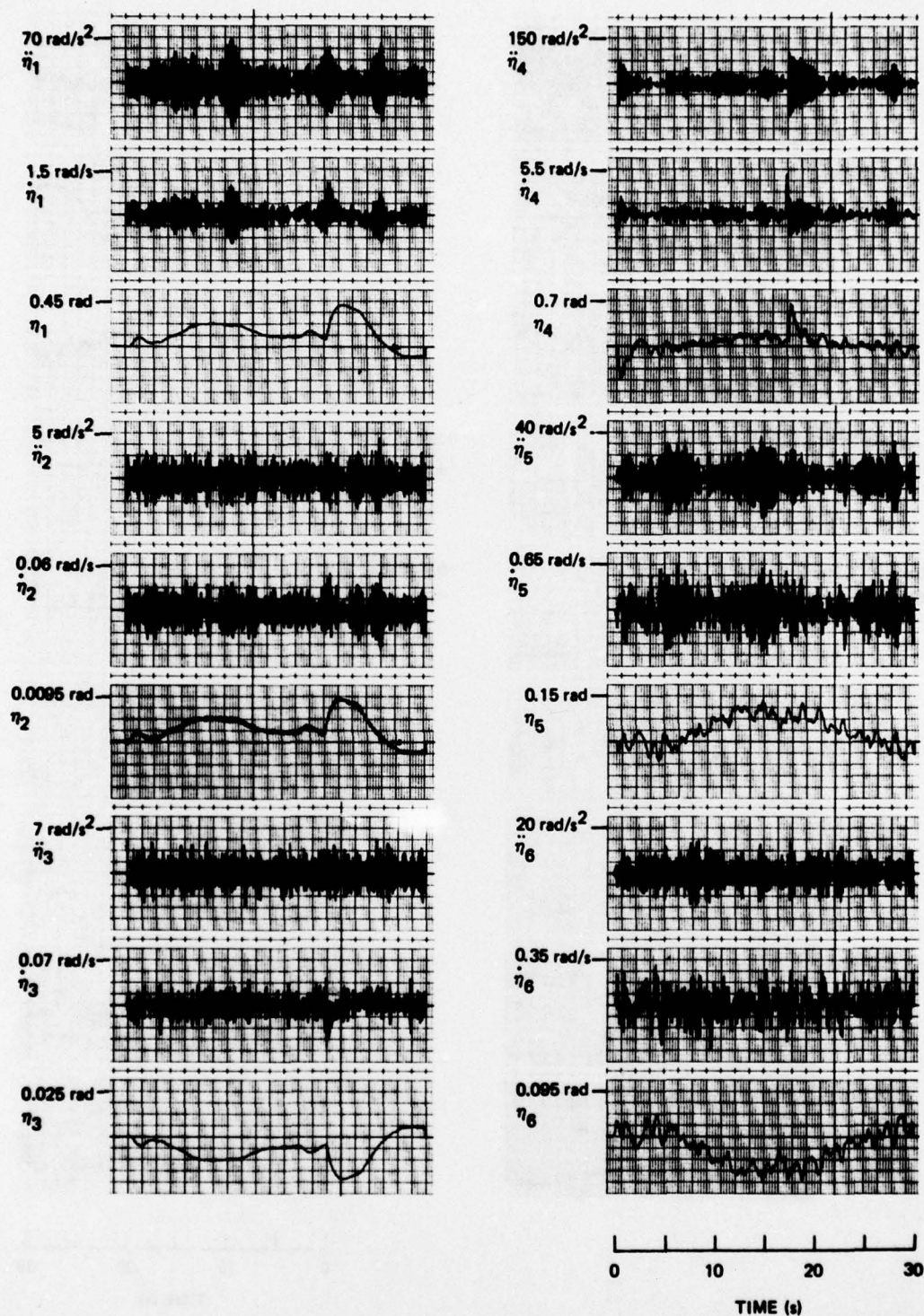
Figure 3-20. MIRA simulation responses: all sensors located at FS313; laser navigation gyros—navigation sensors used for flight control; 30-second run in turbulent environment (sheet 4 of 4).

orthogonal-triad configuration of a laser-gyro model located at FS313, correspond to those presented in Figure 3-14. The differences among the two sets of responses are not very dramatic, and the basic vehicle responses do not differ significantly, if at all. Some differences are evident in the flight-control signals, with those of Figure 3-20 showing the effect of the sensor quantization. The structural-mode responses are essentially the same in both cases, with those obtained for the dual-purpose navigation sensors being perhaps a slight bit larger in magnitude. The maximum value of the accelerations is slightly higher, resulting from the use of the navigation sensors for flight control, but the effect is certainly nothing that is going to be discernible to the pilot. Similar conclusions can be drawn for the orthogonal-triad configuration with the two-degree-of-freedom-gyro model. However, the responses for this case are not shown, since they add nothing to the information already presented. Therefore, there does not appear to be any strong technical reason why the navigation sensors cannot be used for flight-control purposes.

SECTION 4

TEST AND DEVELOPMENT PLAN

This section presents and discusses the topics that should be included in a test and development plan for MIRA-type sensor systems. Several of the items included in the plan are normally a part of test plans for conventional sensor systems, thus forming a base upon which to build the test plan. However, the uniqueness of the MIRA concept dictates that a much more comprehensive and detailed test plan be developed and carried out. It is this aspect of the proposed test plan that will receive the major consideration. A combination of analyses, laboratory and van testing, and use of the MIRA simulation is proposed to characterize the parameters of a MIRA system and ensure its proper operation.

The initial requirement for the test plan is a basic characterization of the instruments included in the MIRA system. This aspect is no different from that which would be done in the testing of any conventional sensor system, and includes laboratory tests to determine the basic parameters of the sensors (e.g., scale factors, rate limits, etc.). The next item that should be covered in the test plan is a determination of the nominal navigation and flight-control performance achievable with the sensor system. This would involve a series of laboratory and van tests to ascertain how well the sensor system meets the system specification and requirements of the dynamic environment in which the vehicle will be flying. The MIRA simulation can be useful in this area because the basic sensor characteristics established for this testing can be incorporated into it, and the navigation and flight-control performance achieved in the test can be verified with the simulation.

The next requirement that must be determined during the testing of the MIRA system is a definition of the relative differences existing among the system sensors. This information is needed to establish the

basic failure detection and isolation (FDI) capability of the MIRA
system. The parameters that would have to be determined during this
phase of the testing include misalignment effects and those effects
associated with a dynamic environment (e.g., the magnitude of the
g-dependent effects). The dynamic response of the individual sensors
will also be different due to different bandwidths, nonlinearities,
and the like. The noise level associated with the instrument, which
may be small in a dynamic environment, must also be determined to
characterize the quiescent level of the instrument's operation. An
extensive combination of laboratory and van testing in conjunction
with analyses will be needed to determine the required parameters and
the degree of confidence required for reliable operation of the MIRA
system.

The next logical step in the test plan will be a determination of
the failure modes of the sensor system. A combination of analysis
and appropriate testing to confirm the analysis will be required.
Once the failures have been catalogued, an investigation of the effect
of the failure modes on the performance of the MIRA and vehicle systems
should be undertaken. This phase of the testing should concentrate
upon two aspects of the problem. One deals with hard failures and
their effect upon the flight-control system and transient behavior
of the aircraft to ensure that the safety of the vehicle is not
compromised; the effect of the failures on the handling qualities of
the vehicle is an area of prime consideration. The other aspect of the
problem concerns the long-term navigation performance of the system
with instrument failures. The intent of the tests performed at this
time should be to gather statistical data for identifying the effects
of soft failures leading to a set of FDI requirements. Once again,
a combination of van testing and verification by simulation should be
required during this phase of the program.

The next tests required are those designed to specify the
parameters and verify the operation of the FDI mechanism of the sensor
system. With the knowledge obtained in the previous tests, it should
be possible to induce failures in the sensor system and verify that
the failure is detected and isolated, and the proper reconfiguration
is undertaken. Laboatory and van testing will again be required. A
tool such as the MIRA simulation could also be used to confirm the
results of the testing and provide more exhaustive and comprehensive
verification of the FDI algorithm.

The last item that should be considered in the test plan is the effect of the sensor reconfiguration on the performance of the vehicle. A particular example would be the transient induced into the control system due to the reconfiguration of the sensors. A combination of analyses and use of the MIRA simulation should provide answers to many of the questions that arise in this regard.

SECTION 5

SUMMARY AND CONCLUSIONS

The MIRAT technical effort at CSDL has been dedicated to the accomplishment of three major goals:

(1) The continuation of the simulation development effort begun under the first CSDL MIRA program.

(2) The utilization of the simulation tools in the test and evaluation phase of the MIRA program.

(3) The consideration of a test and development plan for MIRA-type systems.

The desired goals have been achieved in each of these three areas.

The simulation development phase of CSDL's effort concentrated on the conversion of the nonreal-time simulation (developed during the first phase of the CSDL MIRA effort) to digital real-time operation. This effort was given first priority in the program plan, and the result is a simulation capability that can be used to evaluate a wide class of MIRA systems in many different environments. The simulation is coded in fixed-point assembly language, and has been designed to operate on an XDS 9300 general-purpose digital computer, and two Honeywell 124 series computers, which operate as parallel processors.

The capability of the MIRA simulation has also been increased significantly during the course of this program by the addition of several subroutines. A navigation and attitude error-propagation algorithm using the incremental-velocity and angular-sensor errors as inputs together with flight-profile data has been incorporated into the MIRA simulation. It is now possible to isolate the effects of sensor errors on navigation performance with this capability. Models of two-degree-of-freedom gyros were also incorporated into the MIRA simulation to augment the laser-gyro models previously included. A

91

model of a transport vehicle was developed to permit the investigation of the operation of sensor systems in vehicles of this type. Last of all, an air-data sensor model was added to support the proposed MIRA configurations.

The simulation runs performed during this program were designed with two goals in mind. Parametric studies were performed to provide an indication of the effects of sensor type, sensor location, sensor errors, etc. In addition, specific potential MIRA configurations were evaluated to provide an assessment of their capability. This phase of the effort was hampered by the fact that CSDL did not receive the MIRA configurations selected by McDonnell Douglas for evaluation as called for in the contract Statement of Work. In lieu of this, CSDL selected and evaluated sensor configurations that were suitable for MIRA applications.

Two major sets of computer runs were performed. Eight 1-hour runs were made to determine the navigation performance of the various configurations selected, and ten 30-second runs were made to determine the effect of the configurations on the transient behavior of the aircraft systems.

The specific configurations evaluated were an orthogonal triad with laser gyros located near the cg of the vehicle and then forward of the pilot's station; the same configuration with two-degree-of-freedom-gyro models; and dodecahedron and octahedron configurations. Other variables in the simulation were the environment and the use of the navigation sensors for flight-control purposes.

Many conclusions were drawn from the simulation runs (see Section 3). The results concern the effects of the parametric investigation and the relative merits of the configurations evaluated. However, it is felt that the simulation runs performed and potential MIRA configurations evaluated were not extensive enough to justify the selection and recommendation of the most suitable specific-sensor configuration for the MIRA application.

Many suggestions were made for items that should be included in a test and development plan for MIRA systems. The basic plan calls for a combination of analyses, laboratory and van testing, and simulation verification to ensure the proper operation of a MIRA-type system. This plan includes the characterization of sensor instruments and the

determination of system performance and failure modes, operations associated with the testing of sensor systems in general. However, because MIRA systems require a much more extensive plan, suggestions were made to include differential instrument measurements, the effect of the failure modes on flight-control and navigation performance, the verification of the FDI and reconfiguration performance of the system, and a determination of the effects of the transients introduced into the vehicle system due to the sensor reconfiguration.

1. Daly, K., et al., Development of Capability for Multifunction Integrated Reference Assembly Evaluation, AFAL-TR-77-64, July 1977.

2. Sciegienny, J., et al., Inertial Navigation System Standardized Software Development, Final Technical Report, Charles Stark Draper Laboratory Report R-977, Volume II, June 1976.

3. Nurse, R., "Navigation and Attitude Error Propagation for a Strapdown Inertial Navigator—Given Inertial Sensor Error Time Histories and Flight Profile", Charles Stark Draper Laboratory Memorandum T&A 269-76, December 1976.

4. Computer Program Development Specification for Software for Avionics, System Simulation and Dynamic Validation, General Dynamics Report FZM-6197, May 1975.

5. Hooker, D., et al., Survivable Flight Control System Interim Report No. 1, Studies, Analyses and Approach, AFFDL-TR-71-20, May 1971.

6. Kisslinger, R., and G. Vetch, Survivable Flight Control System Interim Report No. 1, Studies, Analyses and Approach, Supplement for Control Law Development Studies, AFFDL-TR-71-20, Supplement 2, May 1971.

7. Motyka, P., "Real Time Transport Model Aerodynamics and Flight Control System", Charles Stark Draper Laboratory Memorandum (to be published).

8. Military Specification, Flying Qualities of Piloted Airplanes, MIL-F-8785B(ASG), August 1969.

9. Crisp, R., J. Gilmore, and A. Hopkins, Jr., SIRU—A New Inertial System Concept for Inflight Reliability and Maintainability, Charles Stark Draper Laboratory Report E-2407, May 1969.

10. Redundant IMU Instrument Orientation Requirements for IUS—Final Report, Charles Stark Draper Laboratory Report R-1076, March 1977.